

Single NdPc<sub>2</sub> Molecules on Surfaces:  
Adsorption, Interaction, and Molecular Magnetism

Inaugural-Dissertation

zur

Erlangung des Doktorgrades

der Mathematisch-Naturwissenschaftlichen Fakultät

der Universität zu Köln

vorgelegt von

Sarah Fahrendorf

aus Marl

Berichterstatter:  
(Gutachter)

PD Dr. D. E.Bürgler

Prof. Dr. T.Michely

Tag der mündlichen Prüfung: 24.01.2013

---

## Kurzzusammenfassung

---

Molekulare Nanomagnete, auch Einzelmolekülmagnete genannt, nehmen eine Schlüsselrolle in dem aufstrebenden Forschungsgebiet der molekularen Spintronik ein. Sie bilden die Grundbausteine für eine Weiterentwicklung spin-elektronischer Elemente der klassischen Spintronik zur molekularen Spintronik und könnten in molekularen Spinventilen, molekularen Spintransistoren oder als Quantenbits in Quantencomputern zur Anwendung kommen. Molekulare Nanomagnete sind gekennzeichnet durch hohe Grundzustände der Spinquantenzahl und eine Aufspaltung der Zustände im Nullfeld. Die dadurch entstehenden hohen Relaxationsbarrieren führen zu einer langen Relaxationszeit der Magnetisierung. Moleküle aus der Klasse der Doppeldecker Phthalocyanine mit einem einzigen Zentralion aus der Untergruppe der Lanthanoide ( $\text{LnPc}_2$ ) eingebettet zwischen zwei organische Phthalocyanin (Pc) Liganden sind von hoher Relevanz für das grundlegende Verständnis molekularer Nanomagnete. Der Einfluss von Substraten oder Elektroden auf adsorbierte Moleküle spielt eine zentrale Rolle bei der Entwicklung von Bauteilen für die molekulare Spintronik, da sich die elektronischen und magnetischen Eigenschaften der Moleküle verändern können. Ein umfassendes Verständnis des Substrateinflusses ist daher unerlässlich für eine Weiterentwicklung des Forschungsgebietes.

In dieser Doktorarbeit werden aus diesem Grund die elektronischen und magnetischen Eigenschaften des adsorbierten Neodym Doppeldecker Phthalocyanins ( $\text{NdPc}_2$ ) mittels Tieftemperatur-Rastertunnelmikroskopie und -spektroskopie (RTM und RTS) untersucht.

Hierfür werden zunächst die  $\text{NdPc}_2$  Moleküle unter Ultrahochvakuum-Bedingungen auf verschiedene Oberflächen aufgedampft. Es ergibt sich, dass sich ein hoher Anteil an Doppeldecker Molekülen bei der Deposition in einzelne Phthalocyanine zerlegt. Die Rate der zerstörten Doppeldecker ist dabei stark von der Art des Substrats abhängig. Aus diesem Grund wird die Schlussfolgerung gezogen, dass die elektronische Beschaffenheit der Oberfläche einen stabilisierenden oder destabilisierenden Einfluss auf die intra-molekularen Bindungen hat. Es stellt sich heraus, dass Ladungstransfer von der Oberfläche in die Orbitale des Moleküls ein möglicher stabilisierender Effekt sein könnte.

Eine detaillierte Studie der elektronischen und magnetischen Eigenschaften des adsorbierten  $\text{NdPc}_2$  Moleküls wird auf dem Substrat Cu(100) vorgenommen. Im Rahmen der Interpretation werden die Ergebnisse der experimentellen RTM- und RTS-Untersuchungen mit Dichtefunktionaltheorie (DFT) Rechnungen verglichen. Diese DFT-Rechnungen wurden von Mitarbeitern des Peter Grünberg Instituts (PGI-1) am Forschungszentrum Jülich ausgeführt. Es zeigt sich, dass der untere Pc-Ligand des  $\text{NdPc}_2$  Moleküls robuste chemische

---

Bindung mit Cu(100) eingeht und seine elektronischen Zustände mit denen der Oberfläche stark hybridisieren. Zugleich ist der Einfluss des Substrats auf die Zustände des oberen Pc-Liganden verschwindend und sie behalten ihren molekulartigen Charakter. Diese molekulartigen elektronischen Zustände können durch ein äußeres elektrisches Feld auf der Energieskala verschoben werden. Das zentrale Ergebnis dieser Studie ist jedoch der direkte Zugriff auf die spin-polarisierten  $4f$ -Zustände des zentralen Nd Ions mithilfe der Rastertunnelmikroskopie. Der direkte Zugang zu diesen Zuständen ist eine besondere Eigenschaft des NdPc<sub>2</sub> Moleküls im Vergleich zu analogen Spezies mit Lanthanoiden höherer Ordnungszahl als Zentralion und erlaubt rein elektrische Schreib- und Lesevorgänge des Spinzustands des Moleküls.

In Hinblick auf Untersuchungen der magnetischen Eigenschaften des NdPc<sub>2</sub> Moleküls werden spin-polarisierte RTM-Messungen an der zweiten Atomlage von Fe auf W(110) durchgeführt. Die eingesetzten Cr Spitzen werden ex-situ, anhand eines elektrochemischen Verfahrens von Cr Stäben heruntergeätzt. Weitere in-situ Präparationsschritte zeigen zudem keinen grundlegenden Einfluss auf die magnetischen Eigenschaften der Spitze. Die Etablierung der reproduzierbaren Präparation der ferromagnetischen Fe Oberfläche und der RTM-Spitzen bildet die Voraussetzung für die weiteren Messungen an adsorbierten NdPc<sub>2</sub> Molekülen mittels spin-polarisierter RTM. Vorläufige Ergebnisse von RTM-Untersuchungen geben Hinweise darauf, dass ein direkter Zugang zu den spin-polarisierten  $4f$ -Zuständen auch nach Adsorption des Doppeldecker Moleküls auf der zweiten Atomlage von Fe auf W(110) möglich ist.



---

## Abstract

---

Single molecule magnets (SMMs) play an important role in the field of molecular spintronics. They have huge potential for application in molecular-spin-transistors, molecular-spin-valves, and molecular quantum computing. SMMs are characterized by high spin ground states with zero-field splitting leading to high relaxation barriers and long relaxation times. A relevant class of molecules are the lanthanide double-decker phthalocyanines ( $\text{LaPc}_2$ ) with only one metal atom sandwiched between two organic phthalocyanine (Pc) ligands. For envisaged spintronic applications it is important to understand the interaction between the molecules and the substrate and its influence on the electronic and magnetic properties.

The subject of this thesis is the investigation of the adsorbed neodymium double-decker phthalocyanine ( $\text{NdPc}_2$ ) by means of low temperature scanning tunneling microscopy and spectroscopy (STM and STS).

The molecules are deposited by sublimation onto different substrates. It is observed that a large fraction of the double-decker molecules decomposes during deposition. The decomposition probability strongly depends on the chosen substrate. Therefore it is concluded that the substrate modifies the electronic structure of the molecule leading to a stabilization or destabilization of the molecular entity. Charge transfer from the surface to the molecule is identified as a potential stabilizing mechanism.

The electronic and magnetic properties are investigated in detail for adsorbed  $\text{NdPc}_2$  molecules on  $\text{Cu}(100)$ . The results of the experimental study are compared to state-of-the-art density functional theory calculations performed by our colleagues from the Peter Grünberg Institute (PGI-1) at the Forschungszentrum Jülich. Interestingly, the lower Pc ring of the molecule hybridizes intensely with the substrate leading to strong chemisorption of the molecule, while the upper Pc ring keeps its molecular type electronic states, which can be energetically shifted by an external electric field. Importantly, it is possible to get direct access to the spin-polarized  $4f$ -states of the central Nd ion by means of STM and STS. This important and unique characteristic absent for late lanthanide double-decker phthalocyanine molecules opens the door for direct reading and writing of the molecular spin-state by purely electrical means.

In view of the intended investigations of the magnetic properties of the  $\text{NdPc}_2$  molecule coupled to ferromagnetic surfaces, spin-polarized STM investigations of the second atomic layer of Fe on  $\text{W}(110)$  are performed. Here, bulk Cr-tips are used, which were ex-situ electrochemically etched from a Cr rod. Further in-situ treatment is shown to have no essential influence on the magnetic properties of the tips. The reproducible and

---

reliable preparation of the ferromagnetic substrate and the Cr-tips is the basis for further investigations of the NdPc<sub>2</sub> molecule adsorbed on the second atomic layer of Fe on W(110). Preliminary STM and STS results give strong evidence, that the direct access to the spin-polarized 4*f*-states is also feasible after adsorption of the double-decker molecule on a ferromagnetic substrate.

# Contents

<b>I</b>	<b>Introduction</b>	<b>1</b>
<b>II</b>	<b>Molecules in Spintronics</b>	<b>5</b>
II.1	Molecules with Magnetic Properties . . . . .	5
II.1.1	Single Molecule Magnets . . . . .	6
II.2	Adsorption on Surfaces . . . . .	7
II.3	Magnetic Molecules on Surfaces . . . . .	9
II.4	NdPc <sub>2</sub> Double-Decker Molecule . . . . .	9
<b>III</b>	<b>Scanning Tunneling Microscopy</b>	<b>13</b>
III.1	The One Dimensional Tunneling Effect . . . . .	14
III.2	Interpreting STM Images . . . . .	16
III.3	Probing the Local Density of States . . . . .	18
III.4	Spin-Polarized Tunneling Experiments . . . . .	20
<b>IV</b>	<b>Experimental Methods</b>	<b>25</b>
IV.1	Vacuum System . . . . .	25
IV.2	Tip Preparation . . . . .	27
IV.2.1	Tungsten Tips . . . . .	27
IV.2.2	Chromium Tips . . . . .	28
IV.3	Sample Preparation . . . . .	33
IV.3.1	Sputtered Samples . . . . .	33
IV.3.2	HOPG . . . . .	34
IV.3.3	Iron on Tungsten . . . . .	34
IV.4	Molecules . . . . .	36
<b>V</b>	<b>Adsorption of NdPc<sub>2</sub> on Surfaces</b>	<b>39</b>
V.1	Surface-Dependent Adsorption . . . . .	40
V.1.1	Cu(100) . . . . .	41
V.1.2	Fe on W(110) . . . . .	43
V.1.3	Au(111) . . . . .	44
V.1.4	Au(100) . . . . .	46
V.1.5	HOPG . . . . .	47
V.2	Discussion . . . . .	47

<b>VI NdPc<sub>2</sub> Spin-Polarized 4<i>f</i>-States Accessed by STM</b>	<b>51</b>
VI.1 Adsorption of NdPc <sub>2</sub> on Cu(100) . . . . .	51
VI.2 Electronic Structure of the Adsorbed NdPc <sub>2</sub> . . . . .	55
VI.3 Conclusion and Perspectives . . . . .	61
<b>VII Iron on Tungsten</b>	<b>63</b>
VII.1 Previous Results . . . . .	64
VII.1.1 Topography . . . . .	64
VII.1.2 Electronic and Magnetic Properties . . . . .	65
VII.2 SP-STM Investigations on the 2nd Monolayer of Fe on W . . . . .	68
VII.2.1 Mapping the Surface . . . . .	68
VII.2.2 Out-of-plane Domains . . . . .	69
VII.2.3 Domain Wall Investigations . . . . .	72
<b>VIII NdPc<sub>2</sub> Adsorbed on Fe on W(110)</b>	<b>77</b>
VIII.1 Topographic and Electronic Structure . . . . .	78
<b>IX Summary and Outlook</b>	<b>85</b>
<b>Bibliography</b>	<b>89</b>
<b>Acknowledgement</b>	<b>99</b>
<b>Curriculum Vitae</b>	<b>103</b>

---

## Introduction

---

The continuous demand for increasing information processing capacity and data storage density leads to an ongoing miniaturization of electronic devices that will in the near future hit physical limitations at the current technologies. In view of this upcoming challenge new materials for advanced technologies with high densities and low energy consumption have to be developed. One promising pathway is focussing on the ultimate molecular limit by integrating molecules into electronic devices [1]. The conventional top-down fabrication process of electronic devices reaches its limits at a scale of the wavelength of the light used in the photolithography procedure. In contrast to this, molecules consisting of only tens of atoms can be implemented in devices using bottom-up processes, which does not rely on any lithography.

In the research field of molecular electronics [2], transport through molecular orbitals is studied by connecting molecules to nanoelectrodes. In these measurements, quantum effects as for instance the coulomb-blockade can be observed [3]. Molecules offer some general properties that make them well suited for the integration into electronic devices. The synthesis of organic molecules with sizes down to a few Å in large quantities and with perfect reproducibility is possible at low cost. By means of chemical synthesis certain functionalities such as the coupling to electrodes, the magnetism or the transport properties can be easily tailored [4, 5]. Furthermore, they show the ability of self organization on appropriate substrates which makes the realization of molecule chains or arrays on surfaces feasible [6].

Combining the field of molecular electronics with the field of spintronics by integrating molecules with magnetic properties into the devices offers the spin of an electron as an additional degree of freedom [7, 8]. Setting, manipulating, and detecting of spins allows using the electron spin rather than the electron charge as a state variable for information processing. Depending on the spin-state of the electron it for instance interacts differently with magnetic material [9–11]. Entities with stable magnetic moment furthermore maintain their spin-state between manipulation steps, i.e. they show non-volatility. Spin-states can be controlled by applying external magnetic fields, spin-polarized currents or even

light [12]. The switching processes in general cost less energy the lower the number of manipulated spins is. In magnetic molecules the number of spins is orders of magnitudes smaller than in lithographically defined nanomagnets.

In the combined research field called molecular spintronics one or more molecules with magnetic properties are integrated into molecular devices with spintronic functionalities such as e.g. molecular spin-valves [7]. A relevant class of molecules for molecular spintronics are the single molecule magnets (SMMs). SMMs act like permanent magnets on the molecular level, which means that they show zero field splitting with an anisotropy direction leading to a slow relaxation of the magnetization [13]. This makes them in addition perfectly suited as qubits for quantum computing [14]. They combine some characteristics of ferromagnetic bulk materials with advantages of the molecular scale: molecules are perfectly monodispers, whereas nanoparticles for instance vary in shape, size, and magnetic anisotropy. Moreover they typically consist of organic ligands surrounding one or more metal centers with unpaired electrons, which make up the total magnetic moment [13]. This means that only a few electron spins have to be manipulated in order to switch the magnetization of the molecule. Low energy consumption for the switching and manipulating processes is therefore expected.

For the implementation of molecules into electronic devices they have to be deposited on substrates and connected to electrodes. Due to the small molecular structure consisting of only a few tens of atoms in total the influence of an extended substrate on the electronic structure of the molecule becomes significant. This might also change the magnetic properties. Therefore a fundamental understanding of the influence of the substrates on adsorbed molecules is crucial for the further development of molecular spintronics. This requires a combination of experimental results with theoretical calculations. However, the comparison of experiment and theory is only possible if the investigated system is well defined. Scanning tunneling microscopy (STM) and spectroscopy (STS) in ultra high vacuum are versatile tools regarding this requirement: isolated molecules adsorbed on atomically clean and well defined crystalline surfaces are investigated with an atomically sharp tip that allows gaining insight into the electronic properties with high spatial resolution.

In this thesis the adsorption characteristics of molecules with magnetic properties deposited on various surfaces are addressed. In particular the mononuclear early lanthanide double-decker phthalocyanine complex  $\text{NdPc}_2$  is investigated via STM and STS. It is a promising candidate for being an SMM, since some of its late lanthanide analogues like the  $\text{TbPc}_2$  complex are already known to show SMM properties [4].

The  $\text{NdPc}_2$  molecules are synthesized by Dr. Claire Besson of the chemistry group of Prof. Dr. Paul Kögerler of the Forschungszentrum Jülich and RWTH Aachen. For a detailed study, the experimental STM and STS results are compared to state-of-the-art density functional theory calculations carried out by Dr. Nicolae Atodiresei and Dr. Vasile Caciuc from the Peter Grünberg Institute of the Forschungszentrum Jülich. The magnetic properties of the adsorbed molecule are addressed by spin-resolved calculations as well as

---

preliminary spin-polarized STM and STS measurements.

In the beginning of this thesis the theoretical background for the STM study of single molecules with magnetic properties is given. Chapter II introduces the concept of molecular magnetism and possible molecule-surface interactions. The explanations concentrate on aspects, which are crucial for the interpretation of the experimental and theoretical results. Afterwards the theory of STM and STS as well as spin-polarized STM (SP-STM) is presented in Chapter III.

Chapter IV gives experimental details including the vacuum system, sample preparation and STM-tip preparation. The focus in this Chapter lies on the reproducible ex-situ and subsequent in-situ preparation procedure of bulk Cr-tips for SP-STM measurements.

The experimental results are presented in the next four Chapters. As a starting point the substrate dependence of the adsorption of the NdPc<sub>2</sub> molecule is discussed for various surfaces in Chapter V. A detailed analysis of the electronic and magnetic structure of the adsorbed NdPc<sub>2</sub> molecule is then given for the case of a Cu(100) substrate. The results of this combined experimental and theoretical study are presented in Chapter VI. In view of SP-STM and STS investigations of the adsorbed NdPc<sub>2</sub> complex the ferromagnetic surface Fe on W(110) is subject of Chapter VII in order to introduce this surface as a ferromagnetic substrate and to demonstrate our ability to perform spin-polarized STM and STS experiments. The measurements concentrate on the out-of-plane domains and in-plane domain walls of the second atomic layer of Fe on W(110). This surface layer serves as a ferromagnetic substrate for the preliminary SP-STM study of the adsorbed NdPc<sub>2</sub> presented in Chapter VIII.

In Chapter IX the experimental and theoretical results are summarized and evaluated. Finally an outlook on potential subsequent experiments is given.





---

### Molecules in Spintronics

---

Implementing molecules with intrinsic magnetic moment into conventional spintronic devices has attracted a great deal of interest [7]. It has just recently been shown that molecules with magnetic moments, namely  $\text{TbPc}_2$ , attached to a carbon nanotube can function as a spin-valve device at the molecular level [15]. One of the main topics in investigating single molecules for spintronic applications is the interaction between these molecules and the surroundings for instance the substrate. Adsorption on metallic surfaces has a large influence on the electronic and therefore also the magnetic properties of the adsorbed molecule. In the following Sections the characteristics of molecules with magnetic properties are introduced. In addition an introduction about chemical bonding is given to provide the basis for the interpretation of the results. Furthermore a short overview about possible interactions of magnetic molecules with surfaces is given, and finally in the last Section, the  $\text{NdPc}_2$  double-decker phthalocyanine molecule investigated in this work is described to provide the information necessary for the analysis of the experimental and calculated data.

#### II.1. Molecules with Magnetic Properties

It is possible to classify molecules, depending on their response to external magnetic fields. Diamagnetic molecules will be repelled by external magnetic fields, due to the induced magnetic moment that causes a magnetic field opposite to the external one. In contrast to this, paramagnetic molecules will be attracted and their intrinsic magnetic moment aligns with the direction of the applied external field. In contrast to the diamagnetic molecule, the paramagnetic molecule comprises orbitals with un-paired spins, causing the intrinsic magnetic moment. For spintronic application one relevant class of molecules are the so called single molecule magnets (SMM) functioning as magnets on the molecular scale [7, 13].

### II.1.1. Single Molecule Magnets

SMMs show a combination of characteristics of classical magnets with properties of quantum systems, such as transport through well defined molecular orbitals and quantum tunneling of the magnetization. SMMs are paramagnetic molecules with the addition of a zero field splitting and a slow relaxation of the magnetization. That means that similar to a conventional ferromagnetic material with long range order, they show an anisotropy direction of the magnetic moment and a certain relaxation time. Depending on the temperature and time-scale, on which the molecules are studied, they can be referred to as SMM and superparamagnetic-like molecule. Their magnetic properties can be described by the Hamiltonian

$$H = DS_z^2 + E(S_x^2 + S_y^2) + g\mu_B\mu_0\mathbf{S} \cdot \mathbf{H} \quad (\text{II.1})$$

with  $D$  and  $E$  being the anisotropy constants,  $g\mu_B\mu_0\mathbf{S} \cdot \mathbf{H}$  describing the Zeeman energy generated by the applied magnetic field  $\mathbf{H}$  and  $S_i$  representing the spin components of the system. Figure II.1 (a) illustrates the energy landscape of an SMM. Here the anisotropy constant  $D$  is negative and we assume the easy axis to be in  $z$ -direction. The potential barrier height is then given by  $DS_z^2$  and consists of  $(2S + 1)$  energy levels indicated in the figure by the red lines. A magnetization reversal occurs for example by thermal excitations over all  $(2S + 1)$  energy levels as shown in Fig. II.1 (a) by the green arrows climbing up and down over the potential barrier or via quantum tunneling of the magnetization [13]. The energy levels of the two wells are shifted with respect to each other when an external field is applied. At certain resonance fields where two levels align at the same energy, the electron spin can flip its direction by direct tunneling into energy levels on the other side of the double-well potential as indicated by the blue arrow in Fig. II.1 (a). The quantum tunneling can be directly observed in Fig. II.1 (b), in which hysteresis loops for various temperatures between 4 and 0.1 K are shown. Characteristic steps, indicating a change in the magnetic state of the molecule due to resonant tunneling, are observed at resonant field values. With decreasing temperature the hysteresis loops become broader due to the reduced thermally activated magnetization reversal. For temperatures below 0.6 K the hysteresis loops become temperature independent and do not change their shape and saturation field anymore. Here, the magnetization reversal is by quantum tunneling of the magnetization only.

Chemically, SMMs consist of an inner magnetic center of one or more magnetic atoms and a surrounding organic ligand system. The magnetic atoms can for instance be transition metal atoms like Fe in the  $\{\text{Fe}_4\}$  compound [16] and Mn in the  $\{\text{Mn}_{12}\}$  SMM [17] as well as rare earth atoms like Tb in TbPc<sub>2</sub> molecules [4]. The organic ligands can be chemically functionalized to alter the coupling of the molecule to the environment and to enhance the magnetic properties, for example to increase the blocking temperature and relaxation times [18]. The coupling to the environment is one of the main challenges in controlling the magnetic properties of adsorbed SMMs. Therefore it is crucial to understand the fundamental properties of adsorbed magnetic molecules. The next two Sections give an

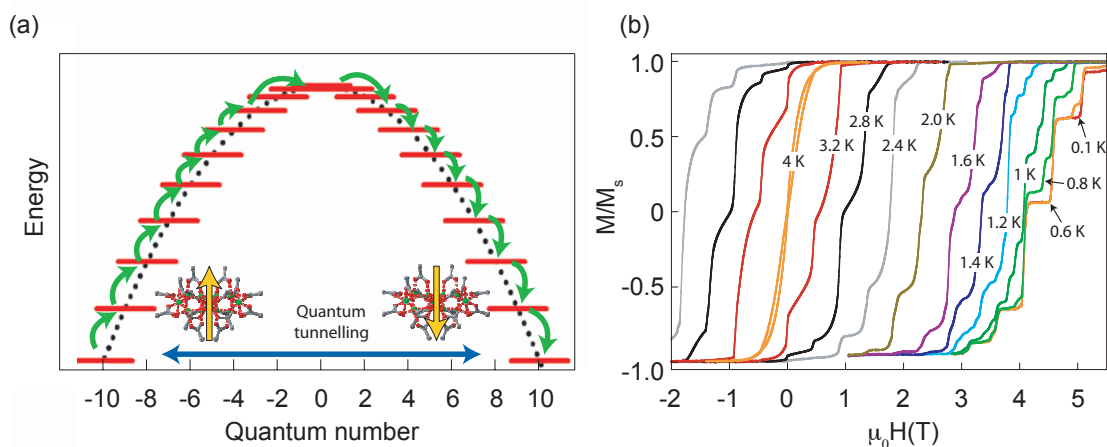


**Figure II.1.:** (a) Schematic representation of the potential barrier separating the two spin ground states of an SMM. Magnetization reversal can occur due to quantum tunneling of the magnetization or by thermal excitation, respectively. (b) Hysteresis loops for the  $\{\text{Mn}_{12}\}$  SMM complex at various temperatures between 4 and 0.1 K. The characteristic steps generated by quantum tunneling of the magnetization are observed at resonant fields. (taken from [7])

overview about adsorption mechanisms on surfaces in general and the influence of the adsorption on magnetic molecules in particular.

## II.2. Adsorption on Surfaces

In contrast to the bulk of a material, where the bonds are completely saturated by surrounding atoms, the bonding conditions of the surface atoms differ in the way that they attract additional molecules or atoms to be bound. This may lead to an adsorption of molecules or atoms on the surface of the adsorbent. Depending on the different species involved, the adsorption energy describing the energy gain of the system after adsorption and the bonding mechanisms themselves vary. One distinguishes in general between processes called physisorption, in which only physical forces are involved into the bonding (e.g. van-der-Waals bonding), or chemisorption due to actual chemical bond formation (e.g. covalent bonding). In a physisorption process the electronic structure of the adsorbate is only weakly influenced and bonding energies are low compared to the process of chemisorption, in which new bonds between the adsorbate and the adsorbent are created and the electronic structure of the adsorbate might be altered. The forces generating the physisorption are van-der-Waals forces, resulting from dipole interactions between adsorbate and adsorbent. The van-der-Waals forces are weak compared to the mechanisms involved in chemisorption and can only be directly observed in bonds of purely physisorbed character at low temperatures, since the energy is of the order of the thermal activation energy at room temperature  $k_B T = 26 \text{ meV}$ , but can play an important role in the bonding characteristics of molecules on surfaces [19]. In contrast to this, as already

mentioned, chemisorption results from bond formation between the atoms of the surface and of the adsorbate. The three main bonding types are ionic, covalent and metallic bonding. However, a strict classification, whether a bond is of either of ionic or covalent character, is challenging. The metallic bonding plays a negligible role in the adsorption of organic molecules on surfaces, since it is generated by sharing of delocalized conduction electrons between the involved atoms. A metal-organic molecule does not match the requirements for the formation of a metallic bond in the sense of delocalized electrons, as they are found in metallic system. An ionic bond is formed between atoms with a large difference in electronegativity. Electronegativity is a chemical measurement that describes the tendency of an atom to attract electrons. The prominent example for the formation of an ionic bond is table salt consisting of Na and Cl, in which Cl has the much higher tendency to attract an electron. The result is an almost pure ionic, strongly polar bond between the two species, where one electron of the Na is transferred to the Cl. The covalent bonding is generated by the sharing of valence electrons of the species involved in the bond formation leading, in the best case, to a full outer shell and a stable electronic configuration. Atoms with equal or similar electronegativity form bonds of almost pure covalent character. If the electronegativity difference becomes larger, the bond gets more polar, as e.g. in a water molecule, until it reaches almost entirely ionic character like in NaCl. In consequence, it is not possible to completely separate covalent and ionic bonding from each other. Another important characteristic of covalent bonding, is the formation of bonds in which electrons are shared by more than two atoms. The electrons are then referred to as delocalized electrons similar to the delocalized electrons in the conduction band of a metal. An important example for a molecule comprising delocalized electrons is the benzene  $C_6H_6$  molecule, in which the six electrons of the three carbon double bonds are shared by the whole carbon framework. These six electrons are called  $\pi$ -electrons, because they populate the  $\pi$ -orbitals of the molecule.  $\pi$ -orbitals are formed in the molecule by an overlap of two atomic p-orbitals. Due to the overlap a new orbital with a different geometry is formed. These new, so called hybrid orbitals are found in a variety of organic molecules comprising carbon double bonds, like the benzene molecule and are called  $\pi$ -conjugated molecules. Hybridization is in general an important property of covalent bonding and not exclusively found in conjugated molecules. It describes the mixing of overlapping atomic orbitals that form new hybrid orbitals accounting for certain geometries in the bond formation. How strong the hybridization is and which geometry the new hybrid orbitals will show depends strongly on the overlap of the involved atomic orbitals, their geometry and their energy.

For the adsorption of molecules on surfaces, the described bond formations play important roles. However, a clear definition of the bond character is not necessarily possible, because a mixture of the different bonding types is in general observed. Since the molecules are relatively large systems, only large-scale calculations, like full density functional calculations, will be able to predict the influences of the chemisorption on the electronic structure of the molecule.

### II.3. Magnetic Molecules on Surfaces

Whenever a molecule adsorbs on a surface, different kinds of bond formation occur as discussed in Section II.2, such as hybridization of the molecular orbitals with the orbitals of the metallic surface and charge transfer from the surface to the molecule. The charge transfer occurs due to a difference in the tendency to attract electrons, similar to what is happening in an ionic bond formation. As already mentioned, an additional interaction generated by dipole-dipole forces that is known to be important for the adsorption of  $\pi$ -conjugated molecules on surfaces, is the van-der-Waals interaction [19]. It will mainly influence the bond length between the molecule and the surface and in consequence also the overlap of the orbitals of molecule and surface and therefore the hybridization strength. Hybridization and charge transfer lead to a reorganization of the electronic structure of the molecule and therefore also possibly influence the magnetic properties. It has been shown, for example, that hybridization with and charge transfer from the metallic surface to the molecule occurs in paramagnetic transition metal single-decker phthalocyanines, such as FePc, CoPc, NiPc and CuPc on Ag(100). However, the consequences on the magnetic and electronic properties differ depending on the central metal. For FePc and CoPc, the magnetic moment of the metal center is reduced, whereas in the case of NiPc and CuPc, the spin of the central atom stays unperturbed and an additional spin is induced into the Pc ligand [20]. It has also been shown that in CoPc adsorbed on Fe, the spin of the central transition metal is fully quenched [21]. For the adsorbed SMM TbPc<sub>2</sub> an unpaired spin is transferred to the ligand system that alters the conductance on Au drastically [22] and influences the coupling to ferromagnetic surfaces [23]. In consequence, it is impossible to draw a general conclusion about the influence of the substrate on the magnetic properties of the molecule. The so called spinterface [24] that means the interaction of the two spin systems of the surface and the molecule is therefore known to be crucial and has been studied in many scientific articles for different classes of magnetic molecules, mainly paramagnetic, and different surfaces [21, 23, 25–27].

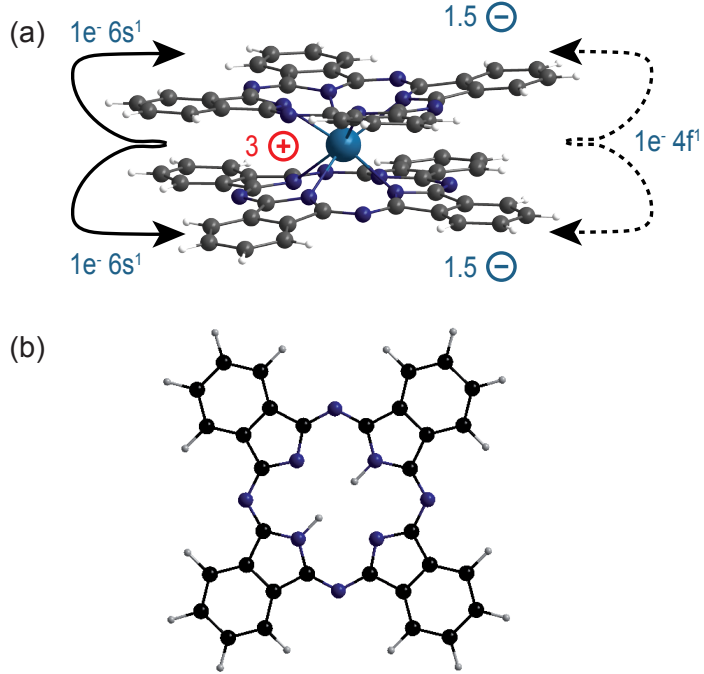
In conclusion, the same molecule that exhibited SMM behavior studied in bulk samples or as a free molecule in the gas phase can, for instance, be modified upon adsorption in a way that it still shows a magnetic moment but without magnetic anisotropy. Therefore studies of single SMMs on surfaces are of high importance to investigate whether a molecule is qualified to offer SMM characteristics also after the adsorption on metallic surfaces, since adsorption is the first step towards the construction of spintronic devices.

### II.4. NdPc<sub>2</sub> Double-Decker Molecule

A relevant class of molecules for potential spintronic applications are the mononuclear lanthanide double-decker phthalocyanines (LnPc<sub>2</sub>) with only one metal ion in the center of the organic ligands [4, 28]. Besides the particular characteristics of the individual LnPc<sub>2</sub> molecules, there are some general properties favoring the application of these double-decker molecules in spintronic devices. One main aspect in integrating molecules into devices is the adsorption on substrates. After adsorption, the characteristic properties of molecular

electronic features should still be preserved. The double-decker phthalocyanine molecules fulfill this requirement. Due to the double-decker structure and the weak electronic coupling of the two Pc rings through the central ion, the lower ring will be strongly chemisorbed on the surface whereas at the same time the upper Pc ring still exhibits electronic features of molecular character. In this work, we chose in particular the  $\text{NdPc}_2$  molecule for our investigations. A model of the  $\text{NdPc}_2$  molecule that consists of two phthalocyanine (Pc) rings with a neodymium ion in the center is shown in Fig. II.2 (a) to illustrate the double-decker structure of the molecule. The bare phthalocyanine molecule ( $\text{H}_2\text{Pc}$ ) with the molecular formula  $\text{C}_{32}\text{H}_{18}\text{N}_8$  is illustrated in Fig. II.2 (b). It consists of four isoindole rings linked by four nitrogen atoms forming a molecule with a four-fold symmetry. The two chemical bonds to the nitrogen atoms in the center are satisfied by hydrogen atoms.

**Figure II.2:** (a)  $\text{NdPc}_2$  double-decker phthalocyanine molecule. The bonding of the molecule is mainly of electrostatic character. The central Nd atom transfers three electrons to the two phthalocyanine rings. (b) phthalocyanine molecule with two hydrogen atoms in the center. The molecule consists of four isoindole rings linked by nitrogen atoms. Atomic representation: hydrogen (white), carbon (grey), nitrogen (dark blue) and neodymium (blue).



The electronic configuration of the neutral neodymium atom is  $[\text{Xe}]4f^46s^2$ . After bonding with the two hydrogen-free phthalocyanine rings three electrons are transferred from the central ion to the rings, namely the two  $6s^2$  and one  $4f$ -electron, indicated by the arrows in Fig. II.2 (a). Since each of the two rings would accept two electrons, one electron is shared by them. This results in a charge of  $3e^+$  on the central ion and a net charge of  $1.5e^-$  left on each of the rings. In consequence the bonding of the molecule is mainly of electrostatic nature and there is only a weak electronic coupling from one phthalocyanine via the central atom to the other ring. This hybridization [29] but also the repulsive negative charges on the two Pc rings lead to a relative rotation of  $45^\circ$  with respect to each other. As a consequence of the charge transfer the Nd atom will remain with three  $f$ -electrons in one spin-channel while the two Pc ligands will share the former Nd  $4f$ -electron in the opposite

spin-channel. It is known that in systems comprising atoms with high atomic number  $Z$  the spin-orbit coupling (SOC) strongly modifies the band structure. For this reason a calculation of the total magnetic moment of the molecule is only feasible by including SOC. However, charge density calculations of the free NdPc<sub>2</sub> molecule including SOC show that the energetic position of the states is barely influenced. This allows to neglect the SOC in the calculations for the adsorbed NdPc<sub>2</sub> molecule in this study and has been done for the reason to reduce the anyway long computing times. As a result an information about the total magnetic moment cannot be given here. Nevertheless, the total spin moment is known and results to  $2(\sqrt{s_{\text{Nd}}(s_{\text{Nd}} + 1)} - \sqrt{s_{\text{Pc}}(s_{\text{Pc}} + 1)}) \mu_{\text{B}}$  with  $s_{\text{Nd}} = 3/2$  on the Nd ion and  $s_{\text{Pc}} = 1/2$  on the two organic ligands, respectively.

Different lanthanide double-decker molecules have been studied under the aspect of single molecular magnetism [4, 28], but the NdPc<sub>2</sub> molecule was throughout neglected in these studies. The intramolecular bonding inside the NdPc<sub>2</sub> is weak compared to those molecules comprising late lanthanide atoms with higher atomic number [30]. This leads to very low yields in the synthesis of the molecules. These low yields are the main reason why NdPc<sub>2</sub> was not included in earlier studies and the interest focused on lanthanide atoms with higher occupied  $4f$ -orbitals. So far TbPc<sub>2</sub> and DyPc<sub>2</sub> are already known to be SSM with long relaxation times and hysteretic behavior, when measured in bulk and diamagnetic diluted bulk samples. The high blocking temperatures of several tens of Kelvin [28, 31] make them extremely interesting compared to transition metal complexes. The highest blocking temperatures reported for the latter are below 8 K [18]. As a consequence, the electronic properties of TbPc<sub>2</sub> and DyPc<sub>2</sub> adsorbed on different surfaces have been studied in the past by various of techniques. Vitali et al. [32] for example performed STM studies on the TbPc<sub>2</sub> molecule adsorbed on Cu(111) indicating that the SMM character might be preserved despite strong substrate molecule interaction. The same behavior was observed by Stepanow et al. [33] by means of XMCD measurements on TbPc<sub>2</sub> adsorbed on Cu(100), where the magnetic moment of the molecule is found to be of Ising type and aligns parallel or antiparallel to the surface normal. Kondo resonances were absent for TbPc<sub>2</sub>, DyPc<sub>2</sub> and YPc<sub>2</sub> when studied as single molecules adsorbed on Au(111) [34, 35], whereas a Kondo resonance could be observed and manipulated for TbPc<sub>2</sub> grown as islands on Au(111) [22]. More recently Schwöbel *et al.* reported about spin-polarized STM on TbPc<sub>2</sub> single molecules adsorbed on the ferromagnetic surface cobalt on iridium [36]. As already mentioned above it was also shown that TbPc<sub>2</sub> attached to carbon nanotubes can function as a molecular spin-valve device [15].

Besides the lack of experimental information regarding its molecular magnetism NdPc<sub>2</sub> is a promising candidate for electronics with single molecular magnets from the theoretical point of view. For spintronic applications it is important that the  $4f$ -states that give rise to the magnetic moment, lie energetically and spatially in a range accessible to transport experiments. Compared to the prominent TbPc<sub>2</sub> molecule, the  $4f$ -electrons in NdPc<sub>2</sub> lie closer to the Fermi energy and can more easily be tuned by the molecular framework and accessed in a transport experiment. A similar argument is valid for the spatial position of the orbitals. Figure II.3 shows an excerpt of the periodic table of the elements for selected atoms of the period of the lanthanides. The occupation of the  $4f$ -orbitals is lower in the Nd

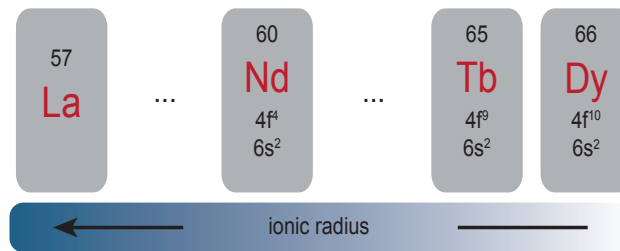


**Figure II.3.:** Excerpt of the periodic table of the elements for selected atoms of the lanthanide period.

atom compared to Tb and Dy, due to its lower atomic number  $Z$  leading to orbitals which are less localized around the nucleus. The increased spatial extend of the  $4f$ -electrons in the NdPc<sub>2</sub> molecules leads to lower binding energies and also geometrically favors the accessibility of the magnetic states in transport experiments.

By means of combined density functional theory and scanning tunneling microscopy investigations of the NdPc<sub>2</sub> molecule on Cu(100) it will be confirmed in Chapter VI that the direct access to the  $4f$ -states of the molecule is indeed possible.



## CHAPTER III

---

### Scanning Tunneling Microscopy

---

Scanning tunneling microscopy (STM) and spectroscopy (STS) are versatile tools to investigate topographic, electronic, and magnetic properties of conducting surfaces down to the atomic scale. The working principle is based on the quantum mechanical tunneling effect of electrons tunneling through a gap between surface and probing tip.

As shown in Fig. III.1 an atomically sharp tip is approached to a conducting surface down to a distance of a few Å.

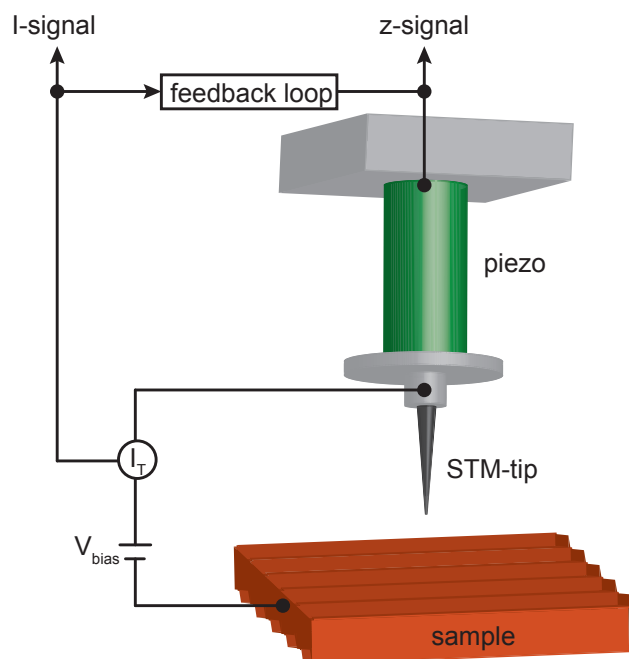


**Figure III.1:** Schematic drawing of the working principle of a scanning tunneling microscope (STM). An atomically sharp tip is approached to a surface until a tunneling current will occur due to the applied bias voltage. A piezo scanner moves the tip across the surface.

When applying a bias voltage, a tunneling current occurs and provides information about the surface. A scanner consisting of a cylindrical crystal of piezo-electric material moves the tip across the surface. Two pairs of electrodes sit on the outside of the piezo element, while the inner side is entirely covered by one electrode. Applying voltages to either one of the outer pairs of electrodes relative to the inner ones, depending on the polarity, will bend the piezo in the corresponding direction and the  $x$  and  $y$  movement is generated. By applying a voltage between the inner and all four outer electrodes, the entire piezo will, depending on the voltage polarity, expand or contract in  $z$ -direction. While scanning across the surface the tunneling current  $I$  and the piezo motion  $\Delta z$  are recorded. There are two different ways of imaging the surface. In both cases, the tip is stabilized at a certain bias voltage and tunneling current. In the constant height mode, the feedback loop of the STM is switched off and the height  $z$  stays constant while scanning along the surface. In the constant current mode the principle is different. The current  $I$  is kept at a constant value, while the feedback loop regulates the height  $z$ . Throughout this work, STM images recorded in the constant current mode will be presented.

In the following Sections, the theoretical background of the working principle of STM and STS with non-magnetic and magnetic tips will be introduced to provide the basis for the interpretation of the experimental data within this work.

### III.1. The One Dimensional Tunneling Effect

Towards the understanding of the basic principle of scanning tunneling microscopy it is helpful to start with taking a closer look at the one dimensional quantum mechanical tunneling effect. Let us consider a finite potential barrier with the height  $V_0$  and thickness  $d$  and a particle that tends to cross this barrier as shown in Fig. III.2.

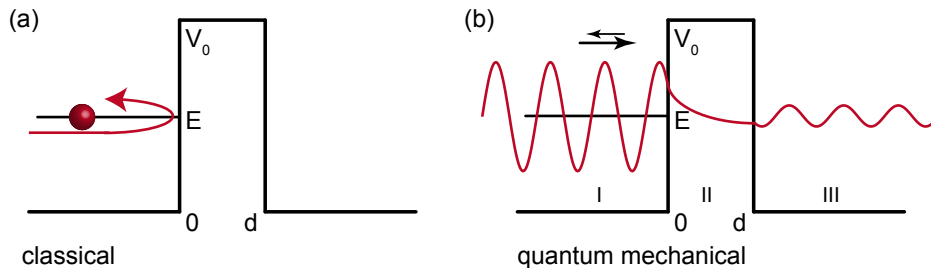


**Figure III.2.:** (a) A classical particle with the energy  $E$  approaching an energy barrier of the height  $V_0$ , with  $V_0 > E$  will be reflected. (b) A quantum mechanical particle, described by a wave function  $\Psi$  with the an energy  $E < V_0$  will have a certain probability to penetrate or even cross (tunnel) through the barrier.

The analogues in scanning tunneling microscopy would be the vacuum gap between tip and sample and the electrons carrying the current. As shown in Fig. III.2 (a) in case the energy of the incoming classical particle is lower than  $V_0$  it will be reflected at the barrier. In the quantum mechanical picture the particle can be described as a wave function  $\Psi(z)$  and thus

has a certain probability to penetrate or even cross the energy barrier (see Fig. III.2 (b)). This probability can be determined by solving the time independent Schrödinger equation.

$$\left( -\frac{\hbar^2}{2m} \frac{d^2}{dz^2} + V_0(z) \right) \Psi(z) = E\Psi(z) \quad (\text{III.1})$$

for the three areas, in front of (I), inside (II) and behind (III) the barrier. The solution for area (I) and (III) in front of and behind the barrier are of the form of plane waves

$$\Psi_{\text{I}}(z) = Ae^{ikz} + Be^{-ikz} \quad (\text{III.2})$$

$$\Psi_{\text{III}}(z) = Ce^{ikz} \quad (\text{III.3})$$

with  $k^2 = 2mE/\hbar^2$ . Whereas inside the barrier of the height  $V_0$ , the wave function will describe an exponential decay

$$\Psi_{\text{II}}(z) = De^{\kappa z} + Ee^{-\kappa z} \quad (\text{III.4})$$

with  $\kappa^2 = 2m(V_0 - E)/\hbar^2$ . For a first estimation of the tunneling current present in the experiment the ratio between transmitted  $|C|^2$  and incoming  $|A|^2$  fraction of the wave is vital, because it can directly be compared to the ratio of transmitted and incident current density and therefore describes the characteristic of the tunneling current. The transmission coefficient

$$T = \frac{|C|^2}{|A|^2} \quad (\text{III.5})$$

can be calculated by determining the coefficients A, C, taking into account the requirement that the wave function and its derivative has to be uniformly continuous. Additionally considering a thick and high barrier ( $\kappa d \gg 1$ ), which is reasonable for typical STM parameters leads to

$$T \approx \frac{16k^2\kappa^2}{(k^2 + \kappa^2)^2} \cdot e^{-2\kappa d}. \quad (\text{III.6})$$

This result is the basis for interpretations of the current in STM. It shows an exponential dependence on both, the thickness of the barrier  $d$  and the effective barrier height ( $\sqrt{\Phi_{\text{eff}}} = \sqrt{V_0 - E}$ ). For reasonable parameters in STM experiments ( $\Phi_{\text{eff}} = 4 \text{ eV}$ ,  $d = 5 \text{ \AA}$ ) it has the consequence that the increase of the barrier thickness by  $\Delta d = 1 \text{ \AA}$  leads to a decrease in tunneling current by one order of magnitude. This result directly exhibits the high sensitivity of the STM to small changes in the topography down to less than a tenth of an  $\text{\AA}$ . Another conclusion which is already possible to be drawn on the basis of this result is the dominance of the first atom at the apex of the tip. Electrons tunneling out of this atom will mainly contribute to the signal, leading to, not only the very high vertical resolution, but also to an atomic resolution in the lateral directions.

By considering the one dimensional tunneling effect it is possible to get a first impression

of the basic mechanisms of the STM, but of course this image is over-simplified. Up to this point the structure of the electrodes was neglected although the atomic and electronic configurations of the two electrodes, namely tip and sample, have to be taken into account to derive a more realistic STM model.

## III.2. Interpreting STM Images

To account for a more realistic description of the tunneling current a theory developed by Bardeen already twenty years before the invention of the STM is applied. Bardeen [37] calculated a system consisting of two planar electrodes separated by an insulating oxide layer by means of first order perturbation theory. Within this theory the two electrodes are considered to be weakly interacting systems and the current is calculated based on the overlap of the wave functions inside the barrier. In 1983 Tersoff and Hamann [38, 39] adopted this theory to the system consisting of tip and sample separated by a vacuum gap. Under the assumption of small biases and low temperatures the tunneling current is given by

$$I = \frac{2\pi}{\hbar} e^2 V \sum_{\mu\nu} |M_{\mu\nu}|^2 \delta(E_\mu - E_F) \delta(E_\nu - E_F). \quad (\text{III.7})$$

Here,  $e$  and  $V$  are the electron charge and the applied bias voltage. The indices  $\mu$  and  $\nu$  denote tip and sample, respectively. The delta-functions account for elastic tunneling of the electrons that means that the energy of the electrons is conserved during the tunneling process. The basic challenge when trying to apply Eq. (III.7) is the determination of the tunneling matrix element  $M_{\mu\nu}$ . It describes the transition of the states  $\Psi_\nu$  of the sample before tunneling and of the states  $\Psi_\mu$  of the tip after the tunneling process.  $M_{\mu\nu}$  depends on the energy levels and wave functions of sample and tip and can according to Bardeen be written as

$$M_{\mu\nu} = -\frac{\hbar^2}{2m} \int d\vec{S} (\Psi_\mu^* \vec{\nabla} \Psi_\nu - \Psi_\nu \vec{\nabla} \Psi_\mu^*). \quad (\text{III.8})$$

Information about the exact energy levels and wave functions can only be obtained, if detailed information about the structure of the electrodes can be provided. This is especially in the case of the tip not possible. The tip is fabricated in a relatively uncontrolled way, mainly ex-situ, and detailed information can only be achieved for example by means of field emission microscopy with high efforts. Additionally the tip apex undergoes various changes, again in an uncontrolled manner, while recording the data during the experiment itself. To avoid being forced to provide detailed information about the tip apex additional assumption were introduced by Tersoff and Hamann. They proposed the tip sample geometry shown in Fig. III.3 with the tip representing a perfect spherical shape at the apex with the curvature  $R$  and the distance  $d$  from the surface. The position of the tip is given by  $\vec{r}_0$ . This proposal seems reasonable, when taking into account that the first atom at the tip apex, due to the exponential dependence of the current on the distance, is mainly contributing to the signal.

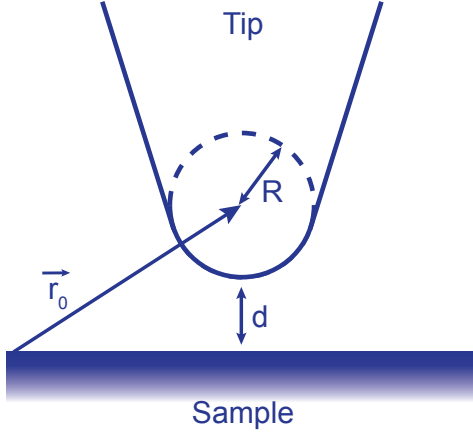


**Figure III.3:** Schematic drawing of the tip-sample geometry. The tip is approximated by a spherical shape with the radius  $R$  at the apex [39].

Furthermore only tip wave functions of the form of  $s$ -waves are considered to be present in the tunneling process.<sup>1</sup>

These further assumptions leads to a determination of the tunneling matrix element and modify the tunneling current to

$$I \propto V n_t \exp(2\kappa R) \sum_{\nu} |\Psi_{\nu}|^2 \delta(E_{\nu} - E_F), \quad (\text{III.9})$$

in which  $n_t$  is the constant density of states of the tip at the position  $\vec{r}_0$  and at the Fermi level. Furthermore one can identify the second part of Eq. (III.9)

$$n_s(\vec{r}_0, E_F) = \sum_{\nu} |\Psi_{\nu}|^2 \delta(E_{\nu} - E_F) \quad (\text{III.10})$$

as the local density of states (LDOS) of the surface at the Fermi energy. Equations (III.9) and (III.10) demonstrate two main features of the theory introduced by Tersoff and Hamann. First of all the role of the tip is reduced to simply being a probe of the sample characteristics and its contributions to the energy dependence of the tunneling current are neglected. And second, the results of the in the introduction of this Chapter already mentioned constant-current imaging, in which the tip is scanned across the surface by regulating the distance to keep the current constant, can be interpreted as maps of contours of constant local density of states of the sample. In a first approximation, these LDOS images are considered to reflect the topography of the sample surface. This approximation holds as long as the geometrical structures dominate over the electronic structures. On the atomic scale, the LDOS images can not longer be considered to reflect topographic features, but the orbital character of the electron wavefunctions. As a result, depressions instead of protrusions might appear in atomic resolution images at the

<sup>1</sup>This immediately opens up questions regarding magnetic tips for spin-polarized STM, in which the  $d$ -orbitals are carrying the magnetic information necessary to achieve signals based on the tunneling magnetoresistance.

positions of the atoms. STM is therefore widely and mainly used as a tool to investigate surface structures, which were before the invention not accessible with techniques like low energy electron diffraction or other tools, which are based on diffracted particle or electro-magnetic waves. Attention has to be paid when imaging surfaces with atomic resolution. The measured and calculated corrugations strongly differ. Chen [40] solved this discrepancy in the Tersoff-Hamann model with developing an extended theory, where he included tip orbitals of lower symmetry, e.g.  $d_z^2$ . Furthermore the interpretation of adsorbates on surfaces or surface alloys has to be made with the knowledge that it is not the topography that is measured in STM, but contours of constant LDOS. Due to their different work functions, oxygen adsorbates on metallic surfaces for example appear as depressions on the surface although they are protrusions from the topographic point of view.

While it was in the beginning mainly used as a tool to investigate the surface structure, the sensitivity of STM to the local electronic density of states of the sample opens up the possibility to investigate the electronic properties including magnetic properties of surfaces and is now widely used in this research area. In the next Section it will be shown that STM is best suited to probe the local density of states for occupied, but also unoccupied states of the investigated sample.

### III.3. Probing the Local Density of States

Scanning tunneling spectroscopy (STS) offers the possibility to investigate the LDOS structure of a sample with lateral atomic resolution. It will be shown in this Section that the differential conductivity of the sample  $dI/dV$  as a function of the applied bias voltage  $V$  provides the information about the density of states.

In the approximations made in the last Section, only vanishing bias voltages were included. Now the theory will be extended to account also for finite bias voltages. The result of the Tersoff-Hamann tunneling current in Eq. (III.7) is then modified to

$$I \propto \int_0^{eV} n_t(\epsilon - eV)n_s(\epsilon)T(\epsilon, eV)d\epsilon, \quad (\text{III.11})$$

in which the net current originates from a convolution of the densities of state of tip and sample over the energy interval  $eV$ . The transmission coefficient, similar to the one introduced in Eq. (III.5) accounts for the exponential bias voltage and energy dependence of the tunneling current.

For a better understanding, Fig. III.4 visualizes the content of Eq. (III.11) on the basis of one dimensional energy diagrams. Tip and sample are considered to exhibit different work functions  $\Phi_t$  and  $\Phi_s$  and the density of states of the tip is according to the approximations made in the model supposed to be constant. The magenta line represents the density of states of the sample. At high distance, as plotted in Fig. III.4 (a), the two systems do not interact with each other. By bringing the two electrodes in tunneling contact, electrons are tunneling in both directions until the combined system is in equilibrium, which means the Fermi levels are located at the same energy [Fig. III.4 (b)]. An applied bias voltage

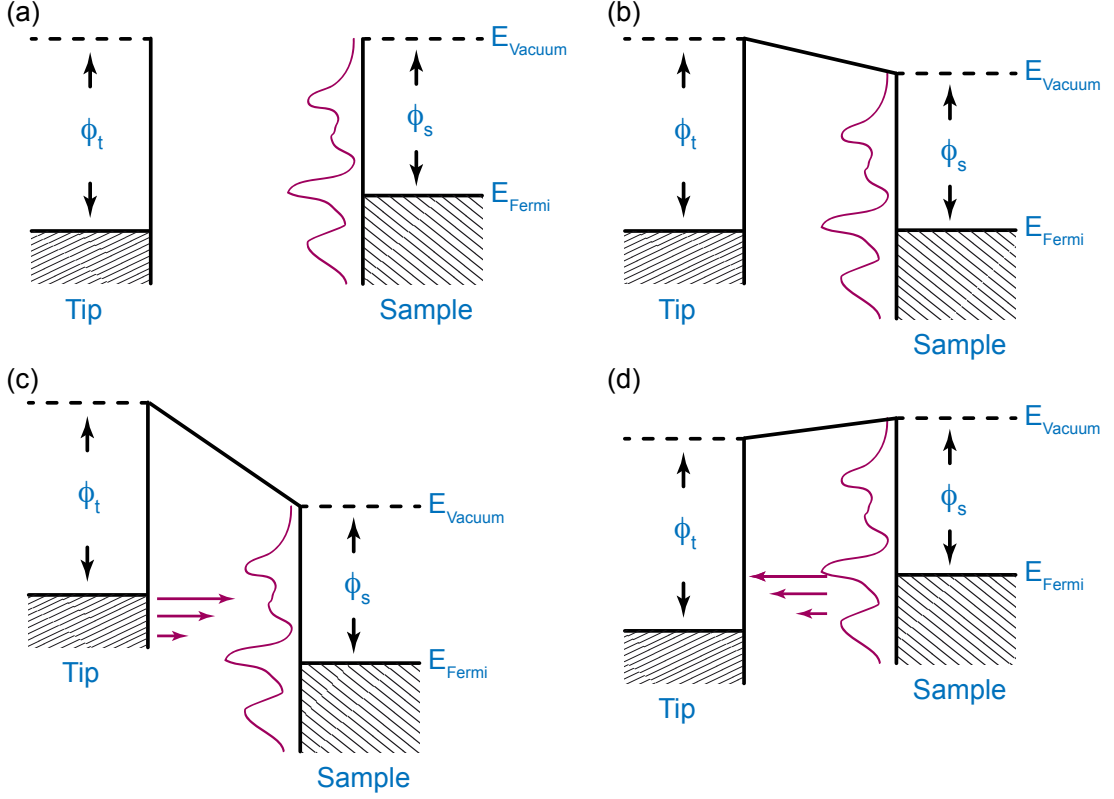


**Figure III.4.:** Sketch of the energy diagrams for a tunneling system. The sample DOS is indicated as a wavy line, whereas the DOS of the tip is considered to be featureless (constant). (a) Tip and sample in high distance from each other: No interaction. (b) Tip and sample in tunneling contact. Electrons are tunneling until both Fermi levels are in equilibrium. (c) Positive bias voltage at the sample. Electrons are tunneling from the tip to the sample, which results in probing the unoccupied sample states. (d) Negative bias at the sample. Electrons are tunneling from the sample to the tip, which results in probing the occupied sample states (as in [41]).

$eV$  will shift the Fermi energy of one electrode with respect to the other and electrons tunnel from the negative to the positive electrode. In Fig. III.4 (c) a negative bias voltage is applied to the tip and electrons tunnel into unoccupied states of the sample, whereas in Fig. III.4 (d) electrons tunnel from occupied states of the negatively biased sample into the tip. The plotted arrows of different length represent the influence of the transmission coefficient  $T(\epsilon, eV)$ . Electrons, which are located at the Fermi edge of the negatively biased electrode contribute most to the tunneling current. This can be intuitively understood by considering that they have to overcome the smallest energy barrier.

If we now in a further step differentiate Eq. (III.11) with respect to  $V$

$$\frac{dI}{dV}(V) \propto n_t(0)n_s(eV)T(eV) + \int_0^{eV} n_t(\epsilon - eV)n_s(\epsilon)\frac{dT(\epsilon, eV)}{dV}d\epsilon \quad (\text{III.12})$$

the correlation between the differential conductivity  $dI/dV$  and the LDOS of the sample becomes evident and can be attributed to the first term. The second term represents the influence of the bias voltage dependence of the transmission coefficient  $T(\epsilon, eV)$  and will appear in the STS experiment as a background on the signal. Different approaches to eliminate this background have been proposed [42,43], but are not discussed and used in this work. The appearance of the transmission coefficient in the first term gives rise to an asymmetry in the  $dI/dV$ -signal, when changing the bias polarity. To explain this in detail, Figs. III.4 (c) and (d) are taken into account again. Probing the unoccupied states of the sample in STS is favored, because the electrons are tunneling from the Fermi edge of the tip, where the efficiency is highest (indicated by the long magenta arrow), into states at an energy  $E_F + eV$ . In contrast to this, probing the occupied sample states means that electrons which lie deeper in energy and thus, exhibit lower tunneling efficiency, generate the tunneling signal. In view of these considerations, the assumption that the LDOS of the tip is flat becomes questionable. However, experimental results show that it is still applicable. Nevertheless it is also possible to eliminate the influence of the tip from the signal. This can be done by recording STS data at different sample positions, at which the LDOS of the sample is known to change, but the contribution of the LDOS of the tip is known to be unaltered. In conclusion the  $dI/dV$ -signal reveals the LDOS features of the sample and can be addressed in STS with the already mentioned high lateral atomic resolution intrinsic for STM.

The spectroscopic  $dI/dV$ -data shown in this work is obtained in the following experimental approach. A lock-in amplifier is used to add a small bias voltage modulation with a frequency higher than the cut-off frequency of the feedback loop ( $\Delta V = 20$  mV,  $f = 2.7$  kHz) to the applied bias voltage  $V$ . The resulting in-phase current modulations are detected by the same lock-in amplifier. The  $dI/dV$ -signal by this means detected is attributed to the LDOS of the sample. The spectroscopic data is displayed in two different ways, depending on the requested information. On the one hand the LDOS for a certain bias voltage  $V$  is plotted in a two dimensional image to show the spatial distribution of the contributing states of the LDOS at the energy  $E_F + eV$ , which is then called a  $dI/dV$ -map. On the other hand the LDOS is plotted for a particular sample position as a function of the applied bias  $V$  to gain information about the energy dependency, which is called  $dI/dV$ -curve.  $dI/dV$ -maps and constant current STM images are always recorded simultaneously. This offers the potential to directly compare spectroscopic properties to topographic features. In case of the  $dI/dV$ -curves, the tip is moved to a selected sample position and stabilized at certain bias voltage-tunneling current values. During the acquisition of the spectra, the feedback loop is switched off and the bias voltage is swept within the chosen interval, while the lock-in amplifier detects the  $dI/dV$ -signal.

#### III.4. Spin-Polarized Tunneling Experiments

As already mentioned in the introduction to this Chapter, STM opens up the additional possibility to investigate not only the electronic, but also the related magnetic properties of surfaces. Therefore it is necessary to include the electron spin into the considerations so



far taken about the tunneling current. In 1989 Slonczewski [44] discussed the problem of electrons tunneling between two ferromagnetic electrodes and showed the cosine dependence of the tunneling current with respect to the relative alignment of the two magnetization directions of the electrodes ( $\Theta$ ). Under the assumption of vanishing bias voltages and electrons behaving like free electrons within the conduction band, the tunneling current can be expressed

$$I_{\text{sp}} = I_0[1 + P_1 \cdot P_2 \cos \Theta], \quad (\text{III.13})$$

with  $I_0$  being the spin-averaged current and  $P_i = \frac{n_{i,\uparrow} - n_{i,\downarrow}}{n_{i,\uparrow} + n_{i,\downarrow}}$  the spin-polarization, in which  $n_{i\uparrow/\downarrow}$  are the densities of states of the spin up and spin down electron states at the Fermi energy, respectively. The cosine- $\Theta$  dependence of the tunneling current is shown in Fig. III.5 observed for tunneling junctions consisting of Fe-Al<sub>2</sub>O<sub>3</sub>-Fe layers.

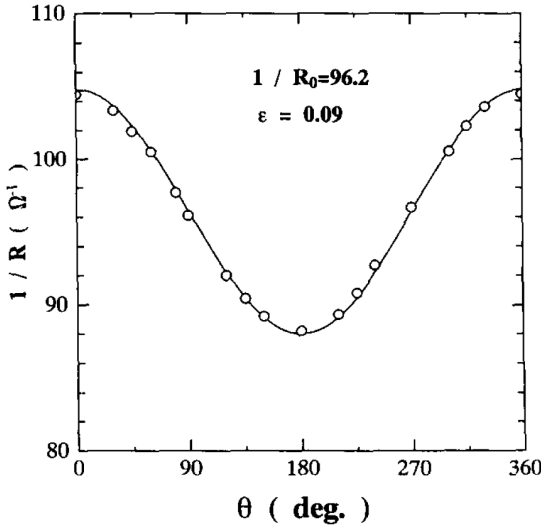


**Figure III.5:** Dependence of the magnetoresistance on the relative angle between the two magnetization directions of a planar tunneling junction consisting of Fe-Al<sub>2</sub>O<sub>3</sub>-Fe [45].

If the relative alignment of the two electrodes is 90°, there will be no change of the tunneling current by reversing the magnetization direction of either tip or sample, whereas a change of the relative alignment of 180° will lead to the maximum contrast. The spin-polarized tunneling was already verified by Jullière in 1975 [46] in Fe-Ge-Co junctions.

In ferromagnetic materials the band structure is split into a minority and majority band as shown in Fig. III.6. Due to the exchange energy splitting it comes to a replacement of electrons from the minority spin band into the majority spin band. The bands exhibit different values of density of states  $n_{i\uparrow/\downarrow}$  at the Fermi level resulting in a spin-polarization  $P_i$  at  $E_F$ . If we consider a tunneling junction consisting of two electrodes of the same material as shown in Fig. III.6, electrons will tunnel from one electrode (tip) to the other (sample), if a positive bias voltage is applied to the sample. Since the tunneling probability depends on the number of states available at the Fermi level (see Eq. (III.12)), the case of parallel alignment of the two magnetization directions, shown in Fig. III.6 (a), will lead to a higher tunneling current, than the opposite case of antiparallel alignment in III.6 (b).

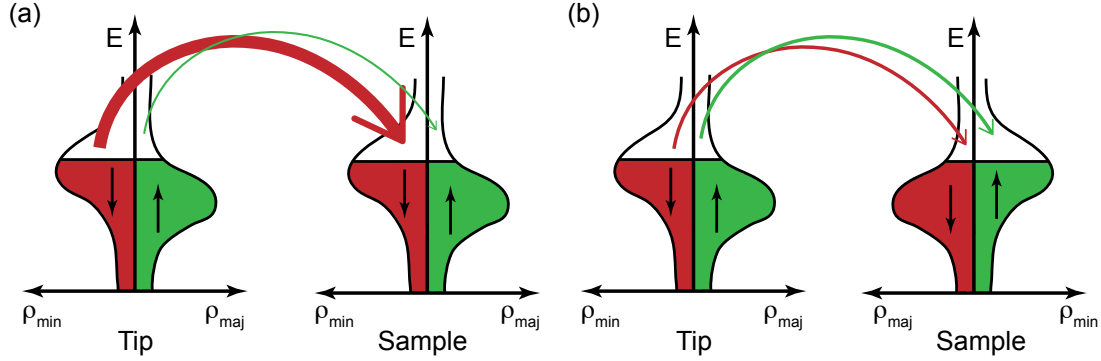


**Figure III.6.:** Jullière model of the spin-polarized tunneling in a tunneling junction consisting of identical electrodes. In the parallel magnetization configuration of the two electrodes (a) a high tunneling current is detected whereas in the antiparallel configuration (b) a lower current is observed.

The result is a detectable contribution to the tunneling current in STM depending on the relative alignment of the magnetization of tip and sample.

In this way it is possible to understand the mechanism of spin-polarized tunneling and the tunneling current derived by Tersoff and Hamann can be extended [47] to account for spin-polarized tunneling. Again, the density of states of the tip is supposed to be constant ( $n_{t,\uparrow}, n_{t,\downarrow} = \text{const.}$ ), but unequal for both spin directions ( $n_{t,\uparrow} \neq n_{t,\downarrow}$ ) and the density of states of the sample depends on the position and bias voltage. For the energy integrated local density of states  $\tilde{n}_s(\vec{r}_0, V)$  and energy integrated local spin density of states  $\tilde{m}_s(\vec{r}_0, V)$  of the sample in the interval  $[E_F; E_F + eV]$  follows

$$\tilde{n}_s(\vec{r}_0, V) = \tilde{n}_{s,\uparrow}(\vec{r}_0, V) + \tilde{n}_{s,\downarrow}(\vec{r}_0, V) \quad (\text{III.14})$$

$$\tilde{m}_s(\vec{r}_0, V) = \tilde{n}_{s,\uparrow}(\vec{r}_0, V) - \tilde{n}_{s,\downarrow}(\vec{r}_0, V). \quad (\text{III.15})$$

The tunneling current including spin-polarized tunneling then derives to be

$$I(\vec{r}_0, V, \Theta) \propto n_t \tilde{n}_s(\vec{r}_0, V) + m_t \tilde{m}_s(\vec{r}_0, V) \cos \Theta(\vec{r}_0) \quad (\text{III.16})$$

and a differentiation with respect to the bias voltage results in

$$dI/dV(\vec{r}_0, V, \Theta) \propto n_t n_s(\vec{r}_0, E_F + eV) + m_t m_s(\vec{r}_0, E_F + eV) \cos \Theta(\vec{r}_0). \quad (\text{III.17})$$

Regarding Eq. (III.16), the magnetic information will add to the topographic signal described via the first term of Eq. (III.16) in a constant current STM image. With increasing voltage the spin averaged topographic signal in the first term will also increase, whereas the magnetic signal stays constant. Since the quantities are energy integrated values, the magnetic signal may even decrease, if by chance the integration is carried out over states of

opposite spin-polarization. In a measurement of the differential conductivity described in Eq. (III.17), the signal is spin and energy resolved, so that an identification of the energy ranges of the spin-polarized states is possible when recording spin-polarized STS-curves as introduced in the last Section. Attention has to be paid at negative bias voltages, where the efficiency of tunneling is lower and the impact of the density of states of the tip and particularly the energy dependent spin-polarization of the tip might influence the signal. Furthermore, it is possible to make use of the spatially resolved  $dI/dV$ -maps at bias voltages with high spin-polarization, to compare the magnetic information to the topographic constant current STM images recorded simultaneously.



---

## Experimental Methods

---

This Chapter gives an overview of the experimental methods used for the STM measurements on single molecules adsorbed on surfaces and the spin-polarized STM investigations with bulk chromium tips presented in the following Chapters. At first, the vacuum chamber, in which the experiments were performed is introduced and the main parts are described briefly. Afterwards a description of the preparation of the different crystalline substrates is given. One of the essential parts in scanning tunneling microscopy is the reproducible preparation of STM tips. In this work, both tungsten and chromium bulk tips are used. The use of bulk tungsten tips is well known in STM and will therefore only be mentioned briefly, whereas the application of antiferromagnetic bulk chromium tips has only recently been started in the community and opens up room for discussion and further experimental investigation. These results are presented in detail in this Chapter. In the end, the details of the deposition of the single molecules onto the clean substrate are presented.

### IV.1. Vacuum System

All the data presented in this thesis was measured inside the ultra high vacuum (UHV) chamber described in this Section. Figure IV.1 shows a schematic drawing of the UHV chamber called the NanoSpintronicsClusterTool. It comprises four separated, but connected chambers for in-situ preparation and characterization of samples used for UHV investigations. The description of the instrumentation is restricted to the components relevant for this work.

1. Scanning Electron Microscope (SEM)

The SEM-chamber is used to characterize tips for scanning tunneling microscopy with a resolution down to a few tens of nanometers. Though this resolution, is not sufficient to gain insight into the part of the tip-apex that is responsible for tunneling, it is still a powerful method to investigate the influence of etching rates and electron beam heating on the tip, regarding for instance roughness and adsorbates.

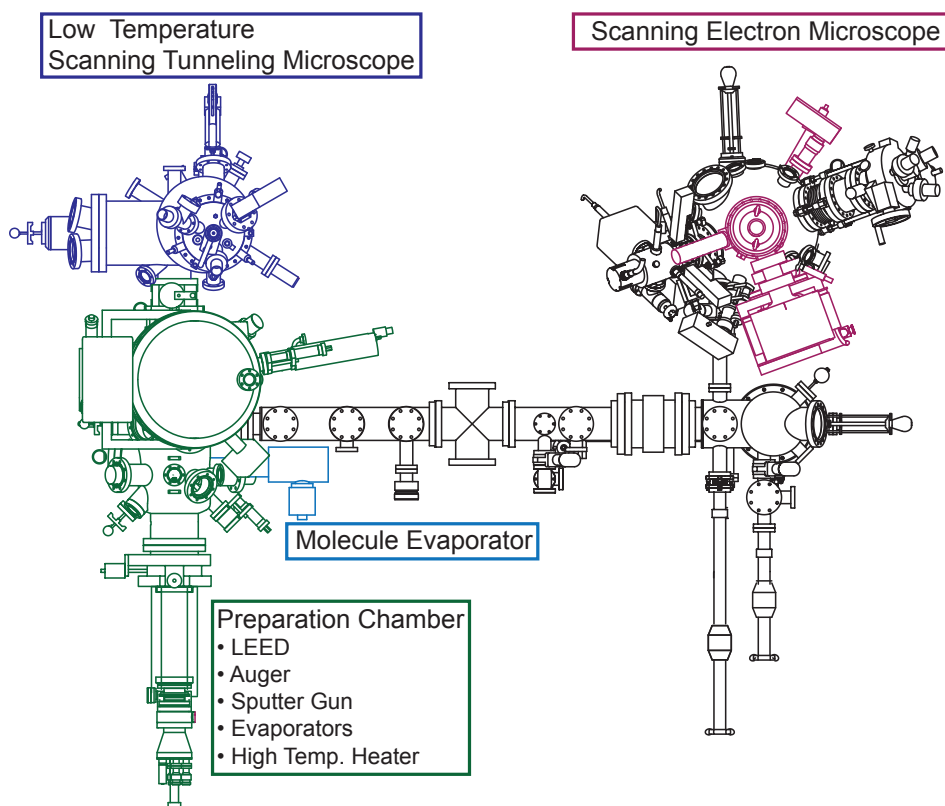


**Figure IV.1.:** Schematic drawing of the NanoSpintronicsClusterTool.

## 2. Preparation Chamber

The preparation chamber is used for preparation and characterization of the several samples used in the course of this work. Various methods are available, such as argon sputtering, high temperature heating (for tungsten crystals), electron beam evaporators for the deposition of iron, low energy electron diffraction (LEED) analysis and Auger electron spectroscopy.

## 3. Molecule Evaporator

The molecule evaporator for depositing single molecules on surfaces is directly connected to the preparation chamber, but separated by a valve and pumped by an additional turbo pump. This allows for initial degassing of the molecule powder without affecting the pressure in the main preparation chamber.

## 4. Low Temperature Scanning Tunneling Microscope (LT-STM)

The Omicron LT-STM is connected directly to the preparation chamber and separately pumped. The STM head is cooled via two bath cryostats with either only liquid nitrogen or both liquid nitrogen and liquid helium. Counter heating for variable

temperatures is possible. All measurements presented in this work were performed at 4.8 K.

## IV.2. Tip Preparation

The main experimental issue lies on the reproducible preparation of sharp STM tips for the investigation of surfaces on the atomic scale. In case of non-spin-polarized STM, the use of tungsten tips is most common. Therefore polycrystalline W wires of the desired thickness are commercial available and in most cases ex-situ chemical etching is applied to fabricate sharp tips. In the first part of this Section, the preparation of W-tips used in this work is presented. For spin-polarized STM investigation the situation becomes even more complex and is discussed in detail in the second part of this Section.

### IV.2.1. Tungsten Tips

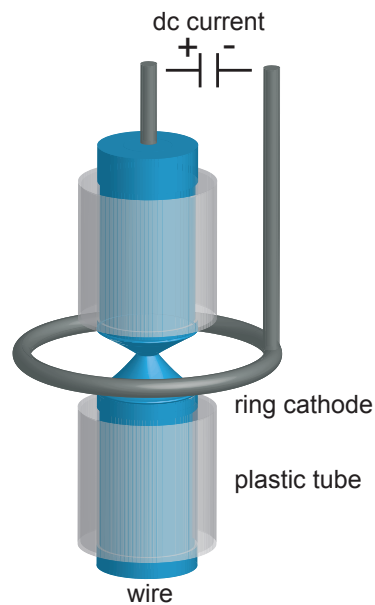
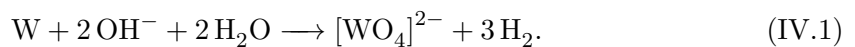


**Figure IV.2:** Setup for electrochemical wet etching of STM tips. A constant current is applied between the ring cathode and the tip. Plastic tubes prevent the tip from being etched in unwanted regions.

In this work, the W-tips are ex-situ electrochemically etched from bulk wires with diameters of 3.8 mm. As shown in Fig. IV.2, plastic tubes are attached around the wire, leaving a small defined opening in which the etching takes place. By means of surface tension, 5 molar NaOH forms a thin film in a ring-like platinum cathode. The ring, filled with NaOH, is positioned around the opening of the two tubes. Depending on the desired tip shape, different dc-currents are applied between the tip and the ring-like cathode to achieve different etching rates. The equation for the chemical reaction is



Metallic tungsten is oxidized to tungstate while gaseous hydrogen is produced at the cathode. The etching process automatically stops once the wire is entirely etched. Due to its weight, the part of the wire, later used as STM tip, falls down into a small collecting tray. The defined stop of the etching process ensures a very sharp apex of the tip.

After the wet etching process, the tips are mounted on the tip carriers and transferred into the vacuum. To remove the oxygen layer that formed on the tungsten tips during the ex-situ etching and the exposure to air, the tips are flashed by electron beam heating: electrons emitted by a glowing tungsten filament are accelerated onto the tip that lies on a high positive potential of 1 kV. The influence of the heating can be imaged by the SEM before and after treatment, respectively. Figure IV.3 shows the evolution of a W-tip in the process of several heating cycles.

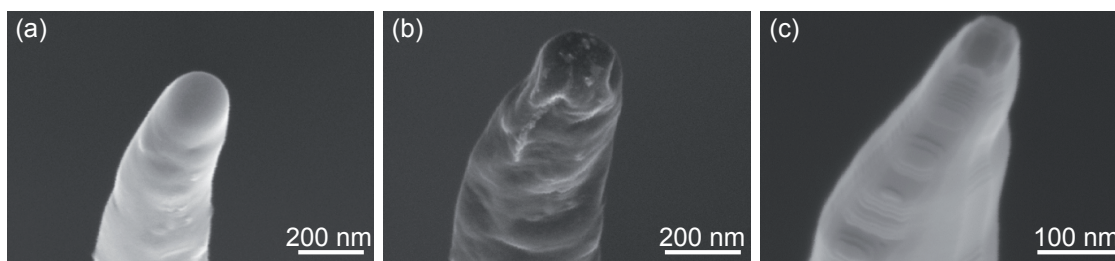


**Figure IV.3.:** SEM images of a flash cycle of a W-tip. (a) tip before flashing, (b) after short flash for 6 s at  $P = 1.6$  VA and (c) after flashing for 18 s at  $P = 8.6$  VA.

Immediately after the transfer of the tip into the ultra high vacuum, the tungsten surface appears bright and smooth as shown in Fig. IV.3 (a). After a short heating cycle at 1.6 VA power for 6 s, shown in Fig. IV.3 (b), the surface becomes darker with small bright areas. In addition the shape of the tip is altered because the tungsten melts at the surface. Bright colors in contrast to darker regions in SEM indicate non conductive areas on the tip, which are attributed to oxidized tungsten. This indicates that the first short flash already removed most of the oxygen initially located on the tip. After an additional electron bombardment at higher heat load (18 s at  $P = 8.6$  VA) a drastic change of the shape of the tip apex is observed. The tip radius approximately reduces to the half of the initial value. (Note: the magnification in Fig. IV.3 (c) is higher compared to (a) and (b).) In addition the surface appears in a homogenous light color indicating the complete removal of oxides. In conclusion, the application of electron beam heating to tungsten tips results into a removal of the oxygen that could otherwise possibly complicate taking STM images and alters the radius of the tip in a way that sharper STM images may be obtained. In the following, W-tips are used for the investigation of the NdPc<sub>2</sub> molecule on Cu(100) in Chapter VI.

### IV.2.2. Chromium Tips

For the investigation of the magnetic properties of surfaces with lateral resolution down to the atomic scale, the choice and preparation of tips from suitable materials is crucial. From the formulas derived in Chapter III it is concluded that the  $dI/dV$  signal recorded in the STM



investigations of magnetic surfaces scales with the scalar product of the two magnetization vectors of tip and sample  $\vec{m}_t \cdot \vec{m}_s$ . Depending on the direction of the magnetization of the tip, it therefore can be sensitive to certain directions of the magnetization of the sample. Since the scalar product can also be written as the cosine of the relative angle between the two magnetization vectors, it will vanish in case of perpendicular alignment. In early times of spin-polarized STM measurements tips made from ferromagnetic bulk materials, like Ni, Fe or Co [48–50], or tips coated with ferromagnetic materials like Fe [51] were mainly used for SP-STM. Due to the fact that most of the tunneling current has its origin at the very end of the tip apex, it is also possible to use tips made from antiferromagnetic materials. These tips do not show a net magnetization because of their antiferromagnetism. However, single atoms carry a magnetic moment and spin-dependent tunneling occurs at the apex of the tip. It has been shown that the use of antiferromagnetic probes has advantages compared to ferromagnetic tips, since the stray field of the latter can influence the magnetic properties of the surface during the measurement [52]. One suitable antiferromagnetic material is chromium, because it has a Néel temperature of 311 K [53], lying above room temperature, so the experiment has not necessarily to be done at cryogenic temperatures. Previous experiments with ex-situ electrochemically etched tungsten tips which were coated with Cr after the transfer into the vacuum chamber showed in-plane sensitivity [52]. The in-situ preparation step of the STM tip is tedious, since the ideal chromium thickness that has to be achieved is in the range of 35 atomic layers [54]. Attempts to achieve magnetic contrast in the STM investigations of Fe on W(110) with chromium coated tips during this work did not lead to the desired results. Whether the limiting factor was the magnetic sample or the tip itself could not be sorted out. To reduce the additional effort concerning the in-situ evaporation of chromium layers on the tungsten tips, we changed to Cr-tips fabricated from bulk material. The possibility to achieve spin-contrast and atomic resolution in STM with tips made from bulk chromium has only recently been shown [55, 56]. Here the tips were ex-situ electrochemically etched, either followed by no in-situ preparation steps as done by Bassi *et al.* [55] or by applying short voltage pulses up to 10 V between tip and sample as done by Schlenhoff *et al.* [56]. By the time these two groups performed their experiments, it was not possible to purchase thin chromium rods. The production of thin uniform rods is in general challenging, due to the brittleness of pure chromium. Therefore the rods had to be cut from thin Cr sheets and uniformities in the sheet thickness could lead to bad aspect ratios of the resulting tip [55]. It is now possible to purchase thin uniform Cr rods with a diameter of 0.5 mm and a purity of 99.95%. These rods are then in our laboratory electrochemically etched in NaOH solution following the well established procedure for tungsten wires, in detail described above, and immediately transferred into the vacuum chamber. Figure IV.4 shows scanning electron microscopy images of two different Cr-tips etched in the same 5 mol NaOH solution with different etching durations.

The tip in Fig. IV.4 (a) exhibits smaller facets and smoother facet edges than the tip in (b). This can be a result of the longer etching at higher currents in case of the tip in (b)

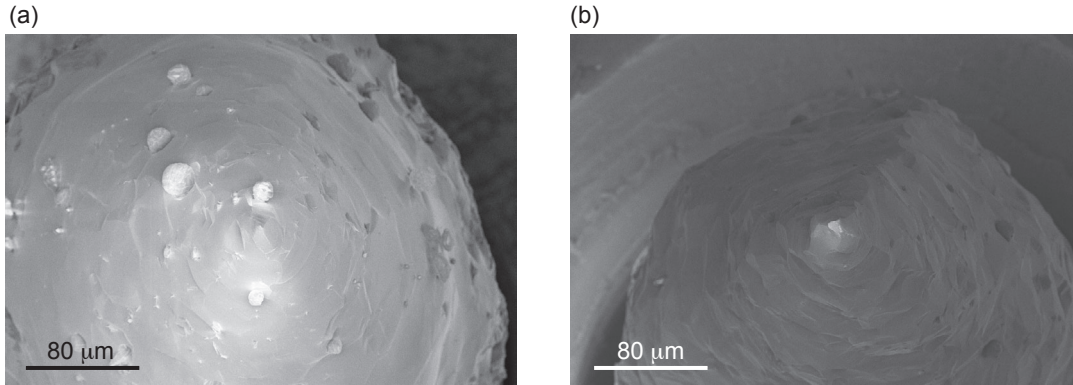
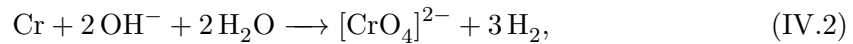


**Figure IV.4.:** SEM images of two different Cr-tips after the chemical wet etching in 5 mol NaOH. The two tips show different facet sizes due to the different etching rates. The tip in (a) was etched for longer time at smaller dc currents and shows smaller facets, whereas the tip in (b) was etched at higher dc currents for longer times. [(a) 1 min at 31 mA + 2.5 min at 20 mA + 9 min at 10 mA, (b) 2 min at 31 mA + 5 min at 20 mA + 2.5 min at 10 mA]

compared to (a). An explanation is given by the chemical equation of the reaction. During the etching process



gaseous hydrogen is produced. The hydrogen, together with the yellow colored Cr(VI), can be observed during the etching of the tip. Hydrogen bubbles are formed and accumulate close to the Cr rod. Higher etching currents generate larger bubbles. If a hydrogen bubble sticks to the rod, it locally prevents it from being etched as long as it stays there. The larger the bubble the larger the protected area. Since smaller facets are observed together with etching for a longer duration at lower currents, it is most likely that the size of the hydrogen bubbles have an influence. This influence on the shape of the tips has been observed before by Mc Kendry *et al.* [57]. Smoother tip shapes are in general favored and give better experimental results, so that in this work the Cr-tips have been etched at lower currents.

After transferring the Cr-tips into the UHV chamber, they are directly mounted in the STM and images on the magnetic surface are taken without further in-situ preparation steps. More than 80% of the fabricated tips show sensitivity to the surface magnetization. In contrast to what was observed before, the tips are mainly sensitive to the out-of-plane components of the surface magnetization. Schlenhoff *et al.* [56] observed sensitivity to both, in and out-of-plane components of the surface magnetization and Bassi *et al.* [55] reported solely in-plane contrast, but it is important to note that the out-of-plane component could not be observed since the investigated antiferromagnetic Cr(001) surface is not likely to exhibit an out-of-plane magnetization component. These variations of the tip sensitivity are not surprising, since the actual atomic configuration at the tip apex is in general unknown and can be arranged in a way that the magnetization of the apex atoms is tilted

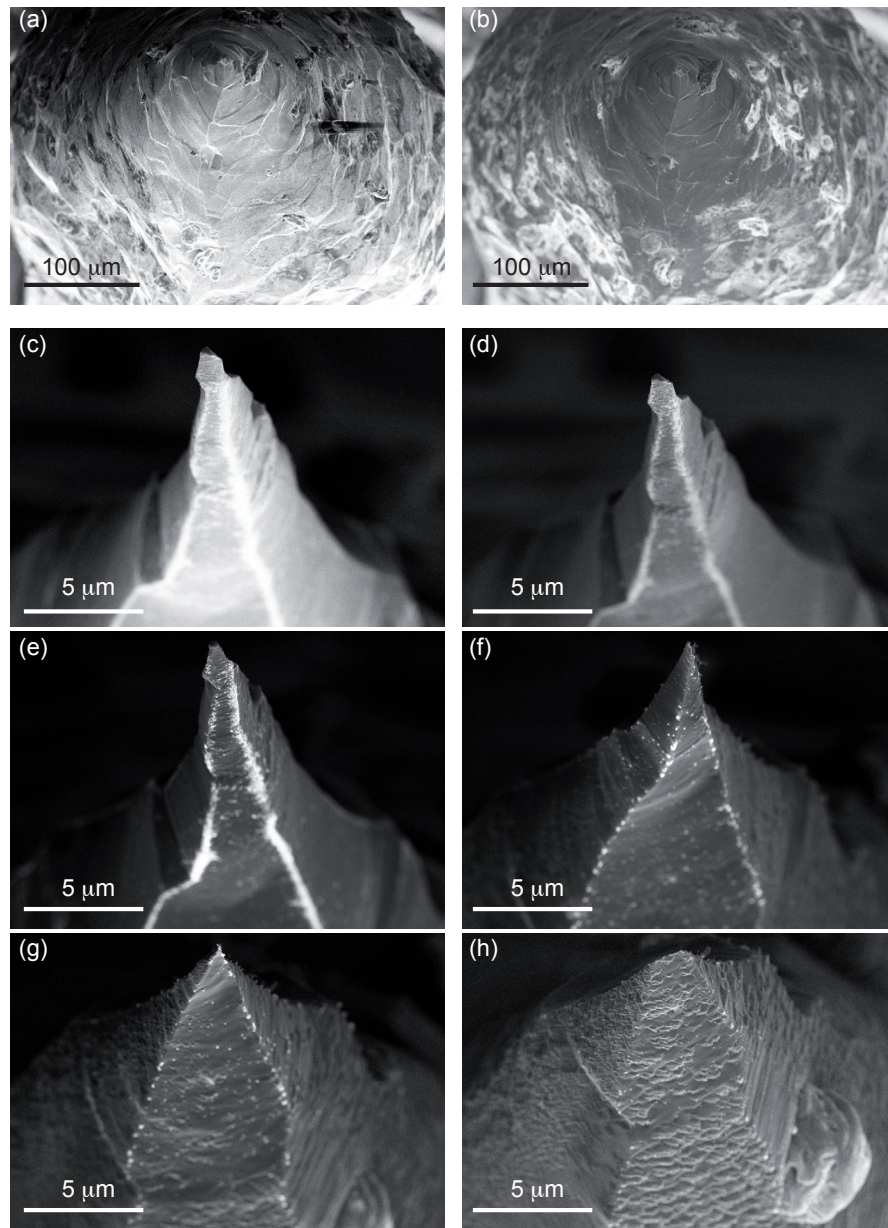


**Figure IV.5.:** SEM images of Cr-tips, showing the influence of the electron bombardment. In (a) and (b) a tip is shown before and after a flash for 30 s at a power of 1.75 VA. The bright contaminations on the upper part of the tip are removed. (c)-(h) show the evolution of the un-flashed tip in (c) after five heating circles. Amount and kind of contaminations are changed together with a strong modification of the tip shape.(d) 10 s at 1 AV, (e) 10 s at 2 AV, (f) 20 s at 2 AV, (g) 30 s at 2 AV, (h) 30 s at 1.5 AV

towards the normal direction of the sample surface. Both, in and out-of-plane as well as intermediate sensitivity, can be explained in this way. As described in the context of tungsten tips, it is possible to apply electron beam heating to the apex of the tip to remove possible contaminations or to enhance the STM resolution by sharpening the apex. The influence of the electron beam heating on the shape and the magnetic properties of the Cr-tips were therefore investigated. Electron bombardment was applied to tips that showed magnetic sensitivity immediately after being transferred into the vacuum, but also to tips that did not show contrast before. After the heating cycle, no statistically firm result could be observed. Tips that were sensitive in the beginning stayed sensitive or lost sensitivity and tips that showed no contrast before became sensitive or stayed in their initial state. Thus, concerning the magnetic properties of the different tips, no final conclusion about the correlation between the magnetization and the applied heating can be drawn.

Figure IV.5 shows the influence of the electron bombardment on the tip. Only the upper part of the tip is influenced by the electron beam, as shown in Fig. IV.5 (a) and (b). The image in (a) was taken, after the transfer of the tip into the vacuum, whereas image (b) was taken after a flash for 30 s at a power of 1.75 VA. Before the flash, the tip all over appeared in the same bright color. Bright colors indicate non-conducting areas of the surface. These bright areas are removed from the upper part of the tip after the electron flash, which might indicate that a possible oxide layer is removed. For a closer look on the influence of the heating at the apex of the tip images were taken after several subsequent heating cycles at different power and for different durations. Figure IV.5 (c)-(h) shows the evolution of the tip apex after five heating cycles. Before the first flash in (c), the tip appears smoothly bright, indicating again non-conducting areas that formed during the wet etching process on the surface. After the first electron bombardment for 10 s at 1 AV shown in (d), the shape of the tip remains unchanged, but the color contrast changes. The flat areas change to darker contrast, whereas the edges still appear bright. This difference in contrast becomes even more dominant after an additional flash for 10 s at 2 AV shown in (e). It seems that the contaminations stick tightly to the edges or that contaminations migrate preferentially at the edges from the bulk to the surface at these temperatures. Additional to the contrast development, small modifications in the tip shape are observed at the apex. The material most likely melted due to the applied heat. After the next electron beam heating for 20 s at 2 AV in (f), the shape of the tip changes drastically and the edges are almost free from the bright contaminations as compared to (e). Applying another electron flash for 30 s at 2 AV in (g) again drastically alters the shape, but almost no influence on the contaminations is observed. It has to be noted at this point that in the last two cycles, the duration but not the power was increased. In the last image (h), in which a flash at lower power (1.5 AV) but again with a longer duration (30 s) was applied to the tip, two different modifications are observed. Besides the again drastic change of the shape of the tip, an evolution of the side walls occurs. Bright structures appear layerwise, whereas the layers seem to be related to the chromium growth. These bright structures might be contaminations migrating from the bulk to the surface due to the applied heat. This study of the heat related evolution of the shape of the tip and the contaminations sticking to the

surface of the tip is used to assist choosing suitable electron beam parameters. In the first place it is most important to remove the contamination layer only. The modification of the tip shape is only necessary, in case the tip showed no proper tunneling behavior in the STM experiment. Therefore, we decided to use parameters, which are close to the values of the tip flashes shown in (d) and (e), for which only minor modifications of the shape are observed.

### IV.3. Sample Preparation

This Section gives an overview about the preparation of the samples used in the course of this work. Single molecule studies of  $\text{NdPc}_2$  were performed on several substrates, i.e.  $\text{Cu}(100)$ ,  $\text{Au}(111)$ ,  $\text{Au}(100)$  and highly oriented pyrolytic graphite (HOPG) as well as on the second atomic layer (AL) of Fe on  $\text{W}(110)$ . Depending on the substrate, different cleaning techniques, namely sputtering, cleaving, and high temperature heating, have been applied and will be presented here.

#### IV.3.1. Sputtered Samples

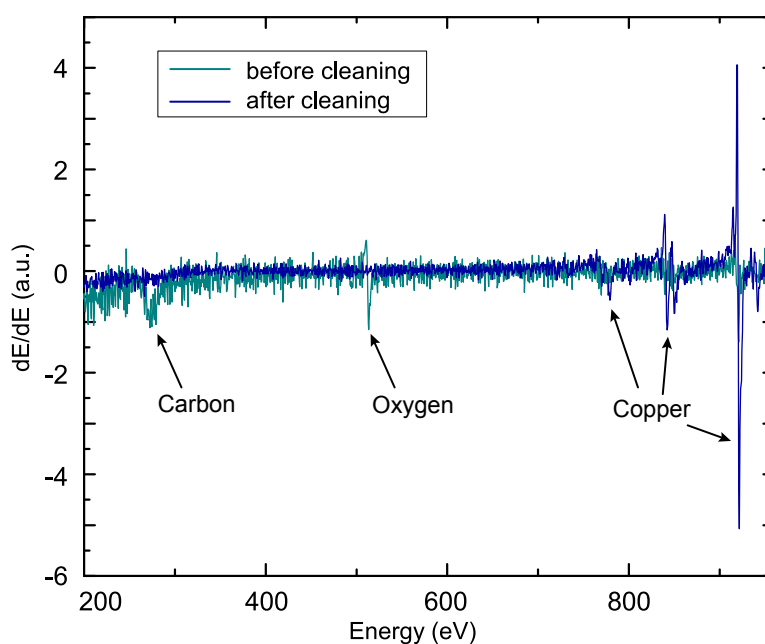


**Figure IV.6:** Auger spectrum of the  $\text{Cu}(100)$  surface before and after the cleaning process. (Derivative shown for better visualization) After the oxygen annealing and high temperature heating, the features corresponding to carbon and oxygen almost completely disappeared, indicating a clean surface.

Most metal surfaces have to be cleaned by ion bombardment with noble gases, because their melting point is lower than the temperature required to remove adsorbates and oxide layers by simply applying heat. Commonly, argon ions are used to remove (sputter) the first layers together with the contaminations. Bombardment with Ar-ions causes structural damage resulting in a rough surface. The surface damage can be cured by slowly

**Table IV.1.:** Sputtering and annealing parameters for the metallic substrates Cu(100), Au(111) and Au(100).

<b>Cu(100)</b>	SPUTTERING	ENERGY	DURATION	
		1.5 kV	15 min	
	ANNEALING	TEMPERATURE	DURATION	COOLING RATE
		760 K	20 min	30 K/min
<b>Au(111)</b>	SPUTTERING	ENERGY	DURATION	
		0.5 kV	20 min	
	ANNEALING	TEMPERATURE	DURATION	COOLING RATE
		900 K	40 min	30 K/min
<b>Au(100)</b>	SPUTTERING	ENERGY	DURATION	
		0.5 kV	20 min	
	ANNEALING	TEMPERATURE	DURATION	COOLING RATE
		900 K	40 min	30 K/min

warming up and cooling down the crystal at proper temperatures. This preparation step is therefore called "annealing". The annealing process can cause contaminations migrating from the bulk to the surface, so that it might be necessary to apply several sputtering and annealing cycles. Figure IV.6 shows representative Auger spectra before and after the cleaning procedure of Cu(100). Carbon and oxygen which are known to be the main contaminating species are absent after the sputtering and annealing process. Auger spectra for the other metal surfaces used in this work show similar improvements and are therefore not shown. Depending on the material to be cleaned different sputtering energies and annealing temperatures are suitable to obtain clean surfaces. In order to gain large surface terraces with the desired crystal structure both annealing duration and cooling rate have to be chosen in an adequate way. Table IV.1 summarizes the sputtering energies and annealing temperatures for the metallic crystals used for the investigations presented in this thesis. For the sputtering of all metallic surfaces the emission current and the partial argon pressure were set to  $I_{\text{Emis}} = 10 \text{ mA}$  and  $p_{\text{par}} = 5 \cdot 10^{-6} \text{ mbar}$ , respectively.

### IV.3.2. HOPG

Due to the layered structure of HOPG, it is possible to obtain very clean surfaces by cleaving the crystal to remove the first few contaminated layers. Therefore scotch tape is glued homogeneously on the flat surface before the sample is transferred into the vacuum. After pumping the load-lock chamber to  $1 \cdot 10^{-5} \text{ mbar}$ , the scotch tape is stripped off. Figure IV.7 shows an STM images, taken after this process. Atomic resolution is achieved exhibiting a clean surface without adsorbates.



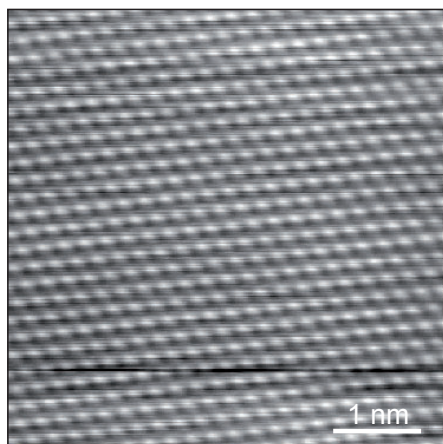


**Figure IV.7:** Atomic resolution STM image of a HOPG surface taken after in-situ cleaving. The image exhibits a clean surface without defects or adsorbates. [ $I_T = 1 \text{ nA}$ ,  $V_{\text{Bias}} = 0.2 \text{ V}$ , z-color scale: black ( $z=0 \text{ pm}$ ) to white ( $z=180 \text{ pm}$ )]

### IV.3.3. Iron on Tungsten

The second atomic layer of Fe on W(110) is used to characterize the suitability of bulk Cr-tips for spin-polarized STM measurements and as a substrate for single molecule studies on NdPc<sub>2</sub>. For the sample preparation a clean tungsten substrate has to be achieved before depositing the iron on top of the surface. The main impurity in the densely packed

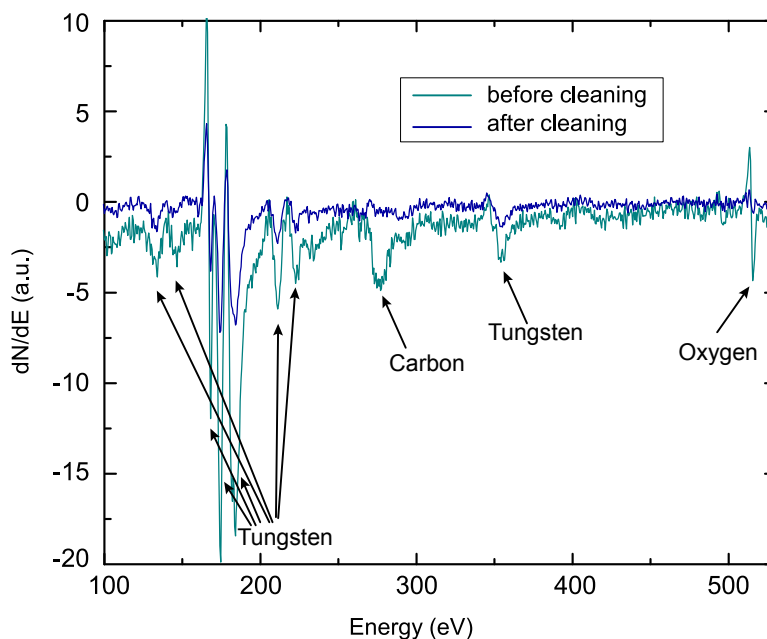


**Figure IV.8:** Auger spectrum of the W(110) surface before and after the cleaning procedure. (Derivative shown for better visualization) After the oxygen annealing and high temperature heating, the features corresponding to carbon and oxygen almost completely disappeared, indicating a clean surface.

W(110) crystal is carbon. It is located both on the surface and in the bulk and has to be removed to obtain clean surfaces for STM investigations [58]. Due to its very high melting point, the tungsten surface is cleaned by high temperature heating. Therefore several annealing cycles under oxygen atmosphere and subsequent high temperature heating are

applied. During annealing under oxygen atmosphere with a  $O_2$  partial pressure of about  $2 \cdot 10^{-9}$  torr at 1800 K for 30 min, the carbon migrates from the bulk to the surface. There, it forms CO and  $CO_2$ , which desorb during the annealing process and are removed from the chamber by the pumping system. In addition, oxidized tungsten is formed on the surface and can only be removed by applying high temperatures above 2300 K. Hence, short flashes at temperatures of 2300 K for 20 s are applied after the oxygen annealing process. This procedure is repeated until the base pressure of the chamber stays below  $1 \cdot 10^{-7}$  mbar during the whole process. This value has been observed to be a sufficient indication for the clean tungsten surface by Auger spectroscopy and STM imaging. Figure IV.8 shows a comparison of the Auger spectra on W(110) before and after the cleaning process. The main contaminations of the tungsten surface, carbon and oxygen, are almost absent after the cleaning procedure.

For the STM studies of the second AL of Fe on W(110) an iron wedge is deposited on the clean substrate. To that effect a moveable shutter is positioned between the evaporator and the crystal and slowly retracted during the evaporation. The evaporation rate was measured by using a quartz balance. After depositing, the iron wedge is annealed for a duration of 7 min at 570 K. During the annealing process iron islands coalesce and agglomerate at the step edges of the crystal.

It is important to note that pressure is the most crucial factor in the preparation of clean atomic layers of Fe on W(110). It was observed that base pressures of the preparation chamber of the order of  $5 \cdot 10^{-11}$  mbar and maximum pressure increases to  $2 \cdot 10^{-10}$  mbar during evaporation of the iron have to be assured in order to obtain ferromagnetic order in the second monolayer. The spin-polarized STM investigations on the second AL of Fe on W(110) are presented in Chapter VII

### IV.4. Molecules

The  $NdPc_2$  molecules are synthesized in-house by Claire Besson in the chemists group of Paul Kögeler. The synthesis is based on the procedure reported by de Cian *et al.* for the lutetium analogue [59]. After several purification steps, the purity of the product is ascertained by infrared (IR) and ultraviolet-visible (UV-vis) spectroscopies.

For the in-situ deposition of the molecules, the evaporator shown in Fig. IV.9 is used.<sup>1</sup> A copper screw with a drilled cavity to hold the crucible is heated up via the attached filament, as shown in Fig. IV.9 (b), when the heat shielding visible in (a) is removed. Temperatures above 900 K are achieved by resistively heating a filament attached to the copper block. This set-up has the advantage to distribute the heat homogeneously around the crucible. For the control of the temperature, a thermocouple is mounted at the copper. The molecules are evaporated from a small glass crucible that is inserted into the cavity of

---

<sup>1</sup>The design of the evaporator has been provided by the group of Christian Kumpf from PGI-3, Forschungszentrum Jülich.



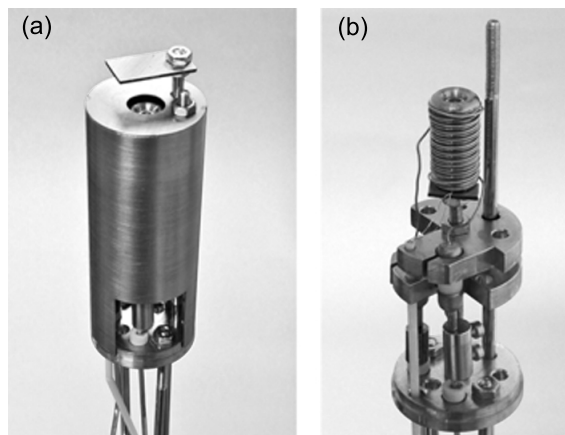


**Figure IV.9:** (a) Evaporator for molecule deposition. (b) After removing the heat shielding, the Cu screw with the drilled cavity and the attached filament is visible.

the copper block. A glass crucible instead of a metallic crucible is chosen for the reason that  $\text{NdPc}_2$  in contact to metals can be chemically altered by electron transfer.

Although the analysis by IR and UV-vis spectroscopy has shown a pure sample from the bulk point of view, contaminations are still present in the pristine molecule powder that might disturb single molecule studies under UHV conditions. Contaminations with evaporation temperatures below the evaporation temperature of the molecules, are easily removed from the powder, by slowly heating up the molecule powder in the vacuum chamber. This so called degassing process takes several days. Once the pressure during the heating process is not decreasing anymore at high constant temperatures close to the evaporation temperature, the degassing process is stopped. As mentioned in Section IV.1, the molecule evaporator is separately pumped and can be separated from the main preparation chamber by a UHV valve. Therefore the pressure in the main chamber is not affected by the degassing procedure. For the evaporation of  $\text{NdPc}_2$  molecules on the different surfaces, the UHV valve is opened. After this, the evaporator is moved towards the sample sitting in the preparation chamber to a distance of approximately 20 cm. The evaporation of  $\text{NdPc}_2$  molecules is observed to be one of the main challenges of this work and therefore will be discussed in the separate Chapter V. Here, it is only mentioned shortly that the amount of double-decker  $\text{NdPc}_2$  molecules on the surface strongly depends on the evaporation temperature, the accumulated evaporation time of the powder inside the crucible and on the substrate involved in the evaporation process.



---

## Adsorption of NdPc<sub>2</sub> on Surfaces

---

The deposition of molecules in ultra high vacuum is in general challenging, since thermal evaporation, which is the method of choice concerning the deposition of metallic substances and can be accomplished with low efforts is not possible in many cases. This applies especially to molecules of bigger size, in which the intramolecular binding energies are low compared to the thermal energy needed to bring it into the gas phase. Therefore, the molecules have to be chosen in a way that thermal evaporation is possible and does not necessarily decompose them. If the molecules of choice are not suitable for thermal evaporation, other deposition methods have to be taken into account. One possibility is an ex-situ deposition of molecules from solution on substrates with low reactivity. Here, a droplet of molecules in solution is deposited on the surface before the sample is transferred into the vacuum system [60]. Another possibility is the deposition of molecules from solution directly into the vacuum, by so called pulsed injection [61,62]. In this case, the liquid is injected into the UHV chamber, by quickly opening and closing a small valve, between the liquid and the UHV-system. After injecting the liquid into the vacuum it evaporates immediately, whereas the molecules stay, in the best case, intact and adsorb on the substrate positioned behind the valve. In contrast to the pulsed injection method, the electrospray injection [63] has the advantage to be a gentle deposition method in which the ionized molecules are decelerated by an applied electric field to ensure a soft landing on the surface. It has also been shown that a method called dry imprint [32] is suitable for in-situ molecule deposition. In the dry imprint technique, molecules attached to an applicator are transferred into the vacuum and afterwards in-situ imprinted from this applicator onto the substrate.

In this work we chose thermal evaporation for the deposition of the early lanthanide NdPc<sub>2</sub> double-decker molecule as it has been described in Chapter IV. For other rare-earth double-decker phthalocyanines, like TbPc<sub>2</sub> [36], DyPc<sub>2</sub> [34], LuPc<sub>2</sub> [64] and YPc<sub>2</sub> [65], it has been already shown that thermal evaporation is possible and intact molecules are found on different surfaces. At higher coverages, it is possible to achieve small two-dimensional islands

of TbPc<sub>2</sub> [34] and YPc<sub>2</sub> [65]. Additionally, it was also observed that during evaporation a notable amount of TbPc<sub>2</sub> double-decker decompose into single-decker molecules that coexist on the Au(111) surface [34]. It is known that early lanthanide complexes like NdPc<sub>2</sub> are less stable compared to the late lanthanide analogues [30]. The main reason for the difference in stability is the size of the central lanthanide ion in the double-decker molecule. It decreases with an increasing number of electrons in the 4*f*-orbital. Therefore, the metal to ligand interaction is stronger in the smaller late lanthanides. As a consequence it is expected that the decomposition of the NdPc<sub>2</sub> in comparison to the late lanthanide complexes is more likely. Nevertheless the larger extend of the ion in the NdPc<sub>2</sub> molecule makes it to a superior candidate compared to late lanthanide double-decker phthalocyanines regarding the direct accessibility of the 4*f*-orbitals as described in the introduction in Chapter II and is for this reason chosen in our study.

Here, it has been observed in the experiments with the NdPc<sub>2</sub> double-decker molecule that indeed one of the main tasks in accordance with the reduced stability, is the evaporation of intact molecules in an appropriate amount onto the surface of choice. Our experiments show further that the fraction of intact molecules strongly depends on the chosen substrate. Surfaces with higher adsorption energies, like Cu(100), tend to stabilize the NdPc<sub>2</sub> molecule, whereas surfaces on which NdPc<sub>2</sub> mainly physisorbs, like Au(111), tend to promote the decomposition into single-decker molecules. This observation is puzzling on first sight, since it would be intuitive to assume that the release of adsorption energy supports the breaking of the weak intramolecular bonds and favors a decomposition of the double-decker molecule. In the following, the experimental results are presented and discussed to find explanations for the results.

## V.1. Surface-Dependent Adsorption

Five different substrates are used for a surface dependent study of the adsorption of the NdPc<sub>2</sub> molecules, namely the second AL of Fe on W(110) (in the following referred to as Fe), Cu(100), Au(111), Au(100) and HOPG. These substrates are prepared as described in Chapter IV and the surface is investigated via scanning tunneling microscopy and spectroscopy after the evaporation step. For the thermal evaporation of the molecules on the substrate, the pristine powder in the crucible is degassed as described in Chapter IV. The evaporator is then heated up to 850 K and kept at this temperature for about half an hour to ensure stable temperature conditions inside the crucible. Afterwards, the valve separating the evaporator and the preparation chamber is opened and the molecules are deposited. The substrates are kept at room temperature. During evaporation, the pressure in the preparation chamber is  $2 \cdot 10^{-9}$  mbar and an evaporation time of 10 s is found to be best, since with longer durations, the amount of surface contaminations increased together with the amount of molecules deposited. Especially during the deposition of molecules on the Fe surface, the relatively bad pressure compared to standard conditions of  $4 \cdot 10^{-11}$  mbar is observed to have a negative influence on the magnetism of the surface as it will be seen later in this Section. Therefore it was necessary to find a compro-

mise between the amount of deposited molecules and the total contamination on the surface.

In the following, the experimental results of the surface dependent adsorption on the five different substrates is presented and discussed. All experiments were carried out under the same ultra high vacuum conditions with the same batch of molecule powder loaded to the crucible of the evaporator. Cu(100) is used as a reference system meaning that after each experiment on one of the other surfaces it was controlled whether the observations on the Cu(100) surface stay the same. In this way it is excluded that changes of the powder are responsible for the different observations for different surfaces. The experiments on the Fe surface are an exception to this. They were done with a different batch of molecule powder, whereas a comparison with the Cu(100) surface was also done during these experiments and thus allowing for a direct comparison of all five substrates.

### V.1.1. Cu(100)

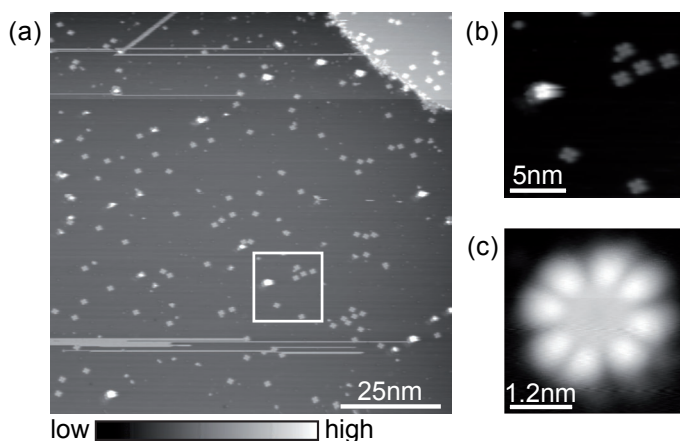
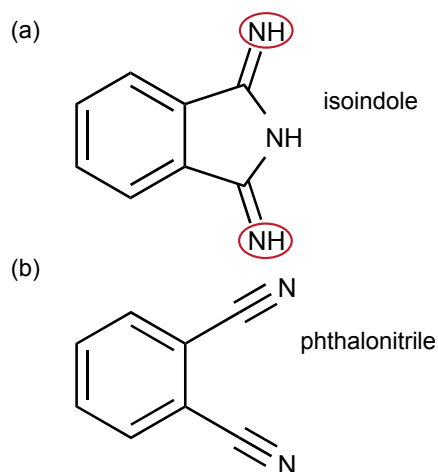


**Figure V.1.:** Constant current STM images of the NdPc<sub>2</sub> molecule deposited on the Cu(100) surfaces. (a) Double-decker molecules along with the decomposed single-decker molecules are observed. The double-decker molecules are identified by their larger height, compared to the clearly four-lobed single-decker molecules. (b) Zoom into the surface in (a) marked by the white square. (c) Zoom into one of the double-decker molecules showing the previously observed eight-lobed structure of the LnPc<sub>2</sub>. Along with the molecules in (a) and (b), adsorbates of smaller sizes are observed. They exhibit a size of a quarter of a single-decker Pc. [(a) – (c)  $V_{\text{bias}} = -1$  V and  $I_T = 1$  nA]

Figure V.1 (a) shows a constant current STM overview image of the Cu(100) surface after the deposition of NdPc<sub>2</sub> molecules as described above. Along with a large amount of single-decker molecules, only a few double-decker molecules are observed. For a better visualization Fig. V.1 (b) shows a zoom into the surface of (a). The two different species are identified by their shape and height. The single-decker phthalocyanines exhibit the well-known four-lobed shape [66] and have a smaller height compared to the double-decker phthalocyanines. The higher double-decker molecules cannot be unambiguously identified in the overview image in (a), but a zoom to one of the molecules shown in Fig. V.1 (c)

reveals the eight-lobe structure of the double-decker phthalocyanine [32]. As described above, it is already known from the deposition of TbPc<sub>2</sub> that the double-decker molecules decompose into single-decker molecules and both species are found on the surface [34]. Therefore it can be concluded that out of ten deposited molecules, only less than two stay intact after adsorption on the Cu(100) surface. In the various experiments of the deposition of NdPc<sub>2</sub> molecules on the Cu(100) surface it has been observed that the total yield of molecules decreases the longer a batch of powder is used. This happens on a time scale of weeks, during which the powder batch was used for twenty to forty different preparation and deposition steps. In the end, the powder batch has to be exchanged by a new load. What is observed inside the crucible, when it is exchanged by a new powder, is not what was expected. The amount of powder left inside remains roughly the same as before sublimation. An investigation by UV-vis spectroscopy revealed that all the double-decker molecules formed triple-decker phthalocyanines under the influence of the applied heat. These chemical changes of the double-decker into triple-decker molecules are very likely, as the low stability of the NdPc<sub>2</sub> molecule tends to favor a formation of Nd<sub>2</sub>Pc<sub>3</sub> molecules [67]. Additional attempts to deposit these leftovers at higher evaporation temperatures were not successful, so that an investigation by STM was not possible. The reason might be the very high temperatures required to sublimate the large triple-decker molecule which could not be reached with the evaporator.

**Figure V.2:** Possible fractions of the phthalocyanine molecule, describing the small additional adsorbates after the deposition of the NdPc<sub>2</sub> molecule: (a) isoindole or (b) phthalonitrile



In addition to the two molecular species, the intact double-decker and the single-decker, another type of adsorbate is observed on the surface. It has a quarter of the size of a single phthalocyanine molecule and it will be shown that it is observed for all substrates after the deposition of molecules. These smaller adsorbates can be identified with another decomposition product of the phthalocyanine. It was explained in Chapter II that the single-decker phthalocyanine molecule consists of four isoindole molecules, shown in Fig. V.2 (a) linked via the marked nitrogens. It is likely that the phthalocyanine complex itself decomposed further during evaporation in either the isoindole or the phthalonitrile molecule sketched in Fig. V.2 (a) and (b) and that these are the additional adsorbates observed on the surfaces,

since they would both fit from size and shape.

### V.1.2. Fe on W(110)

In a next step, the molecules were deposited on Fe. Figure V.3 (a) and (d) show overview constant current STM images of the surface after the deposition of the molecules for two different evaporation times. The data in image (d) is shown again in (e), but modified to enhance the small contrast between the substrate and the molecules. For this purpose the statistical differencing filter was used: here, around each point of the image  $x_i$  a local field is defined for which the arithmetical mean  $\bar{x}$  and the variance  $\Delta x$  is calculated. The new image point is then defined as

$$x_i^{\text{new}} = \frac{x_i - \bar{x}}{\Delta x + \text{weight}}. \quad (\text{V.1})$$

This modification reduces large variations in the z component of the image (e.g. at step edges), but keeps modulations on smaller scales on flat areas. The variance in the denominator smoothes out effects close to large height variations of the image. Its influence can be modified by choosing different *weight* values.

The surface in (a) was exposed to the molecule flux for 5 s, the surface in (d) and (e) for 10 s. The influence of the evaporation time can be observed on the basis of the total amount of molecules adsorbed on the surface, but also by the amount of additional contaminations. For further investigations of the molecule on the Fe surface (see Chapter VIII) it was required that the surface layer keeps its magnetic moment. A large amount of contaminations however quenches the magnetism of the second AL. Already the surface in (d) did not show any magnetic contrast after depositing the molecules, whereas magnetic domains could be observed on the surface in (a) by means of spin-polarized STM. The resulting image is shown in Fig. V.3 (c). Bright and dark areas indicate magnetic domains, in which the magnetization vector points into or out of the surface plane. A detailed analysis of the topographic and magnetic structure of the second AL of Fe on W(110) by means of spin-polarized STM and STS is presented in Chapter VII and will therefore not be further discussed here.

Independently of the evaporation time it is observed that the ratio of intact double-decker to the decomposed molecules is much higher than on Cu(100). The bright spots close to the dislocation lines of the surface in Fig. V.3 (a) (see red circles) can be identified with double-decker NdPc<sub>2</sub> molecule as the zoom in (b) clearly shows. Single-decker phthalocyanine molecules appear less bright and smaller compared to the intact molecules. In Fig. V.3 (e), two NdPc<sub>2</sub> along with four single-decker molecules are identified. One of the NdPc<sub>2</sub> molecules is magnified in Fig. V.3 (f). This yields a decomposition probability of 50 % for this small section of the surface, but is confirmed by additional images on other surface regions which are not shown. Again, the additional smaller decomposition products which we identified with either the isoindole or the phthalonitrile molecule, are observed on the surface.

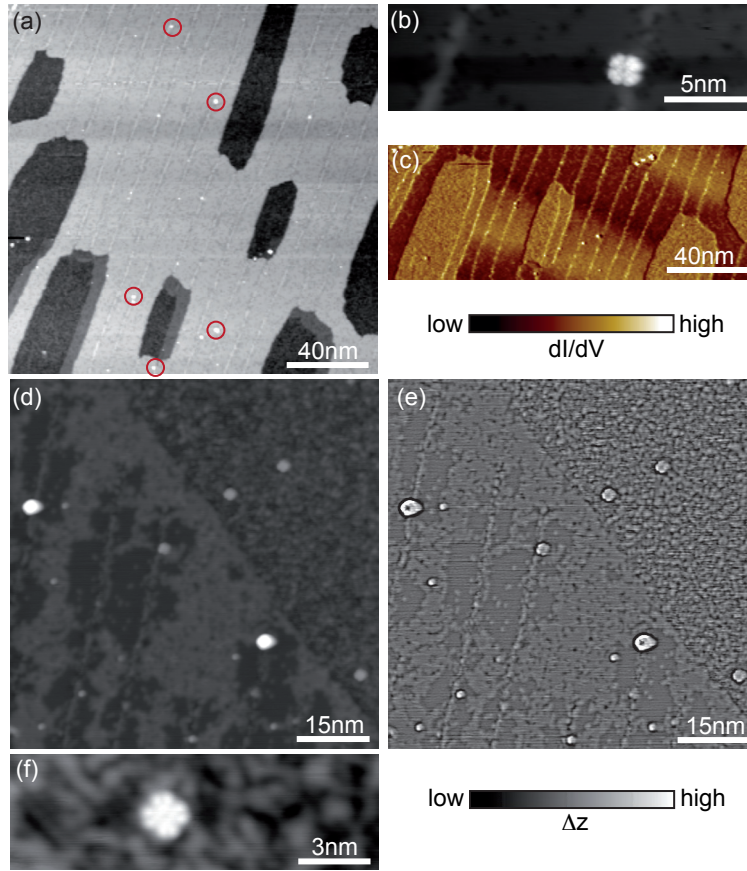


**Figure V.3.:** (a), (d) Constant current STM images of the NdPc<sub>2</sub> molecules deposited on the second AL of Fe on W(110). NdPc<sub>2</sub> along with single-decker molecules can be observed, but the ratio of intact to decomposed molecules is larger than on the Cu(100) surface shown in Fig. V.1. The double-decker molecules are predominantly located at the dislocation lines of the second AL (see red circles). (e) shows the surface of (d), but the contrast is enhanced by the statistical differencing filter. (b), (f) Zooms of NdPc<sub>2</sub> molecules. Due to a lower contamination rate, magnetic contrast is observed on the surface in (a) as shown in the spin-polarized  $dI/dV$ -map in (c) and was not present for the surface shown in (d). [(a) – (e)  $I_T = 1$  nA and (a)  $V_{\text{bias}} = -0.3$  V, (b)  $V_{\text{bias}} = -1.3$  V, (c)  $V_{\text{bias}} = -0.3$  V  $f_{\text{mod}} = 2.7$  kHz,  $V_{\text{mod}} = 30$  meV rms, (d) and (e)  $V_{\text{bias}} = 1$  V]

### V.1.3. Au(111)

The results of the deposition of NdPc<sub>2</sub> on the Au(111) surface differ severely from the already presented observations on Cu(100) and Fe. In the surface overview image in Fig. V.4 (a) only single-decker molecules are found which means that the NdPc<sub>2</sub> molecule decomposes to 100%. Together with the single-decker molecules the typical smaller adsorbates are also observed again. In the background, the distorted herringbone reconstruction of the Au(111) surface is present. Most of the molecules are located in between the herringbone lines and appear with the same brightness. Those molecules located on top of the reconstruction lines



appear brighter and exhibit a tail into the scan direction (see red circles in Fig. V.4 (a)). A closer investigation of the step edges of the crystal in Fig. V.4 (b) exhibits phthalocyanine molecules arranged along the edges. These molecules appear with one or two of the four benzene-like lobes attached to the higher level of the crystal and the other two or three at the lower one. The favored configuration seems to depend on the nature of the step edge, since molecules at one particular edge are almost exclusively attached in the same way. This correlation was not further investigated. Another important result of the adsorbed molecules on the Au(111) surface can also be seen in this image. The phthalocyanines on the flat part of the surface are moved during the scan along the surface due to the influence of the STM tip. This indicates a rather weak coupling of the phthalocyanine to the Au(111) surface that will be discussed in detail later in this Section. An additional observation on the adsorbed phthalocyanine molecules is made by further zooming into the surface as shown in Fig. V.4 (c) and (d).

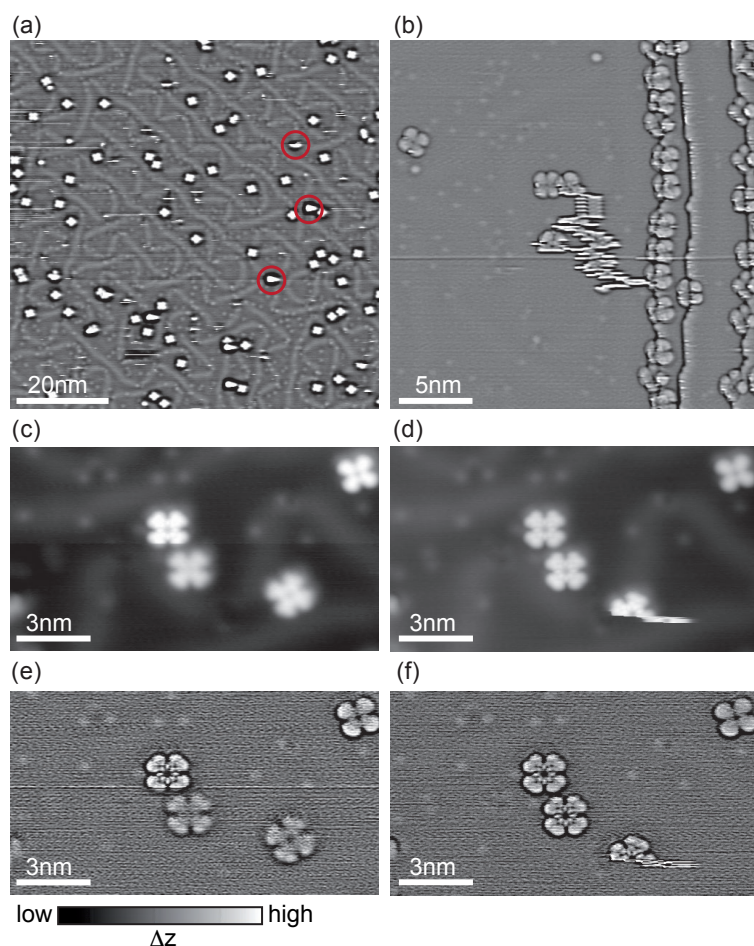


**Figure V.4:** (a) Overview image of the NdPc<sub>2</sub> molecules deposited on the Au(111) surface. The surface reconstruction of the substrate is visible and only decomposed single-decker molecules are observed. (b) Single-decker molecules are located at the step edges of the surface and molecules can be moved along the surface during the scan. The images in (a) and (b) are modified by the statistical differencing filter. (c) Molecules appear in STM images either in a four lobed structure either with only a dip or a protrusion in the center or with additional eight protrusions around a dip. During scanning the appearance of the molecule can change as shown in (c)–(f), but the change is not reversible. (e) and (f) show the data of (c) and (d) after applying the statistical differencing filter. [(a) – (f)  $I_T = 1$  nA and  $V_{\text{bias}} = -1$  V]

First it should be discussed what happens with the Nd ion, when the double-decker molecule decomposes. It is very likely that the ion stays attached to one of the two single

phthalocyanines. A possibility to distinguish between the two species could for instance be a difference of the height in the center of the molecule. In case of a protrusion a Nd atom is assumed to be present, in case of dip, it would be absent. Attention has to be paid by drawing this conclusion, as it was shown [68] that the presence of a central atom in a single Pc cannot unambiguously be identified by the height of the center in an STM image. Depending on the species of the central atom it can possibly be located between the single Pc and the surface and therefore not be visible in an STM topography experiment at all [68]. For final conclusions, it would be necessary to investigate the electronic structure of the molecule by STS to obtain evidence for a clear identification of the central atomic species. However, this investigation was not made in this work. Nevertheless, the observations in Fig. V.4 (c) to (f) might give a hint on the presence of a Nd ion, since the phthalocyanines in these images appear with different features in the center. For a better visualization of the intramolecular features, Fig. V.4 (e) and (f) show the constant current images of (c) and (d) after applying the statistical differencing filter. As described in the introduction to scanning tunneling microscopy in Chapter III the constant current images reflect the integrated electronic structure of the surface. In Fig. V.4 (c) and (e) three of the molecules appear in the typical four-lobed symmetry with either a darker center or an apparent protrusion. One of the molecules exhibits additional eight small protrusions around the center which can be identified with the eight nitrogen atoms of the phthalocyanine. A tip modification happened during this scan allowing for a higher resolution of the central part of the molecule. After a subsequent scan along the surface shown in Fig. V.4 (d) and (f), two additional molecules change their appearance due to the better resolution of the tip apex. One molecule sticks to the tip and is moved to a different position on the surface. The fourth molecule in the upper right corner of the images does not exhibit additional features around the center. This clear difference between the two molecular species in the constant current STM image indicates a difference in the electronic structure. Possibly, for one molecular species the Nd ion is attached to the center, whereas the other molecular species is Nd free. The two broken bonds to the former central ion are then satisfied by for example surface atoms or by the attachment of two hydrogen atoms from the residual gas resulting in a different appearance in the constant current images. Of course, other explanations for the different appearances are also possible. Maybe differences in the adsorption position of the molecule induce these changes in the electronic structure and therefore in the appearance.

#### V.1.4. Au(100)

On the Au(100) surface the result differs again strongly. The surface shown in the constant current STM image in Fig. V.5 exhibits the well-known  $5 \times 1$  surface reconstruction [69], but no double-decker or single-decker molecules are observed on the surface. The distance between two rows of the reconstruction is approximately 1 nm and thus smaller than the width of a double-decker NdPc<sub>2</sub> molecule with 2.7 nm or a single-decker phthalocyanine with 2 nm. Nevertheless, the smaller fractions isoindole and phthalonitrile of the phthalocyanine

already located on the other surfaces can be observed again. They are smaller than one nanometer and therefore fit between the rows of the surface reconstruction. These adsorbates are identified along the step edges in Fig. V.5 (c) and we claim that the adsorbates on the surface in Fig. V.5 (a) are of the same type. A stable imaging of the Au(100) surface is not possible, due to the large amount of small adsorbates that are moved along the surface during the scan, but it is observed that after several scans the surface becomes cleaner and the adsorbates are most likely moved to surface areas outside the imaged range as shown in Fig. V.5 (b) which was taken after three scans of the same surface region.

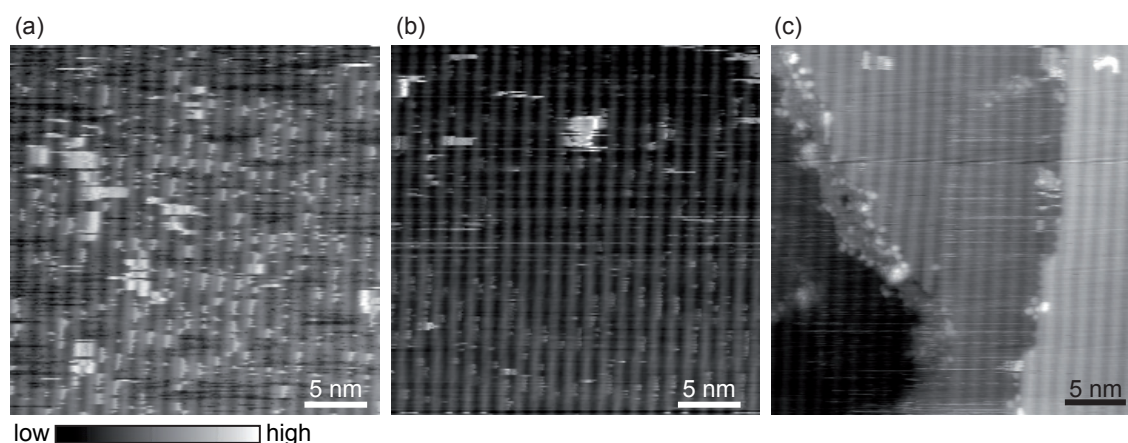


**Figure V.5.:** (a) Overview image of the Au(100) surface after evaporation of the NdPc<sub>2</sub> molecules. The  $5 \times 1$  surface reconstruction of the substrate is visible and no molecules are observed. Smaller adsorbates sit at the step edges and on the surface and prohibit stable tunneling. (b) After three times scanning along the same surface region, less adsorbates are observed and the tunneling is more stable as compared to (a). (c) Adsorbates associated to isoindole or phthalonitrile molecules, are located at the step edges of the crystal. [(a), (b)  $V_{\text{bias}} = 1 \text{ V}$  and  $I_{\text{T}} = 0.5 \text{ nA}$  and (c)  $V_{\text{bias}} = -1 \text{ V}$  and  $I_{\text{T}} = 0.5 \text{ nA}$ ]

### V.1.5. HOPG

The experiments on the HOPG substrate showed a clean surface with atomic resolution as shown in the preparation Section in Chapter IV. Even after repeated deposition steps for up to 30 s evaporation time, no adsorbates could be observed on the clean surface, except for some adsorbates at the step edges that could not be identified with any of the molecular species seen before on the other substrates.

## V.2. Discussion

In summary, the results of the thermal deposition of NdPc<sub>2</sub> molecules depend strongly on the used substrate. Fe tends to stabilize the molecule in comparison to Cu(100), on which more than 80 % of the double-decker decompose into single-decker. The Au(111) surface

solely exhibits single-decker phthalocyanines and on Au(100) and HOPG non of these two molecular species can be identified.

Several different mechanisms have to be considered to play a role in the decomposition or stabilization of the molecular structure of NdPc<sub>2</sub> during the evaporation and the adsorption on the surface. In the beginning of the process, the molecule powder is heated up. The thermal energy alters the chemical structure of the molecule inside the crucible and triple-decker molecules are formed. Therefore, it is possible that already in this state of the process decomposed fractions of the molecules leave the crucible, such as single phthalocyanines and the smaller fractions like isoindole. Since we observed a surface dependent decomposition in our experiments this thermally induced effect is not dominant, but can not be fully neglected. In addition to the thermal energy during the evaporation there is a contribution of the kinetic energy of the molecule which is released when it hits the substrate and also contributes to the decomposition of the molecular structure. Another contribution that tends to favor a breakup of the weak intramolecular bonds is the release of adsorption energy. This contribution is strongly surface dependent and would lead to the observation that on surfaces with higher binding energies, less intact molecules are found. The exact value of the binding energy depends on both the surface and the adsorbate, and has to be calculated with suitable theoretical approaches like density functional theory. This has not been done in this work, but it is possible to compare our adsorbed systems with systems comprising similar molecular structures. Benzene is widely used as a model system for  $\pi$ -conjugated molecules, such as phthalocyanine molecules adsorbed on metal surfaces, and adsorption energies can be given for the different surfaces used in this work. An increase of adsorption energy is calculated starting with benzene on Au(111) with  $E_{\text{ads}} = -0.55$  eV [70] over Cu(100) with  $E_{\text{ads}} = -0.68$  eV [71] up to Fe with  $E_{\text{ads}} = -0.98$  eV [72]. The observation in this Chapter are in contradiction to the trend of the adsorption energy for the investigated surface-molecule systems. In consequence, there have to be other contributions to the stability of the NdPc<sub>2</sub> molecule that compete with the increase of released adsorption energy and stabilize the molecule on surfaces with higher reactivity. As it has been discussed in Chapter II, it is distinguished between chemical and physical adsorption. The physisorption is governed by van-der-Waals interaction that influences the electronic structure of adsorbate and adsorbent only weakly. Binding energies less than  $-0.5$  eV are considered to still be of physisorbed character, whereas stronger binding energies result from chemisorbed systems which can alter the electronic structure of the bonded species drastically. Since it is observed that on the Au(111) surface on which NdPc<sub>2</sub> is considered to be physisorbed, all NdPc<sub>2</sub> molecules decompose, it can be concluded that the character and strength of the bond formation is the counteracting mechanism that tends to stabilize the intramolecular bonds. This conclusion is in accordance with the higher stability of the NdPc<sub>2</sub> molecule on Fe compared to Cu(100), since the total bonding strength is weaker on the latter. Cu is a metal with full  $d$ -orbitals, so that the reactivity of the surface is in general lower compared to other transition metals like Fe [71]. If a molecule forms covalent bonds on a surface, different contributions play a role. Depending on the geometric and energetic positions of the orbitals of the surface

and the molecule with respect to each other, the strength of hybridization and charge transfer differ strongly. Larger overlap of the orbitals however leads to a larger splitting of bonding and anti-bonding states of the hybrid system of the surface and the molecule. As a consequence of the formation of these bonding and anti-bonding states, the occupied and unoccupied frontier orbitals of the molecule shift to higher absolute values and the molecule itself is stabilized. This can be observed by a comparison of scanning tunneling spectroscopy measurements on the  $\text{NdPc}_2$  molecule adsorbed on  $\text{Cu}(100)$  and  $\text{Fe}$  shown in Fig. V.6. The molecule adsorbed on  $\text{Fe}$  which is the surface with higher adsorption energy and stronger chemical binding, exhibits a larger gap between the occupied and unoccupied frontier orbitals as compared to the molecule adsorbed on  $\text{Cu}(100)$ . Therefore its molecular structure should be more stable on  $\text{Fe}$  and in agreement with the experimental observation a larger amount of intact molecules compared to the decomposed species should be present on this surface.

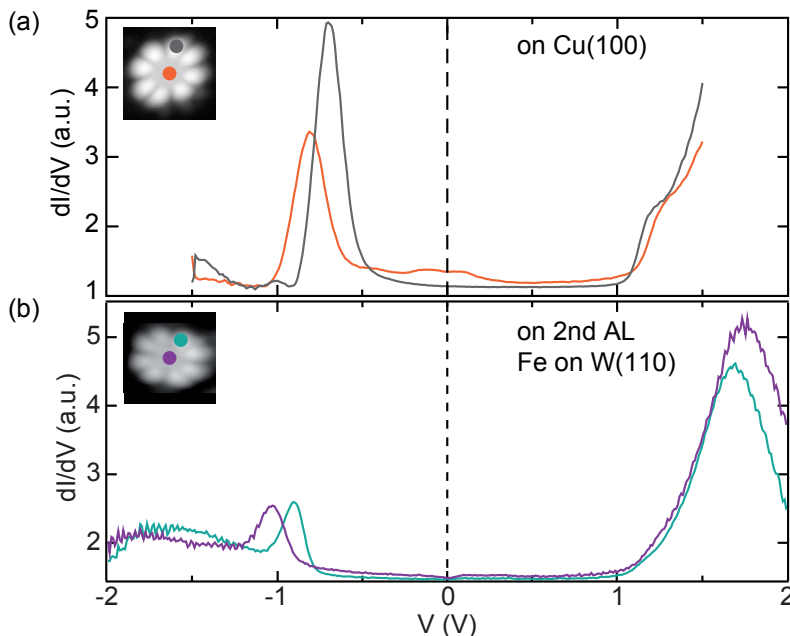


**Figure V.6:**  $dI/dV$ -spectra obtained above the center and the organic ligand of the  $\text{NdPc}_2$  molecule adsorbed on (a)  $\text{Cu}(100)$  and (b)  $\text{Fe}$  on  $\text{W}(110)$ . [ $f_{\text{mod}} = 2.7$  kHz,  $V_{\text{mod}} = 30$  meV rms; (a) tip stabilized at  $I_{\text{T}} = 1$  nA and  $V_{\text{bias}} = -1$  V and (b) tip stabilized at  $I_{\text{T}} = 2$  nA and  $V_{\text{bias}} = 2$  V]

As already mentioned, another mechanism that might occur during chemisorption, is the full or partial transfer of electrons from one bonding partner to the other similar to what is described in Chapter II about polar covalent bond formation. It has been shown that for metallic surfaces and phthalocyanine molecules, charge is transferred from the surface into the molecule [20], but is not possible to estimate the value of the electron transfer without calculations. Nonetheless, the value of the work function of the metallic surface can give an indication. These values are for  $\text{Cu}(100)$  and  $\text{Fe}$  comparable to each other with  $\phi_{\text{Cu}} = 4.59$  eV and  $\phi_{\text{Fe}} = 4.6 - 4.8$  eV [73]. In any case, the transfer of negative charge from the surface to the molecule additionally alters the intramolecular bonds in a stabilizing way. It is described in Chapter II that the intramolecular bonds of the  $\text{NdPc}_2$  molecule is mainly of electrostatical character between the positively

charged Nd<sup>3+</sup> ion in the center and the negatively charged phthalocyanine ligands. A transfer of additional negative charge leads to a higher negative charge on the ligands, so that the total electrostatic energy will increase and the molecule is additionally stabilized.

The result on Au(100) has not necessarily its origin in the adsorption energy contribution but can be explained by taking into account the surface reconstruction. The reconstruction lines are approximately one nanometer apart. Let us consider intact NdPc<sub>2</sub>, decomposed single phthalocyanines and fractions of the phthalocyanine as possible adsorbates on the surface. As a consequence of the short distances of the reconstruction lines, double-decker or single-decker phthalocyanine will not find compatible adsorption sites on the surface and migrate along the surface to the edges of the sample. In contrast to this and in accordance with our observations, the fractions of the phthalocyanine molecule with sizes below one nanometer fit in between the reconstruction and can be observed on the surface. Due to the weak adsorption, they can be moved along the surface by the STM tip similar to the results of the single phthalocyanine molecules on the Au(111) surface (Fig. V.4). Therefore, after several scans along the same surface region less adsorbates are observed.

For the inert surface HOPG no molecules could be located on the surface. We propose that this observation results from the very weak physisorption of the molecules on this surface. The molecules migrate to the edges of the sample or are moved along the surface by the influence of the STM tip and are therefore not detectable. However, in contrast to our observation, Walzer and Hietschold [74] were able to image sub-monolayer coverages of SnPc molecules on HOPG at 62 K by STM. Considering these results, an additional effect of the NdPc<sub>2</sub> molecule itself on the adsorption has to be taken into account for an explanation. This additional effect is not evident, since the deposition on Au(111) has shown that a decomposition of NdPc<sub>2</sub> into single phthalocyanines occurs on surfaces with lower binding energy and these single phthalocyanines should then behave similar to the SnPc in [74]. It is possible that the enhanced surface mobility results from a combination of the kinetic energy of the approaching NdPc<sub>2</sub> together with an energy gain caused by the decomposition of the molecule during adsorption on the surface.

For a more comprehensive investigation, it would be very interesting to study the influence of the substrate temperature during the evaporation on the adsorption. First attempts of molecule deposition at cryogenic substrate temperatures on the Cu(100) surface did not lead to any further conclusion, since no significant change in the adsorption ratio of double-decker to single-decker phthalocyanines could be observed. Nevertheless, a more detailed investigation including also the other substrates might lead to additional observations helpful for the interpretation of the results in this chapter. Including also other lanthanide double-decker phthalocyanines like TbPc<sub>2</sub> or the later analogue LuPc<sub>2</sub> with an even smaller ionic radius of the central atom into the substrate dependent study, might additionally help understanding the correlation between the ionic radius, the resulting intramolecular bonding strength and the adsorption characteristics on the various substrates.

---

## NdPc<sub>2</sub> Spin-Polarized 4*f*-States Accessed by STM

---

In this Chapter the results of the combined experimental STM and theoretical DFT study of NdPc<sub>2</sub> double-decker molecules adsorbed on the Cu(100) surface are discussed. It starts with the presentation of the topographic images obtained by STM concerning the adsorption sites and the overall shape of the molecules on the surface. The main part of the Chapter contains the comparison of the spectroscopic data, both  $dI/dV$  curves and maps, with the *ab initio* DFT calculations, leading towards an unambiguous identification of the observed features. In the end the results are discussed and potential applications as well as possible additional investigation are presented.

### VI.1. Adsorption of NdPc<sub>2</sub> on Cu(100)

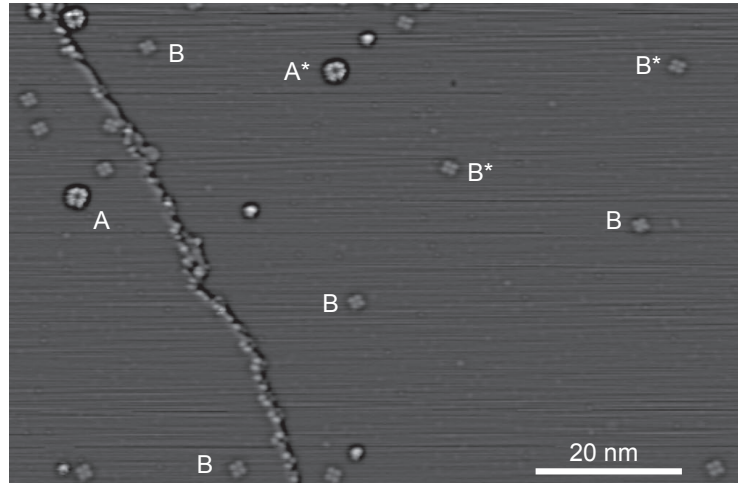
For the STM studies of single NdPc<sub>2</sub> molecules on the Cu(100) surface, the crystal was prepared as described in Section IV.3. After the cleaning procedure single molecules were deposited at evaporation temperatures of 800 K for a duration of 5 s and the sample was immediately transferred into the STM. All the measurements shown in this Chapter were done at cryogenic helium temperatures of 5 K. It has been observed that higher temperatures are not well suited for studies of NdPc<sub>2</sub> on the Cu(100) surface due to the larger drift thermal in the experiment.

Figure VI.1 shows a constant current scanning tunneling microscopy overview image of NdPc<sub>2</sub> molecules adsorbed on the Cu(100) surface. As already discussed in Chapter V double-decker molecules along with single-decker Pc molecules with or without Nd atom in the center can be identified by shape and height. Whether there is a Nd atom left in the center of the single Pc molecule was not investigated.

All three molecular species – Pc, NdPc and NdPc<sub>2</sub> – shown in the image in Fig. VI.1 adsorb in two orientations on the Cu(100) surface. They are labeled with A(B) and A\*(B\*), respec-



**Figure VI.1:** Overview image of the Cu(100) surface. Three molecular species are observed: NdPc<sub>2</sub> (A,A\*) and single-decker Pc (B,B\*) with or without Nd in the center. A(B) and A\*(B\*) mark the different degenerate adsorption sites of the molecules. For better visualization, the image is modified by the statistical differencing filter (see Chapter V). ( $V_{\text{bias}} = 1 \text{ V}$ ,  $I_{\text{T}} = 1 \text{ nA}$ )



tively. In Fig. VI.2(a) two single-decker Pc in the two adsorption configurations B and B\* are shown. For an identification of the main crystal axis, the atomic resolution STM image with arrows indicating the directions is displayed in the inset. The single-decker Pc appears as a four-lobed structure with four-fold symmetry in the STM topography. This has already been observed for different phthalocyanines on a variety of metal surfaces [21, 27, 75, 76]. The sketch in Fig. VI.2(b) shows the two adsorption configurations on the Cu(100) surface

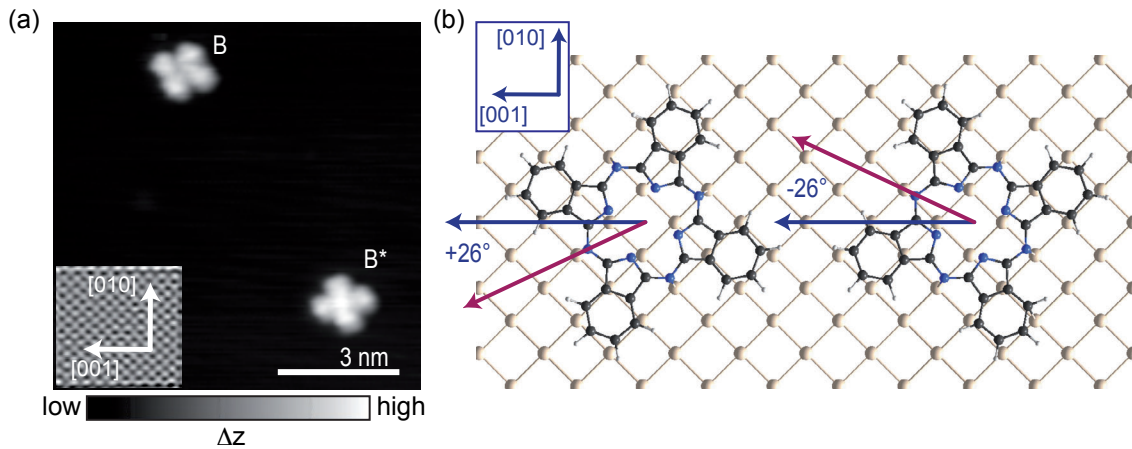


**Figure VI.2.:** (a) Constant current STM image of the two adsorption sites of single-decker Pc B and B\*. (b) Atomic representation of the two adsorption sites. The two configurations are rotated by an angle of  $\pm 26^\circ$  with respect to the [001] - surface direction. ( $V_{\text{bias}} = -1 \text{ V}$ ,  $I_{\text{T}} = 1 \text{ nA}$ )

in an atomic representation. It can be concluded that the two configurations are equivalent and rotated by  $\pm 26^\circ$  with respect to the [001]-direction, respectively as it was already demonstrated by Lippel *et al.* in 1989 for CuPc molecules adsorbed on the Cu(100) surface [66]. In both configurations the overlap between the copper surface atoms and the nitrogen atoms of the Pc ring is highest, which in the calculations turned out to give rise



to the strongest possible bonding (see calculated adsorption site in Fig. VI.4). Analog to the rotation of the single-decker Pc, it is possible to identify the adsorption configurations A and A\* of the double-decker Pc shown in Fig. VI.3(a) and (b).

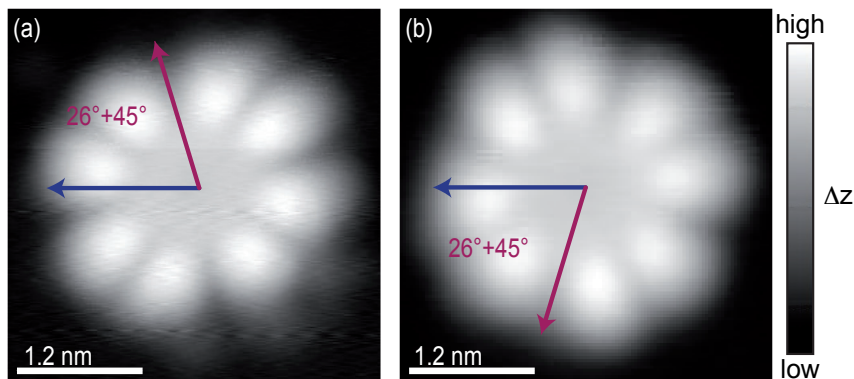


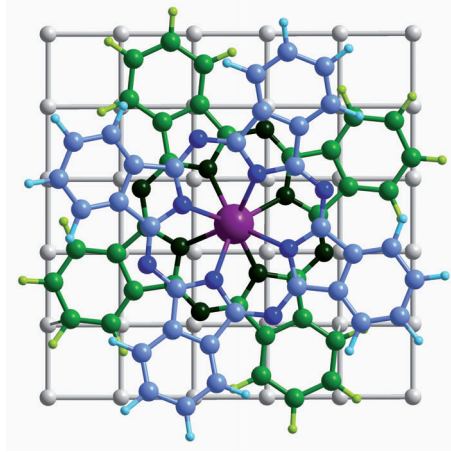
**Figure VI.3.:** Constant current STM images of the two adsorption configurations (a) A\* and (b) A of NdPc<sub>2</sub> molecules adsorbed on Cu(100). The adsorption is governed by the lower Pc ring and analog to the adsorption geometry shown in Fig. VI.2. Upper and lower Pc ring are twisted by an angle of 45° with respect to each other, so that the total rotation angle between the upper Pc and the [001]-surface direction (blue arrow) is  $\pm(26^\circ + 45^\circ) = \pm 71^\circ$ . [(a),(b):  $V_{\text{bias}} = -1 \text{ V}$ ,  $I_T = 1 \text{ nA}$ ]

The NdPc<sub>2</sub> molecule appears in the STM topography images as an eight-lobe shape with a four-fold symmetry as previously observed for other lanthanide double-decker species [32,34,64]. The STM image mainly reflects the charge distribution of the upper Pc ring: Each two-lobe feature is attributed to one benzene-like ring [32] and is also observed in STM images of single phthalocyanine molecules on surfaces covered with thin insulating layers like NaCl [77]. The similarity to STM images of single-decker Pc on insulating surfaces, indicates that for NdPc<sub>2</sub> molecule adsorbed on Cu(100) the molecular electronic features of the upper Pc ring are not significantly modified upon adsorption. The molecules in the two adsorption configurations are rotated by an angle of 71° with respect to the [001]-direction of the Cu(100) crystal surface. As described in Chapter II, the NdPc<sub>2</sub> molecule is mainly electrostatically bound. Therefore the two negatively charged phthalocyanine rings align with an angle of 45° with respect to each other due to the repulsive forces. In conclusion, the adsorption of the NdPc<sub>2</sub> molecule is governed by the lower Pc ring, which adsorbs in the same two equivalent positions on Cu(100) as the single-decker Pc.

For a comprehensive study of the NdPc<sub>2</sub> molecule adsorbed on Cu(100), spin-polarized first-principles total-energy calculations have been carried out in the framework of the density functional theory (DFT) [78] by our colleagues Nicolae Atodiresei and Vasile Caciuc from the Peter Grünberg Institute (PGI-1). To account properly for the orbital dependence of the Coulomb and exchange interactions of the Nd 4*f*-states they employed the PBE+*U* method [79]. The Hubbard parameter for the *f*-states was set to  $U = 2.2 \text{ eV}$  to reproduce the experimental  $dI/dV$  features as it will be described later in this Chapter

again. The NdPc<sub>2</sub>-Cu(100) system was modeled within the supercell approach and contains five atomic Cu layers with the adsorbed molecule on one side of the slab. Additionally, van der Waals interaction was included into the calculations as it was shown to be from significance for  $\pi$ -conjugated systems before [19].

**Figure VI.4:** Calculated adsorption geometry of the NdPc<sub>2</sub> double-decker molecule on the Cu(100) surface. The hollow position of the central atom, as shown here, is the energetically favorable one. Atomic representation: hydrogen (light green, light blue), carbon (green, blue), nitrogen (dark green, dark blue) and neodymium (magenta)



The *ab initio* calculations show that the adsorption geometry with the central Nd ion above the hollow site of the Cu(100) surface, sketched in Fig. VI.4, is energetically most favorable. In the following we mainly focus on NdPc<sub>2</sub> molecules in the adsorption configuration A\* shown in Fig. VI.3(a), since both experiment and calculations confirm that the two configurations are equivalent by the symmetry of the Cu lattice and exhibit the same electronic features.

Constant current STM topography images of the adsorbed molecule were recorded for different bias voltages as shown in Fig. VI.5(a)-(d). Varying the bias voltage slightly changes the shape of the molecule. However, the main features of the images are similar in all cases. The central part exhibits lower z-signal compared to the surrounding eight protrusions of the ligands, only the shape of the eight protrusions and the exact geometry of the center changes with energy. These images can be compared to the calculated topography pictures representing the integrated projected charge density for the corresponding bias voltages. As described in Chapter III, the z-piezo signal in constant current STM images reflects surfaces of constant density of states of the sample, which means the topography image reflects isosurfaces of the density of states. The integrated projected charge density is calculated for every space point leading to a volume data set from which the topography is extracted. To generate the theoretical images, the z-values corresponding to the isosurface are extracted from the volume data set of the integrated projected charge density and plotted. The resulting calculated topography pictures of the molecule are plotted in Fig. VI.5(e)-(h). For each corresponding experimentally obtained and calculated image, the overall shape is reproduced. This excellent agreement regarding the topography of the molecule is the basis for further comparison and interpretation of the experimentally observed electronic structure of NdPc<sub>2</sub> on Cu(100) with the first-principles calculations.

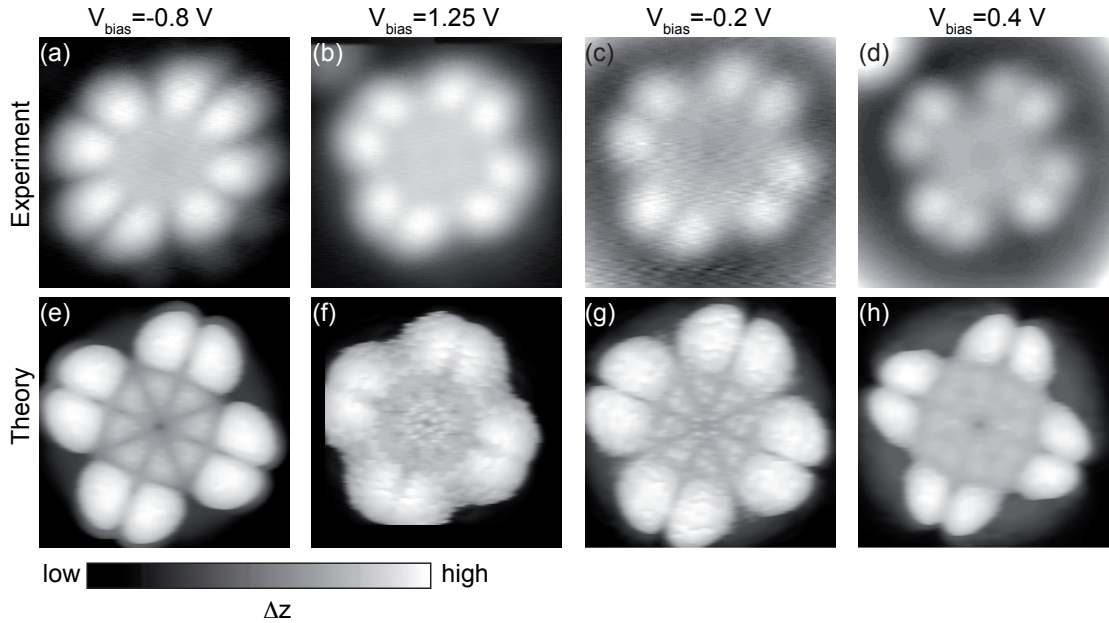


**Figure VI.5.:** Constant current STM images of the NdPc<sub>2</sub> molecules adsorbed on Cu(100) measured at different bias voltages and  $I_T = 1$  nA tunneling current: (a)  $V_{\text{bias}} = -0.8$  V, (b)  $V_{\text{bias}} = 1.25$  V, (c)  $V_{\text{bias}} = -0.2$  V, (d)  $V_{\text{bias}} = 0.4$  V and (e)-(h) the corresponding calculated topography images. Experimental and calculated images are in excellent agreement. Color code is individually scaled. (Image sizes:  $2.7 \times 2.7$  nm<sup>2</sup>)

## VI.2. Electronic Structure of the Adsorbed NdPc<sub>2</sub>

In addition to the information about the topography of the molecule presented in the last Section,  $dI/dV$  curves were measured, as described in Chapter III, to gain insight into the electronic structure the NdPc<sub>2</sub> molecule adsorbed on Cu(100). The  $dI/dV$  spectroscopy measurements were performed at specific positions of the STM tip above the NdPc<sub>2</sub> molecule. Fig. VI.6(a) shows the two spectra obtained on the center (orange curve) and above the organic ligand (grey curve) site of the molecule.

According to the explanations in Chapter III, negative bias voltages represent occupied and positive bias voltages unoccupied states of the surface or rather molecule. Two clear features close to the Fermi energy are observed in both spectra: one distinct peak on the occupied side of the Fermi energy and a shoulder in the rising edge of the unoccupied states. For comparison, the spin-polarized first-principles calculations for the adsorbed NdPc<sub>2</sub> on Cu(100) are shown in Fig. VI.6(b). The projected density of states (PDOS) is calculated for the upper Pc ring (blue curve), the Nd 4*f*-states (magenta curve) and the lower Pc ring (green curve). The lower Pc ring shows broad hybrid molecule-surface electronic states identified by the broad structures of the calculated PDOS. The molecular-type features, present in the free molecule, vanish due to hybridization [21] and charge transfer with the surface. In the free molecule, the ligands carry a spin moment originating from one

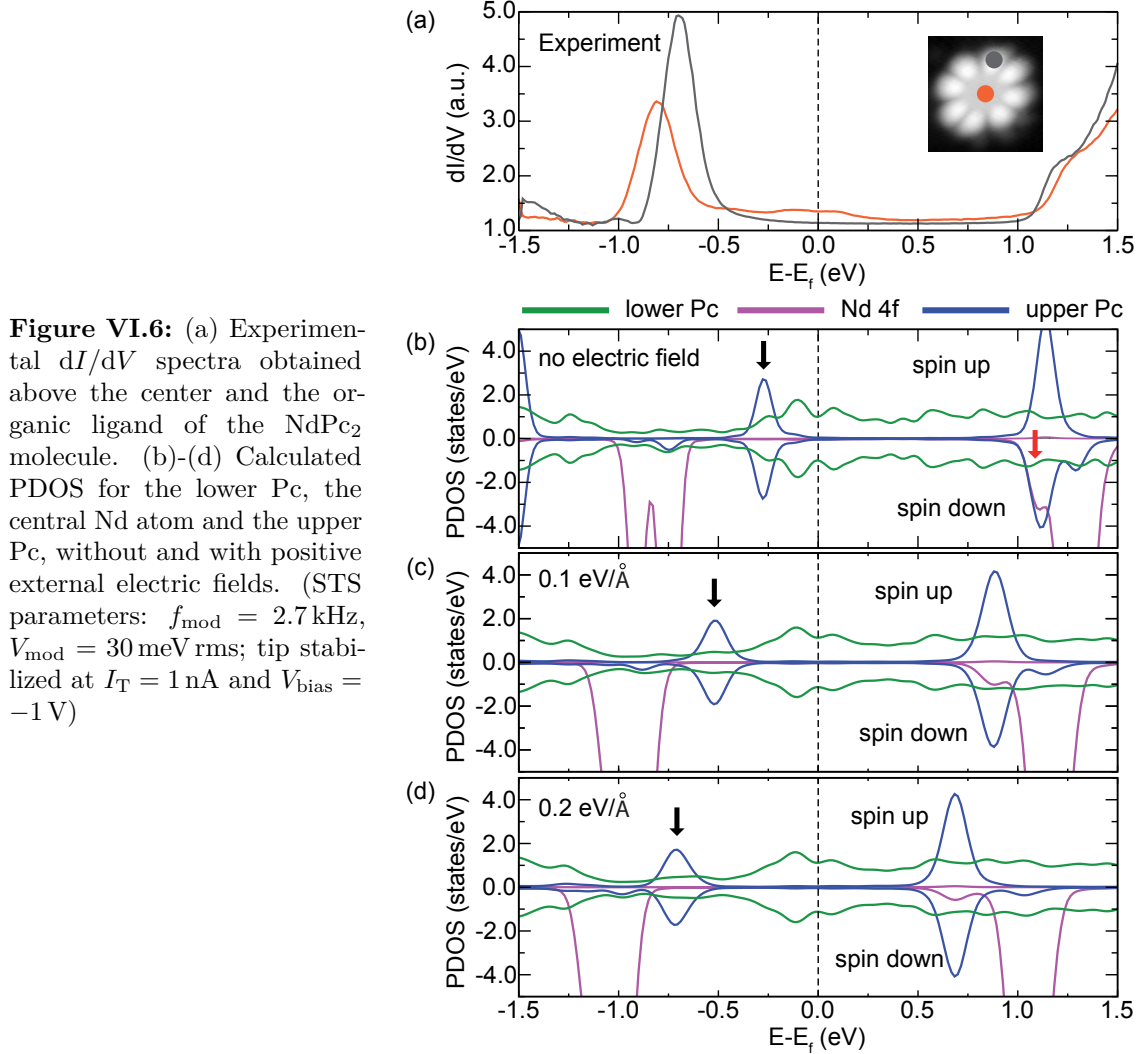


**Figure VI.6:** (a) Experimental  $dI/dV$  spectra obtained above the center and the organic ligand of the NdPc<sub>2</sub> molecule. (b)-(d) Calculated PDOS for the lower Pc, the central Nd atom and the upper Pc, without and with positive external electric fields. (STS parameters:  $f_{\text{mod}} = 2.7 \text{ kHz}$ ,  $V_{\text{mod}} = 30 \text{ meV rms}$ ; tip stabilized at  $I_T = 1 \text{ nA}$  and  $V_{\text{bias}} = -1 \text{ V}$ )

unpaired spin. As a result of the hybridization and charge transfer the spin moment and hence, the magnetic moment on the ligands, vanishes. The PDOS of the upper Pc ring keeps sharp molecular-like features similar to those obtained for NdPc<sub>2</sub> in the gas phase [32]. This characteristic of the upper Pc ring was already discussed in the last Section, since it is also visible in the topography STM images. These images resemble the shape of the molecular orbitals of the upper Pc ring as they are expected for the free single-decker Pc. The striking difference between the electronic states of the upper and the lower Pc ring suggests that the two Pc rings are only coupled via a weak hybridization with the 4*f*-states through the Nd atom in the center. These findings represent the unique characteristic of the double-decker Pc molecule. It chemisorbs strongly to the surface via charge transfer and hybridization with the lower Pc ring, whereas at the same time, the upper Pc ring still maintains the molecular electronic features. Additionally, the weak

hybridization together with Hund's rule constrain the  $4f$ -electrons of the Nd<sup>3+</sup> to be in the same spin channel. In the PDOS calculations, the  $4f$  electrons remain fully spin-polarized in the spin-down channel and therefore make up the spin magnetic moment of the adsorbed molecule. As a consequence of these observations, the  $dI/dV$  peak measured on the center site of the molecule [orange curve in Fig. VI.6(a)] for  $V_{\text{bias}} = -0.8$  V can unequivocally be assigned to the state in the calculated PDOS [magenta curve in Fig. VI.6(b)]. Notably, the state has mainly  $4f$ -character in only the spin-down channel. For the same spectrum, the  $dI/dV$  shoulder measured for  $V_{\text{bias}} = 1.25$  V nicely agrees with the calculated PDOS for the unoccupied Nd spin-down  $4f$ -states at the same energy. The excellent agreement between calculated and experimentally obtained electronic structure of the adsorbed NdPc<sub>2</sub> molecule leads to the conclusion that the Nd  $4f$ -states are directly accessible by scanning tunneling microscopy. This important result is a consequence of the specific characteristics of the NdPc<sub>2</sub> molecule in contrast to other late-lanthanide double-decker Pc, where the  $4f$ -states were not directly accessible [22, 36]. The main differences between the previously studied LnPc<sub>2</sub> molecules and the NdPc<sub>2</sub> molecule lie in the position of the  $4f$ -states with respect to the Fermi energy and in their spatial extension. Both have to be in a range to offer the possibility for sufficient hybridization with the surrounding ligand system (see Chapter II).

Accordingly, we identify the  $dI/dV$  features obtained above the ligand site of the molecule with the PDOS, calculated for the upper Pc ring. We obtain good agreement between the  $dI/dV$  shoulder measured at the ligand site (grey curve) for  $V_{\text{bias}} = +1.2$  V and the calculated unoccupied states with sharp PDOS features of the upper Pc ring. The red arrow in Fig. VI.6 (b) marks one of the positions in the PDOS, where the weak coupling via hybridization of the two Pc rings through the Nd  $4f$ -states is directly visible in the calculation. All three components exhibit a slightly larger spectral weight at this point indicating that hybridization occurs at this energetic position.

It is important to note that the choice of the Hubbard parameter for the  $4f$ -states ( $U = 2.2$  eV) leads to a self-consistent result. It was chosen to reproduce the experimental  $dI/dV$  features for the occupied states. Importantly, this choice leads automatically to an energy match for the unoccupied states, again emphasizing the good agreement between the experimental results and the calculations.

Intriguingly, this agreement does not seem to hold for the broad  $dI/dV$  peak measured at the ligand site for  $V_{\text{bias}} \approx -0.7$  V. The corresponding PDOS features of the upper Pc ring, which tentatively could be assigned to it, are closer to the Fermi energy by  $\approx 0.5$  eV at  $V_{\text{bias}} = -0.25$  V. To solve this apparent mismatch it is necessary to take a closer look at the main conceptual differences of the STM experiment and the DFT calculation. While DFT investigates the electron densities in the ground state of the system, the STM experiment is a transport experiment, detecting electrons tunneling with certain probabilities between overlapping states of the two electrodes, tip and sample. This tunneling occurs due to the applied electric field between the sample and the tip. Certainly, the electric field can influence the states of the probed sample, so that conventional DFT calculations miss the experimental result. Therefore, in order to qualitatively understand how the electric field generated by the applied bias voltage during the STM experiment can influence the

electronic structure of the NdPc<sub>2</sub> molecule adsorbed on the Cu(100), an uniform electric field was included in the calculations as visualized in Fig. VI.6 (c) and (d). According to the physical conventions, positive electric fields are generated by negative bias voltages.

As a result, the electric field shifts the PDOS peak of the upper Pc ring located initially at  $\approx -0.2$  eV to lower energies as indicated by the black arrows in Fig. VI.6(b)-(d). With increasing electric fields, it gradually approaches the position of the occupied 4*f*-derived peak, resulting in a weak hybridization at  $V_{\text{bias}} = -0.7$  V. This shifted peak can therefore be identified with the occupied feature in the experimental  $dI/dV$  obtained on the ligand site of the molecule. It is important to note that the influence of the electric field shift on the Nd 4*f*-states is much less pronounced than on the states of the upper Pc ring with mainly molecular character. This difference originates from the fact that the Nd 4*f*-states are spatially more localized around the nuclei of the lanthanide atom compared to the extended molecular states. For the same reason, the electric field barely modifies the strongly hybridized electronic states of the lower Pc ring. In summary, the shift of the hybrid molecule-surface states with molecular character at the upper Pc ring by applying an external electric field is correlated to the already mentioned specific character of the bonding inside the NdPc<sub>2</sub> double-decker molecule: The upper Pc ring is mainly electrostatically bound to the Nd 4*f*-states with only a small hybridization. Therefore its molecular orbitals are only weakly altered upon adsorption on the surface. The ability of an external electric field to shift molecular orbital states is an additional important result of this study. It will be discussed later in this Section again, since it opens up new prospects for potential applications in spintronic devices.

Further evidence for the above drawn conclusions can be achieved by investigation the spatial extent of the spectroscopic features. Therefore  $dI/dV$  maps were measured for a variety of bias voltages corresponding to the bias range of the  $dI/dV$  spectra in Fig. VI.6. The  $dI/dV$  images were obtained simultaneously to constant current STM images as described in Chapter III.

The  $dI/dV$ -maps in Fig. VI.7(a) and (b) correspond to the two main features in the  $dI/dV$ -curve measured at the center site positioned at  $V_{\text{bias}} = -0.8$  V and  $+1.25$  V in the orange curve in Fig. VI.6 (a). At these energetic positions, the  $dI/dV$ -maps should represent the fully spin-polarized 4*f*-orbitals, as they were identified by a comparison of the measured  $dI/dV$ -spectra and the PDOS data before. For a comparison of the experimental results with the calculations, corresponding images were extracted from the volume data set of the projected charge density. The values were chosen according to the extracted isosurfaces in Fig. VI.5 that were taken from the data volume set of the integrated projected charge density. This means that for every lateral point  $x$  and  $y$  of the molecule, the same  $z$ -value as for the isosurfaces in Fig. VI.5 is chosen and the respective value for the projected charge density is plotted in the theoretical images in Fig. VI.7 (i) – (l). The theoretical calculations for the same bias voltages shown in Fig. VI.7 (i) and (j) are in a very good agreement, reproducing the main features of the experimental data. Both images for  $V_{\text{bias}} = -0.8$  V show a high spectral weight in the four-fold symmetry of the molecule with lines of similar signal height leaving the center along the main axes of the



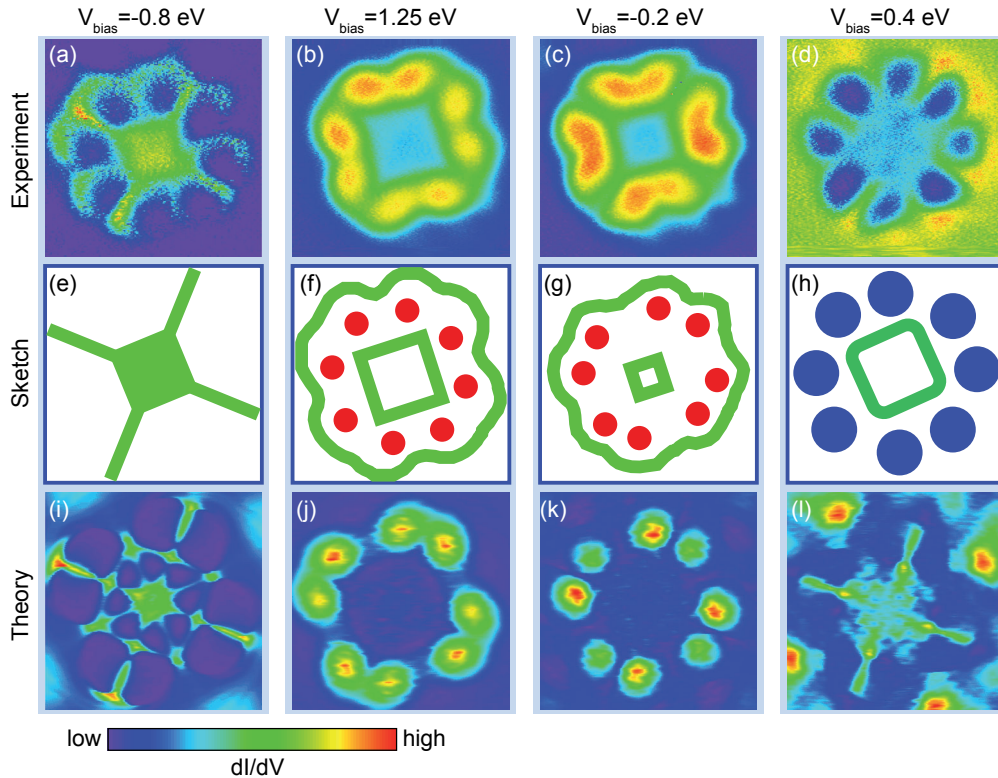


**Figure VI.7.:** (a)-(d)  $dI/dV$  maps of the NdPc<sub>2</sub> molecule. The images were simultaneously recorded with the constant current STM images shown in Fig. VI.5. (i)-(l) Corresponding images of the the calculated charge density of the adsorbed molecule. (e)-(h) For an easier comparison, the main features of both the experimental and calculated maps are visualized. ( $I_T = 1$  nA, bias voltages as indicated in the image. Color code is individually scaled. STS parameters:  $f_{\text{mod}} = 2.7$  kHz,  $V_{\text{mod}} = 30$  meV rms. Image sizes:  $2.7 \times 2.7$  nm<sup>2</sup>)

upper Pc ligand. The general shape is sketched in the central row of Fig. VI.7. In contrast to the high signal in the central part of the molecule, the ligands appear much lower, again present in both, experimental and calculated data. The agreement of experiment and calculation also holds for the two corresponding images at  $V_{\text{bias}} = 1.25$  V. The central part exhibits low spectral weight with the typical four-fold symmetry, whereas the highest signal is located at the eight lobes of the four benzene-like rings of the upper Pc ring. Splendidly, also the asymmetric signal intensity on each benzene-like ring is reproduced by the *ab-initio* calculations. This asymmetry of the spectral weight stems from asymmetric charge transfer between the lower Pc ring of the molecule and the substrate inducing chirality in the achiral NdPc<sub>2</sub> molecule, similar to what is described by Mugarza *et al.* for CuPc on Ag(100) [80]. The influence of the bonding of the lower Pc and the surface is surprising, since the coupling between the two Pc ligands is known to be weak. However,

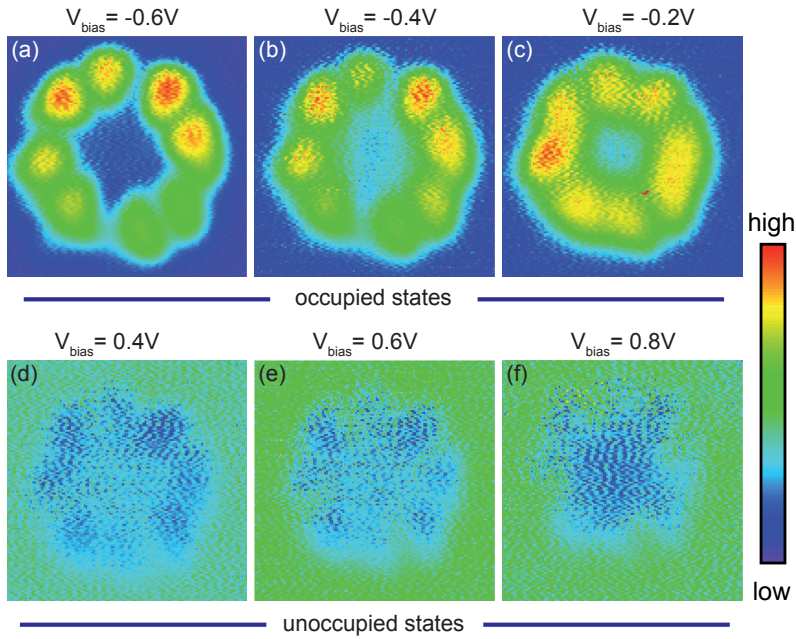


**Figure VI.8.:**  $dI/dV$  images of a NdPc<sub>2</sub> molecule in the adsorption configuration A. Several images for the bias range between  $V_{\text{bias}} = -0.7$  and  $V_{\text{bias}} = 1.25$  V are shown to visualize the contrast change on the ligand site of the molecule for occupied and unoccupied states. Color code is individually scaled. [ $V_{\text{bias}}$  as indicated in the image, tunneling current: (a), (b), (d) and (e)  $I_{\text{T}} = 1$  nA and (c) and (f)  $I_{\text{T}} = 0.5$  nA. Image sizes:  $2.8 \times 2.8$  nm<sup>2</sup>]

there has to be a weak but sufficient electronic coupling between both Pc rings, otherwise double barrier tunneling behavior should be present in the  $dI/dV$  spectra in Fig. VI.6 [77].

The good agreement between experiment and simulation confirms that the 4*f*-states contribute to the transport through the molecule as already concluded from the comparison of  $dI/dV$  spectra and PDOS calculations. According to the calculated spin-resolved PDOS curves in Fig. VI.6(b)-(d) they carry the spin magnetic moment of the adsorbed molecule, so that spin-polarized electron transport is possible by accessing these states via STM.

The reliability and accuracy of our first-principles calculations is also proven by reproducing the experimentally observed inversion of the  $dI/dV$  contrast in the energy range between  $V_{\text{bias}} = -0.8$  and  $+1.25$  V. We identify this region with the gap between the highest occupied molecular orbital (HOMO) and lowest unoccupied molecular orbital (LUMO) of the NdPc<sub>2</sub> molecule adsorbed on Cu(100). In Fig. VI.7 (c) and (d), two representative images for  $V_{\text{bias}} = -0.2$  and  $0.4$  eV in the gap region are shown, respectively. The main spectroscopic features are again reproduced by the DFT calculations shown in Fig. VI.7 (k) and (l). For negative bias, the ligands show higher spectroscopic weight compared to the four-fold symmetric center, whereas for positive bias voltages lower signal is observed on the ligands compared to the central part of the molecule.

This inversion of the contrast between the occupied and unoccupied states is observed throughout the gap region as shown in Fig. VI.8 for a different molecule in the second



degenerate adsorption position. The occupied ligand states exhibit higher signal compared to the unoccupied ones. This observation in comparison to the measured  $dI/dV$  spectra in Fig. VI.6 (a) leads to another puzzling mismatch. Inside the gap region the  $dI/dV$  signal shows almost no contribution which would lead to the conclusion that the same observation should be present in the spatial spectroscopy measurements. In contrast to that, large signal is measured on the ligands. This apparent mismatch can be solved by again taking the electric field effect into account. In the PDOS calculations for different applied electric bias fields in Fig. VI.6 (b)-(d), the peak located inside the gap of the upper Pc ring shifts towards lower energies by applying higher electric fields. This means, by applying different bias voltages in the STM experiment, this peak gives rise to the signal on the ligand site of the molecule for the occupied states depending on the size of the applied bias voltage. In addition, the calculations have shown that applying an electrical field in the other direction doesn't shift the peak to unoccupied states. This observation is in agreement with the low spectral weight on the ligands of the molecule in the experiment.

### VI.3. Conclusion and Perspectives

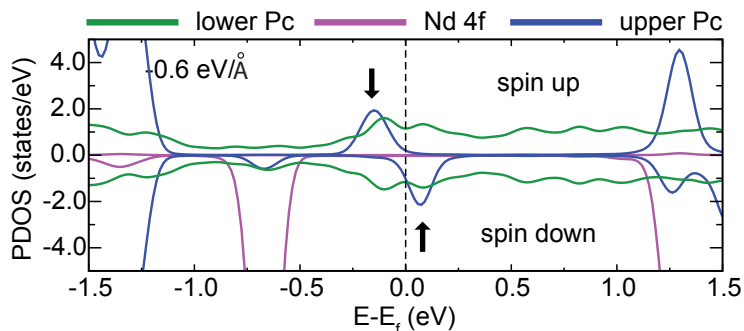
In conclusion it was shown that the  $\text{NdPc}_2$  double decker molecule fulfills important requirements for the implementation in future spintronic devices:

- The molecule chemisorbs strongly to the Cu(100) surface and binds in specific degenerate adsorption sites, which is the basic requirement to construct an electrical device. The strong bonding is identified by DFT calculations, which exhibit broad band like PDOS structures for the lower Pc ring.
- Due to the double decker structure with an electrostatic bonding between the two negatively charged Pc rings and the positively charged central atom, which is only modified by a very weak hybridization, molecular-like orbitals of the upper Pc ring are still observed after adsorption. This important characteristic is identified by the topography images that show eight-lobe structures, similar to those calculated for the free molecule or observed for single-decker molecules adsorbed on insulating surfaces. Additionally, the comparison of the spectroscopic features of the molecule with DFT calculations show clear indication of the presence of molecular orbitals in the adsorbed molecule. The presence of molecular orbitals in an electrical device offers the possibility to gain precise control of the current voltage characteristics of the device.
- These molecular orbitals can be modified by external electric fields, so that an additional degree of freedom is available that can be controlled by applying different external electric fields.
- For the  $\text{NdPc}_2$  molecule adsorbed on Cu(100) it is possible to get direct access to the fully spin-polarized  $4f$ -orbitals of the central Nd atom by the STM transport experiment. These  $4f$ -states are identified based on their spectral position and spatial

extent by comparing STS and *ab initio* calculations. This access was not achieved for other late-lanthanide double-decker Pc, like TbPc<sub>2</sub> and stems from the proper energetic and spatial location of the 4*f*-orbitals in the Nd atom. This immediate access offers the possibility to directly read and write the spin-state of the molecule by electrical means as it is required for all electrical spintronic devices.

Further results of the calculations of Nicolae Atodiressei [81] that show interesting features are discussed in the following. After the shift of the molecular type states of the upper Pc ring by applying external electric fields was observed, a closer investigation of the influence of fields with higher values and opposite signs has been applied to the hybrid molecule-surface system. Both parameters are not simple to change in the STM experiment, but can be easily tuned in the *ab initio* calculations. The resulting PDOS for external electric fields with opposite sign is shown in Fig. VI.9. The peak initially located at  $\approx -0.2$  eV shifts under the influence of the field further into the direction of the Fermi energy and becomes spin-split with the occupied states mainly in the spin-up and the unoccupied states mainly in the spin-down channel.

**Figure VI.9:** Calculated PDOS for the lower Pc, the central Nd atom and the upper Pc with high negative external electric field. A spin-splitting of the molecular orbitals of the upper Pc ring is induced at the Fermi energy.



This very interesting and unexpected observation opens up prospects to implement these molecules into three terminal spintronic devices. The spin-splitting could be enabled and disabled by an external electric field, for example generated by a gate voltage. At the same time, an electric current flowing along the upper Pc ring could read out the spin state of the upper ring of the double-decker molecule. This is of course far away from being straightforward. There are several challenges concerning molecular electronics, like for instance the controlled connection of the molecule to source and drain.

For a more comprehensive investigation of the magnetic properties of the NdPc<sub>2</sub> molecule it would be useful to perform spin-polarized STM measurements on the adsorbed molecule and compare the results to *ab initio* calculations. This can either mean, to adsorb the molecule on a ferromagnetic surface, to which the magnetic moment of the molecule would couple, or to investigate the time dependent magnetic signal of the molecule adsorbed on a non-magnetic surface. In the course of this work a lot of effort was done towards spin-polarized STM investigations, but only preliminary results could be achieved for NdPc<sub>2</sub> adsorbed on the ferromagnetic surface of the second AL of Fe on W(110). These results will be discussed in Chapter VIII.

---

## Iron on Tungsten

---

Iron on tungsten is a prominent example for a magnetic system that is widely investigated by spin-polarized scanning tunneling microscopy [52, 56, 82, 83]. This circumstance originates from the unique magnetic characteristics in the first few AL of Fe growing on atomically flat W(110) that opened up a variety of questions which could be solved on the nanometer scale by applying SP-STM. One of the puzzling challenges was the exact description of the domain walls in the second AL growing as thin stripes along the step edges of the underlying crystal. It was finally solved by a combination of SP-STM with theoretical investigations and will be further discussed in the course of this Chapter. Since the magnetization directions of the system are well understood, it can serve as a model system for SP-STM and assist characterizing the magnetization vector of the (magnetic) STM tip. This information is crucial for investigations of unknown systems. We particularly chose the second AL of Fe on W(110) for further SP-STM investigations of the  $\text{NdPc}_2$  molecule presented in Chapter VIII. The ferromagnetic surface is used as a substrate for the molecules. This opens up the possibilities to have a substrate that blocks the otherwise superparamagnetic magnetization of the molecule in a certain direction, so that it is accessible in the quasistatic SP-STM measurements and to use domains of the substrate to measure two of the magnetization directions of the molecules in a single scan.

In the beginning of this Chapter a general introduction into the first three AL of thin Fe films grown on W(110) concerning the topographic and electronic, and thus, the magnetic properties is given. In the last two decades numerous experiments and theoretical studies have been performed towards the detailed understanding of the system. The main focus is therefore lying on the presentation of previous results that are crucial for the understanding of the experimental data shown in this Chapter. Of importance is the description of the domain walls in the second AL of Fe. On the basis of these previous results, measurements on the second AL by means of SP-STM with bulk chromium tips are presented in the main part of this Chapter. Investigations of the domain walls in the second AL of iron are discussed and the electronic and geometric characterization of the Cr-tip is carried out on the basis of the SP-STM measurements on the ferromagnetic surface.

## VII.1. Previous Results

In the first few AL of epitaxially grown Fe on W(110), drastic changes in the morphology as well as in the electronic and hence magnetic properties are observed. These large variations for different coverages mainly result from the large lattice mismatch of the two materials iron and tungsten. Both metals exhibit in bulk crystals the body-centered cubic structure with lattice constants of  $a_W = 3.165 \text{ \AA}$  and  $a_{Fe} = 2.866 \text{ \AA}$  [84]. This leads to a large lattice strain of  $(a_W - a_{Fe})/a_W = 9.4\%$ . The changes of structural and electronic characteristics with increasing coverages have been studied in the past two decades with a variety of different methods. For instance, low energy electron diffraction [85–87], scanning tunneling microscopy [88–90] and Auger electron spectroscopy [85–87] were applied to get insight in the structural properties and the chemical composition, whereas the electronic characteristics were investigated using SP-STM, conversion electron Mössbauer spectroscopy [91] and magneto-optical Kerr effect measurements [92–94]. SP-STM and STS is hereby of high significance, since it offers the possibility to investigate the structure of the magnetic domains and domain walls within nanometer resolution.

### VII.1.1. Topography

Induced by the large lattice mismatch, dislocation lines and networks appear in the thin Fe films with increasing coverage, until the Fe film is fully relaxed and reaches its pristine lattice constant at a coverage of four AL [89]. Independent of the growth temperature, the first AL as shown in Fig. VII.1(a), nucleates in islands on the W substrate until it covers the surface completely. The layer is pseudomorph which means that the Fe atoms are arranged so that they have the lattice constant of the underlying W. This is a result of the higher surface energy of the W substrate compared to Fe ( $\gamma_W = 3.5 \text{ J/m}^2$  and  $\gamma_{Fe} = 2.9 \text{ J/m}^2$  [95]) that tends to reduce the free energy of the system by completely covering the substrate. The growth of the additional layers is temperature dependent, though it can be modified by subsequent annealing at temperatures of 550 K. The topography and electronic structure discussed in the following are those of the annealed sample. The second AL starts growing on the closed first layer. Due to the enhanced mobility during annealing the Fe atoms move to the step edges of the W crystal and form so called nanowires along the step edges as shown in Fig. VII.1(b). The shape of the nanowires is influenced by the orientation of the step edges of the crystal. They show smooth edges, if the step edges of the substrate are oriented along the  $[001]$ -axis [94, 96] as it is often the case in Fig. VII.1(b), or they exhibit rougher edges the more the direction of the step edges of the substrate are oriented into the  $[1\bar{1}0]$ -direction [97] see Fig. VII.1(c). For coverages between one and two AL, the surface will be similar to the STM topography image shown in Fig. VII.1(b) and the corresponding three dimensional plot in Fig. VII.1(d).

On each terrace of the W substrate, both the second AL and the first AL are visible. This is the coverage regime that is focused on by the spin-polarized STM measurements discussed in the course of this Chapter. The second AL also starts growing pseudomorphically on the first AL until it develops dislocation lines along the  $[001]$ -direction. At the dislocation

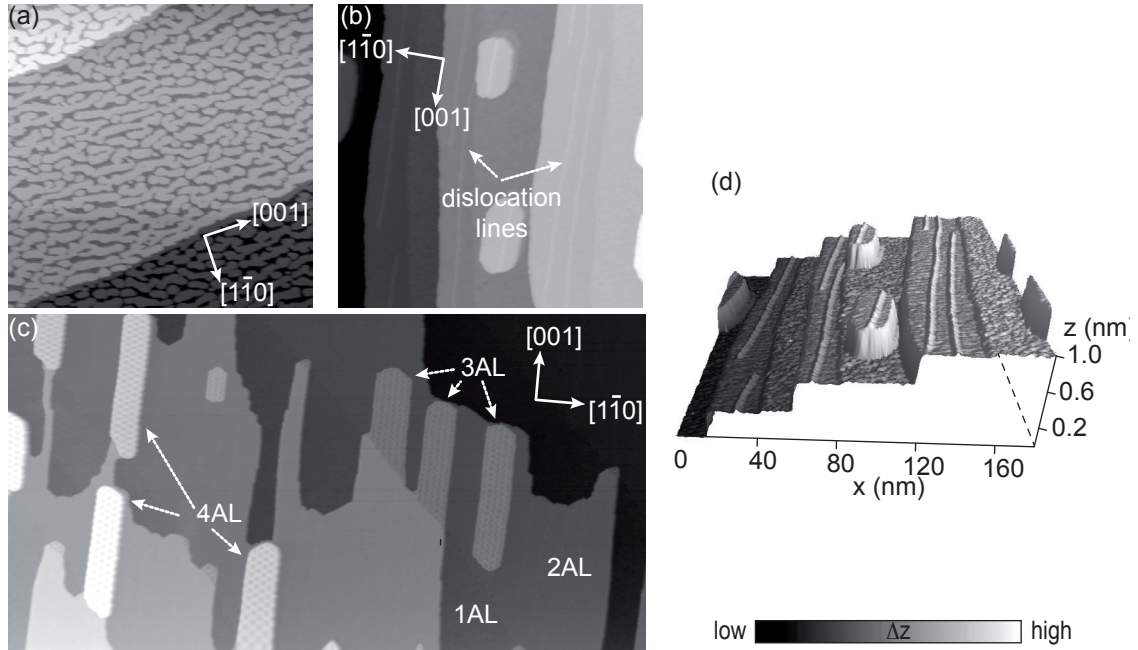


**Figure VII.1.:** (a) STM topography image of the first AL of Fe on W(110). The islands grow pseudomorphically to the W substrate with a preferred growth along the [001]-direction. ( $V_{\text{bias}} = -0.5 \text{ V}$ ,  $I_T = 3 \text{ nA}$  Image size:  $200 \times 200 \text{ nm}^2$ ) (b) The atoms of the second AL moved to the step edges forming nanowires. The dislocation lines appear brighter at this bias voltages. ( $V_{\text{bias}} = -0.3 \text{ V}$ ,  $I_T = 1 \text{ nA}$  Image size:  $180 \times 180 \text{ nm}^2$ ) (c) The first four AL can be identified due to their specific dislocation patterns: pseudomorphic growth without pattern in the first layer, dislocation lines in the second layer, an almost two dimensional pattern in the third and a fully two dimensional pattern in the fourth atomic layer. ( $V_{\text{bias}} = -0.5 \text{ V}$ ,  $I_T = 3 \text{ nA}$  Image size:  $200 \times 186 \text{ nm}^2$ ) (d) Three dimensional representation of the STM image shown in (b).

lines additional rows of atoms account for a relaxation of the strain. The dislocation lines of the second AL can be identified in the Figs. VII.1(b) and (c) as slightly brighter lines in the [001] direction. From the practical point of view, they are very useful during the STM experiment, since they are exclusively found in the second AL and therefore clearly help to identify the thickness range of the Fe wedge on the surface. Before the second AL is complete, the third AL starts growing in islands along the direction of the dislocation lines of the second layer. It exhibits a regular dislocation pattern which is extended into a fully two dimensional dislocation pattern in the fourth AL growing on the islands of the third layer. These first four layers of the Fe covering the W(110) crystal are identified in Fig. VII.1(c).

### VII.1.2. Electronic and Magnetic Properties

The main part of this Section deals with the magnetic properties of the second AL of Fe on W(110). Nevertheless for a comprehensive picture the magnetic properties of the other

layers should be mentioned briefly before the characteristics of the second AL are discussed in detail. In the first AL the magnetization is in the plane of the surface (in-plane) along the  $[1\bar{1}0]$ -direction with a Curie temperature of  $T_C = 230\text{ K}$  [88]. A spin reorientation occurs in the second AL, where the surface is magnetized along the surface normal (out-of-plane). All subsequent layers on top of the second one are again magnetized in-plane initially along the  $[1\bar{1}0]$ -direction with a transition into the  $[001]$ -direction for coverages exceeding 22 AL [98].

### Second Atomic Layer: Domains and Domain Walls

The magnetic configuration of the nanowires of the second AL depends on the total coverage and on the terrace width of the underlying W crystal. For very narrow terraces with width around 10 to 15 nm long out-of-plane domains are observed with rare domain walls. Two neighboring stripes exhibit in most cases antiparallel magnetization direction which results in terrace-wise antiferromagnetic coupling as a consequence of dipolar coupling [83]. On wider terraces as shown those in the images of Kubetzka *et al.* [52] in Fig. VII.2 the stripes on the terraces no longer form very long domains, but show a domain structure with alternating domains with an average length of around 20 nm. The transition from long to short domains is caused by the stray field of the out-of-plane domains [82,99]. The coupling between layers on adjacent terraces depends on the coverage and terrace size. Figure VII.2 (a) shows the second AL of Fe completely covering the surface. The magnetic contrast in the  $dI/dV$  is plotted in black and white on top of the topographic image. Here, a GdFe coated STM tip with out-of-plane sensitivity is used to map the alternating domains. In addition to this image, the magnetization is investigated with an in-plane sensitive Fe-coated tip to map the magnetic contrast in the domain walls. The result is shown in Fig. VII.2 (b), however for a different coverage. The domain wall extend along the  $[1\bar{1}0]$ -direction and the normal  $[001]$ -direction is called the domain wall propagation direction. The domain wall width is approximately 7 nm [56,99]. Subsequent domain walls exhibit alternating black and white contrast, indicating a helical magnetization rotation with fixed rotational sense.

Possible configurations of this so called spin-spiral are shown in Fig. VII.3. The spiral can either be right- or left-rotating and from helical or cycloidal type [100]. In an helical spiral, the magnetization rotates from one out-of-plane domain to the other in form of a Bloch wall. That means that while rotating, the magnetization points perpendicular to the domain wall propagation direction. Depending on the rotational sense of the wall, the spin spiral is then called left- or right-handed. The magnetization in the domain wall in a cycloidal spiral rotates along the domain wall propagation direction in form of a Néel wall. For a better visualization, both wall types are sketched in Fig. VII.4. Due to a lack of experimental proof it was initially believed that the spiral is of helical type and the magnetization rotates in form of a Bloch wall inside the domain walls. In these studies the Dzyaloshinskii-Moriya (DM) interaction was neglected [99,102] and the domain sizes were explained by long-range demagnetization fields [102]. In general the DM interaction becomes important for broken inversion symmetry at the sample surface together with

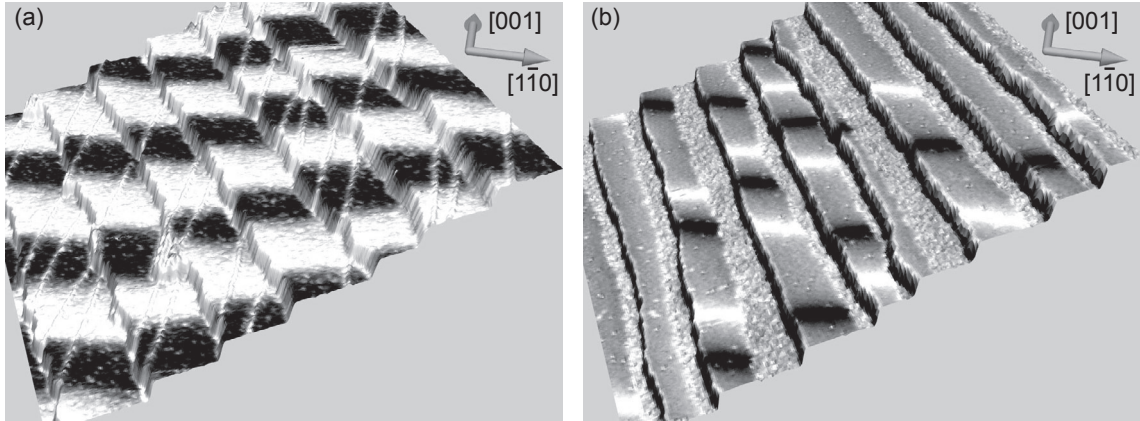


**Figure VII.2.:** Topographic STM images colored with the  $dI/dV$  signal of the second AL of Fe on W(110) showing the magnetic structure for different coverages. (a) The second AL completely covers the first AL and the domain structure is measured with a GdFe-coated tip sensitive to the out-of-plane magnetization of the domains of the sample. ( $V_{\text{bias}} = -0.45 \text{ V}$ ,  $I_{\text{T}} = 0.3 \text{ nA}$ ) (b) The first AL is still visible at this slightly lower coverage. The magnetization is recorded with an in-plane sensitive Fe coated tip. Contrast is therefore observed in the domain walls. Here the domain walls exhibit alternating black and white contrast, indicating a magnetization rotation with fixed rotational sense. ( $V_{\text{bias}} = -0.1 \text{ V}$ ,  $I_{\text{T}} = 0.3 \text{ nA}$ ) Image taken from [52].

spin-orbit coupling [100]. It is an antisymmetric magnetic interaction, known to induce spiral magnetic states on surfaces [103,104], but is beyond the scope of this work and will therefore not be discussed in detail. On the experimental side, the main limiting factor was based on the lack of external magnetic fields in the microscopes. To determine the type and rotational sense of the spin-spiral it is necessary to apply magnetic fields along the in-plane directions of the sample. In early studies, the role of the DM interaction was mentioned as a possible explanation of the rotational sense of the spin-spiral [54], since this observation could not be explained by the applied models [102]. However only in later works [105,106] the DM interaction was included into the theoretical discussion and led to a consistent explanation of the experimental findings. Micromagnetic calculations including the DM

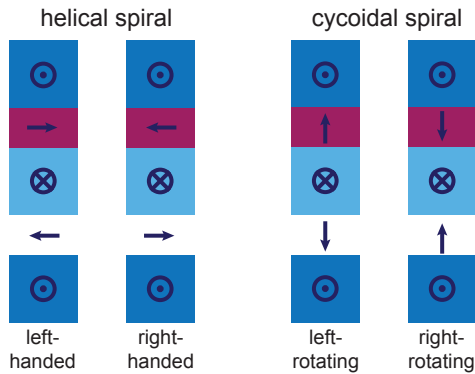
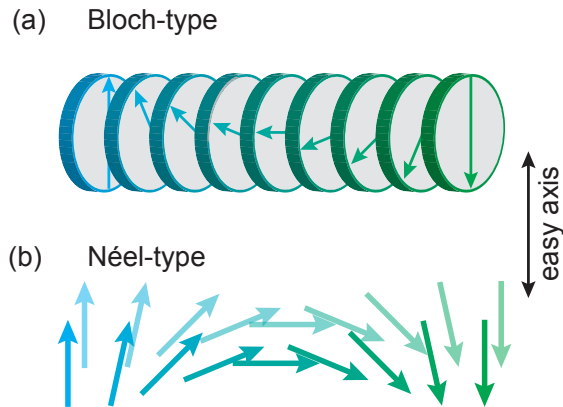


**Figure VII.3:** Sketch of the two spiral types with opposite rotational sense that potentially explain the observed alternating domain wall contrast in Fig. VII.2(b). In the helical spiral, the magnetization rotates in form of a Bloch wall, in the cycloidal spiral it rotates as a Néel wall. As in [100].

**Figure VII.4:** The magnetization rotates by  $180^\circ$  from one easy axis direction to the other, either in form of (a) a Bloch wall, where the magnetization points perpendicular to the domain wall propagation direction or in form of (b) a Néel-type, where the magnetization is aligned into the direction of the domain wall propagation direction [101].



interaction could figure out the cycloidal right-rotating spin spiral but failed to explain for example the domain sizes in the nanometer range. Here the DM vector as most important parameter was determined by DFT calculations [105]. Finally an experimental study by Meckler *et al.* [106] with in-plane magnetic fields in combination with micromagnetic calculations, in which the DM vector was extracted from the experimental data, was able to explain the observed domain geometries and the cycloidal type with right-rotating sense of the magnetization.

## VII.2. SP-STM Investigations on the 2nd Monolayer of Fe on W

### VII.2.1. Mapping the Surface

The magnetic properties of the surface are investigated by spin-polarized scanning tunneling microscopy. Depending on the direction of the magnetization of the STM tip, it is sensitive to magnetic regions of the sample that point in-plane or out-of-plane and the  $dI/dV$  signal is proportional to the scalar product of the two magnetization vectors of sample and tip ( $\vec{m}_t \cdot \vec{m}_s$ ) (see Chapter III). From the experimental point of view, as described in Chapter IV, it is challenging to fabricate tips with initially defined magnetic properties, so that in consequence, the actual configuration has to be figured out in every new experiment. In some cases the magnetic STM tip does not show any sensitivity to the magnetization of the sample at all. Since also the preparation of the sample does not guarantee a magnetic surface, one needs a clear indication to be able to distinguish between a non magnetic surface or an, in general, in-plane sensitive tip. Fortunately, the system Fe on W offers a clear mechanism for this purpose: the in-plane domain walls and the out-of-plane domains of the second AL exhibit a difference in the electronic structure which is in general detectable even with non-magnetic tips [107, 108]. The resulting image for a magnetic surface independent from the magnetic configuration of the tip is shown in Fig. VII.5.

The differential conductivity of the surface is measured at a bias voltage of  $V_{\text{bias}} = 50$  meV, where the magnetic surface exhibits a bright and dark contrast between the domains and the domain walls. No difference between the two domains and domain walls with different



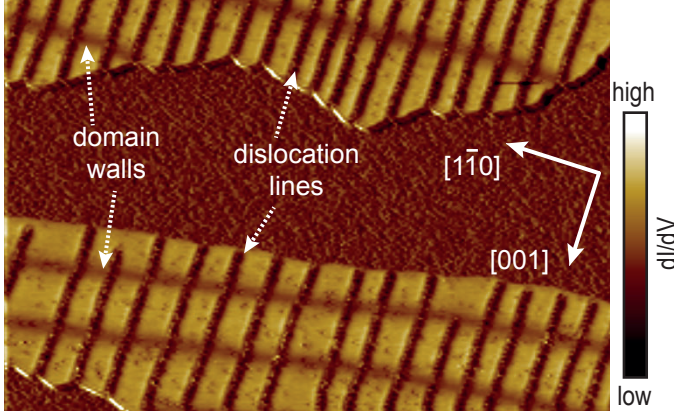


**Figure VII.5:**  $dI/dV$  map at  $V_{\text{bias}} = 50 \text{ mV}$  of the second AL of Fe on W(110). The dislocation lines appear dark and are aligned along the  $[001]$ -direction. The domain walls are clearly visible as dark lines along the  $[1\bar{1}0]$ -direction. The contrast results from the influence of the spin-orbit coupling on the band-structure and depends on the local magnetization direction relative to the easy axis. ( $I_T = 1 \text{ nA}$ , image size:  $200 \times 136 \text{ nm}^2$ )

magnetization directions is necessarily observed. The contrast results from a mixing of states with  $d_{z^2}$  and  $d_{xy+yx}$  symmetry induced by the spin-orbit coupling in the second AL of Fe on W(110). As a consequence of the mixing of these states, the density of states of the surface depends on the magnetization direction of the sample. Areas with the magnetization aligned along the hard or the easy axis of the surface exhibit different density of states [108]. This difference is especially present at  $V_{\text{bias}} = 50 \text{ meV}$ . The investigation of the domain wall contrast at  $V_{\text{bias}} = 50 \text{ meV}$  is therefore the starting point of every investigation of the magnetic properties of the second AL of Fe on W(110) by STM.

### VII.2.2. Out-of-plane Domains

To investigate the out-of-plane domains of the second AL of Fe on W(110),  $dI/dV$ -maps at different bias voltages are recorded. A Cr bulk tip with out-of-plane sensitivity is used for that purpose. The result is shown in Fig. VII.6 for three different bias voltages exhibiting clear magnetic contrast in the domains. These images can be compared to Fig. VII.5 showing the spin-orbit coupling related effect at  $V_{\text{bias}} = 50 \text{ mV}$ . From the position of the domain walls in Fig. VII.5, the bright-dark contrast of the  $dI/dV$ -maps in Fig. VII.6 can unambiguously assigned to a contrast resulting from magnetization direction of the apex atom of the antiferromagnetic Cr-tip and the different magnetization directions of the surface. The largest spin-related contrast is observed in Fig. VII.6 (a) at  $V_{\text{bias}} = -0.3 \text{ V}$ . This is an observation that holds for all experiments done on the second AL with different Cr bulk tips. Another distinct feature is the contrast reversal of the domains in Fig. VII.6 (b) at  $V_{\text{bias}} = -0.1 \text{ V}$  in comparison to the maps in (a) and (c) recorded at  $V_{\text{bias}} = -0.3$  and  $0.7 \text{ V}$ , respectively.

For a detailed investigation of the surface,  $dI/dV$ -spectra are measured above two domains with different magnetization directions. Figure VII.7 shows the result in a bias voltage range between plus and minus  $1 \text{ V}$  for the two domains (I) and (II) as marked in the insets. These insets show excerpts of the  $dI/dV$ -maps of Fig. VII.6 and relate the contrast inversion in the  $dI/dV$ -maps to spectroscopic features.

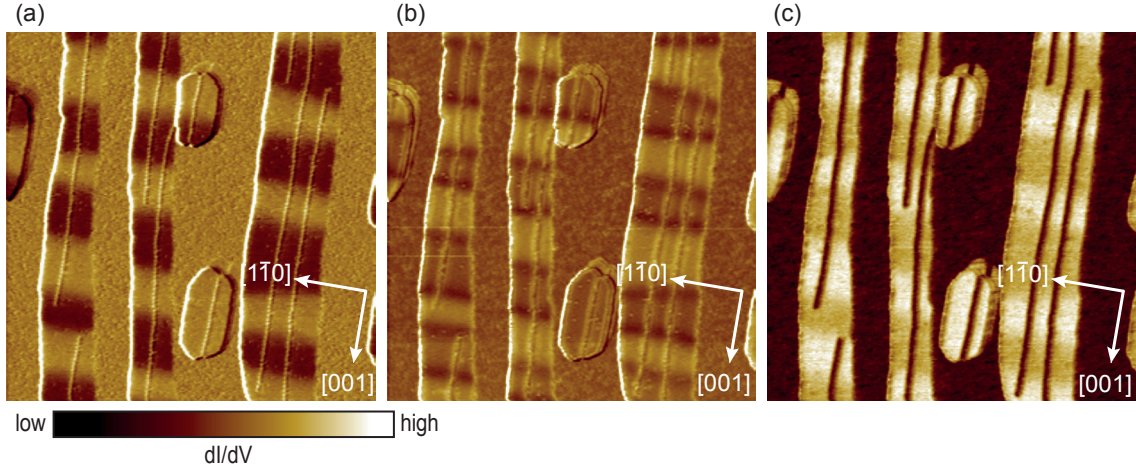


**Figure VII.6.:**  $dI/dV$  maps of the second AL of Fe on W(110) showing distinct out-of-plane spin contrast. Images recorded at (a)  $V_{\text{bias}} = -0.3$  V,  $I_{\text{T}} = 2.5$  nA, (b)  $V_{\text{bias}} = -0.1$  V,  $I_{\text{T}} = 1.6$  nA and (c)  $V_{\text{bias}} = 0.7$  V,  $I_{\text{T}} = 3$  nA. For  $V_{\text{bias}} = -0.1$  V a contrast reversal compared to the other images is observed. Color code is individually scaled. (Image sizes:  $180 \times 180$  nm<sup>2</sup>)

The STS-spectra show three distinct peaks on both domains at  $V_{\text{bias}} = -0.3$ ,  $-0.1$  and  $0.7$  V. In first-principles DFT calculations of the second atomic layer, states of  $d_z^2$  character at  $-0.08$  and  $+0.7$  V have been found [107]. They are located at the  $\Gamma$  point of the Brillouin zone. According to Stroscio *et al.* [109] these states should be most easily detected and therefore appear in the experimental spectra. In consequence, the peaks in the experimental STS spectra at approximately  $V_{\text{bias}} = -0.1$  and  $0.7$  V can be identified with these states. In contrast to this observation, the feature located at  $V_{\text{bias}} = -0.3$  V can not be assigned to a dominant state of the Fe surface. It was nevertheless observed throughout all the experiments done with different Cr-tips on different Fe films on W. According to the Tersoff and Hamann model, explained in Chapter III, the local density of states of the tip is assumed to be structureless. This assumption is valid in the case of investigating unoccupied sample states, but fails in many cases for the occupied states of the sample. Here, the energy dependence of LDOS of the tip has larger influence on the measured signal, as already explained in detail in Chapter III. We therefore assign the peak at  $V_{\text{bias}} = -0.3$  V to features in the LDOS of the chromium tip.

The identification of the exact local density of states of the STM tip is challenging, since the atomic configurations at the apex of the tip are in general not known. Nevertheless it is possible, under certain assumptions about the tip configurations, to apply first-principles calculations to the problem. Ferriani *et al.* [110] carried out first-principles DFT calculations modeling the tip as a single Cr atom on top of a Cr(001) surface. The upper panel of Fig. VII.8 shows the resulting LDOS for minority and majority states in a large energy range for the single Cr apex atom (colored) and the bare Cr surface (gray). The apex atom couples antiferromagnetically to the surface as can be identified by the splitting of the LDOS in bonding and antibonding parts and its overlap with the bands of

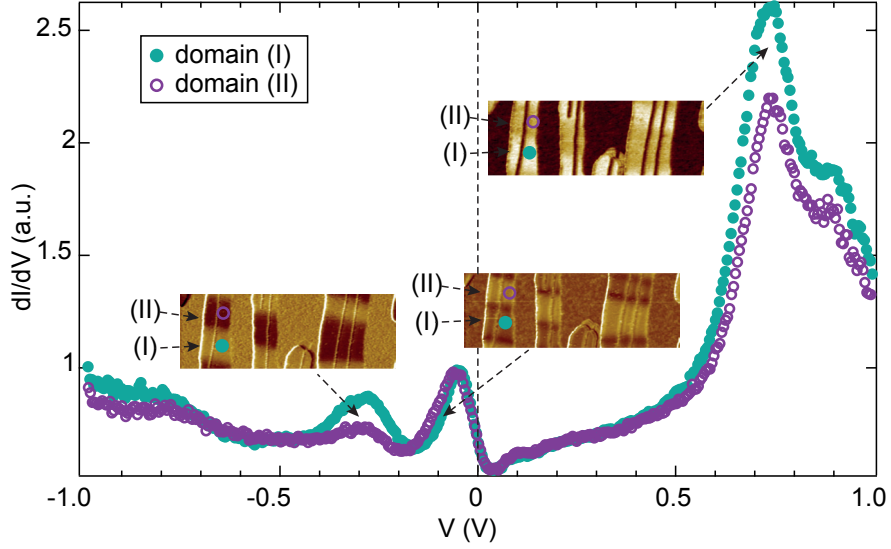
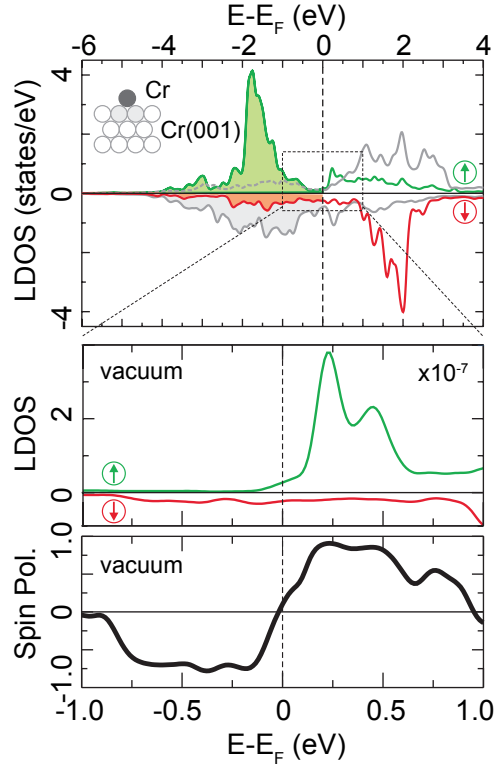


**Figure VII.7.:**  $dI/dV$  spectra recorded above the two different out-of-plane domains of the second AL of Fe on W(110). The domains (I) and (II) are marked in the  $dI/dV$  maps shown as insets. Both,  $dI/dV$  spectra and maps exhibit the contrast reversal around  $V_{\text{bias}} = -0.1$  V. (Tip stabilized at  $V_{\text{bias}} = -1$  V,  $I_T = 1$  nA,  $V_{\text{mod}} = 20$  mV rms.)

the surface. The bonding part of the LDOS has mainly majority spin character and only small minority contributions. The contributions of bonding and antibonding parts of the apex atom are only minor in the vicinity of the Fermi energy. Hybrid states of  $s$ ,  $p$  and  $d$  character dominate the vacuum LDOS of the tip as shown in the central panel of Fig. VII.8 making up the large majority contribution at 0.2 and 0.4 eV. The spin-polarization of the vacuum LDOS 5.9 Å above the Cr apex atom, as shown in the lower panel, reaches almost 100% and changes sign at the Fermi level. These calculations of the LDOS of a model Cr-tip help interpreting the measured data assuming that the model fits to our STM tip. The peak at  $V_{\text{bias}} = -0.3$  V in the STS-spectrum occurs due to the overlap of the large LDOS in the unoccupied states of the tip with occupied states of the Fe surface. Since the influence of the tip is higher for occupied sample states, the Cr states at this bias voltage are dominant in the STS spectra and distinct features appear even if the contribution of the Fe surface is low.

Another observation in the experimental spectra of Fig. VII.7 is the spin-dependent signal height measured on the two domains (I) and (II). The two features at  $V_{\text{bias}} = -0.3$  and 0.7 V show a reversal of the relative signal height. For 0.7 V domain (I) exhibits higher signal than domain (II), whereas at  $-0.1$  V the situation is vice versa. The relative signal height again undergoes a reversal and the peak at  $V_{\text{bias}} = -0.3$  V behaves like the one at the unoccupied sample states. This observation is in agreement with the  $dI/dV$ -maps in the inset taken from Fig. VII.6. Since it is known from first-principles DFT calculations that the two Fe surface states at  $V_{\text{bias}} = -0.1$  and 0.7 V are both of minority spin character [107], this change in contrast is surprising, but can be easily explained by taking into account

**Figure VII.8:** First-principles DFT calculation modeling the tip apex as a single Cr atom on top of a Cr(001) surface. Upper panel: Local density of states (LDOS) of the Cr atom (colored) and the Cr(001) surface atoms (gray) for minority and majority states. Central panel: vacuum LDOS of minority and majority states at a distance of 5.9 Å from the Cr apex atom. Lower panel: spin-polarization of the vacuum LDOS. Taken from Ferriani *et al.* [110].



the spin-polarization of the tip. As shown in the lower panel of Fig. VII.8, it undergoes a sign reversal at the Fermi energy that is directly visible in the contrast change of the experimental data following the formula (III.13) derived in Chapter III. This observation is a reminder that the interpretation of SP-STM results has to be done carefully, taking into account that there are bias voltage dependent contributions from both tip and sample electrodes.

### VII.2.3. Domain Wall Investigations

In the introduction into the magnetic properties of the second AL of Fe on W(110) presented in Section VII.1.2 it is shown that the description and characterization of the domain walls has attracted a great deal of attention over the past years.

By applying SP-STM measurements on the nanowires, as it has been done in this work and presented in the last Section, it is possible to extract information about the profile of the domain walls. To this end line sections are taken from the  $dI/dV$ -maps across an area of a  $360^\circ$  rotation of the magnetization as indicated in the lower panels of Fig. VII.9. The two images are taken with two different Cr bulk tips on different samples but at the same bias voltage. The extracted domain wall profiles are fitted by the formula

$$y(x) = y_0 + y_{\text{sp}} \cos \left( \theta^* - \sum_{i=1}^2 \arccos \left[ \tanh \frac{x - x_i}{w/2} \right] \right) \quad (\text{VII.1})$$

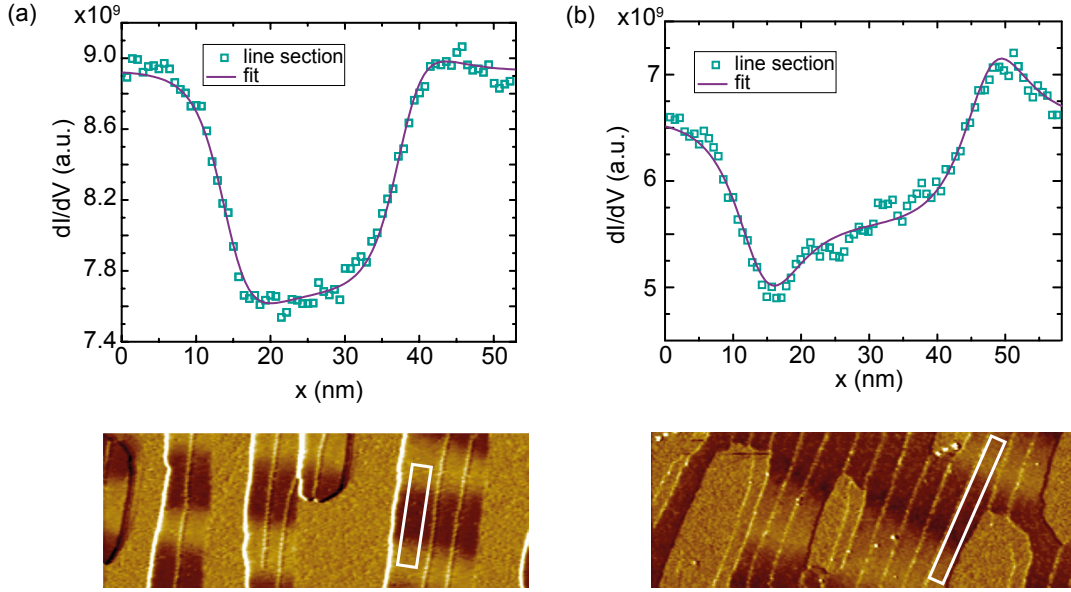


**Figure VII.9.:** Line sections taken across a  $360^\circ$  rotation of the magnetization in the out-of-plane domains as indicated in the  $dI/dV$ -maps in the lower panel. The line sections are averaged inside the white rectangles. The upper panel shows the two respective line sections together with a fit of the domain wall as explained in the text. (a) shows almost exclusively out-of-plane signal, while (b) exhibits a large in-plane contribution of the  $dI/dV$  signal. [(a)  $V_{\text{bias}} = -0.3$  V,  $I_T = 2.5$  nA, (b)  $V_{\text{bias}} = -0.3$  V,  $I_T = 1.5$  nA]

representing two homogeneous  $180^\circ$  domain wall profiles [56]. The fit gives information about the domain wall width  $w$  and the angle  $\theta^*$ . The angle  $\theta^*$  is widely assumed to stand for the angle of the tip magnetization with respect to the easy axis of the sample magnetization [56]. The parameters  $y_0$  and  $y_{\text{sp}}$  are the spin-averaged and the spin-polarized contributions to the signal, respectively and  $x_i$  ( $i = 1, 2$ ) represents the centers of the domain walls. The domain wall profile in Fig. VII.9 (a) shows mainly contrast in the out-of-plane domains and the fit parameters result into  $w = (7.0 \pm 0.3)$  nm and  $\theta^* = (23.1 \pm 3.4)^\circ$ , with  $w$  being close to values found in previous studies [56, 99]. The fit of the domain wall in Fig. VII.9 (b) yields a slightly larger value for  $w = (8.2 \pm 0.3)$  nm and an angle  $\theta^* = (62.6 \pm 1.7)^\circ$ . The shape of the profile indicates a larger in-plane contribution as it is obvious in the image in (b). This observation together with the larger angle  $\theta^*$  is in agreement with the assumption that  $\theta^*$  represents the angle between tip magnetization and easy axis.

It will be shown that in Eq. (VII.1), the angle  $\theta^*$  can only be considered to be the angle of the tip magnetization with respect to the easy axis of the sample within limitations, but that formula (VII.1) can be applied in all cases and gives in general reasonable results for the domain wall width  $w$ .



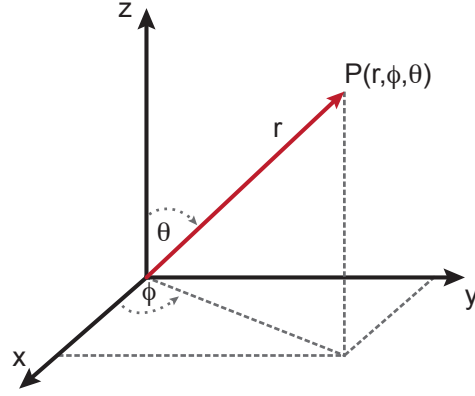
As derived in Eq. (III.17) in Chapter III, the  $dI/dV$ -signal is proportional to a sum of the spin averaged and the spin dependent signal, where the spin dependent signal results from a scalar product of the two magnetization vectors of tip and sample

$$dI/dV \propto y_0 + y_{\text{sp}}(\vec{m}_t \cdot \vec{m}_s). \quad (\text{VII.2})$$

Total-energy minimization for a Néel wall, with a magnetization profile into the direction of the domain wall propagation, yields according to [105] the following

$$\vec{m}_s = \begin{pmatrix} \sin \theta_s \\ 0 \\ \cos \theta_s \end{pmatrix} = \begin{pmatrix} 1/\cosh\left(\frac{x-x_i}{w/2}\right) \\ 0 \\ \tanh\left(\frac{x-x_i}{w/2}\right) \end{pmatrix}. \quad (\text{VII.3})$$

**Figure VII.10:** Definition of the spherical coordinate system used in this work. Here,  $r$ ,  $\theta$  and  $\phi$  represent the radial distance, the polar and the azimuthal angle, respectively.



We use spherical coordinates as they are defined in Fig. VII.10. By definition, the easy axis of the sample magnetization points along the  $z$ -axis and the propagation direction of the domain wall is along the  $x$ -axis. In addition, inside the Néel wall, the  $y$  component in general vanishes. In consequence also the angle  $\phi_s$  vanishes. The magnetization vector of the tip  $\vec{m}_t$  underlies no restrictions and is defined as

$$\vec{m}_t = \begin{pmatrix} \sin \theta_t \cos \phi_t \\ \sin \theta_t \sin \phi_t \\ \cos \theta_t \end{pmatrix}. \quad (\text{VII.4})$$

To derive an expression for the domain wall profile that can be fitted to the measured  $dI/dV$  signal, the scalar product in Eq. (VII.2) has to be calculated and yields:

$$\vec{m}_t \cdot \vec{m}_s = \underbrace{\sin \theta_t \cos \phi_t \sin \theta_s}_{\text{in-plane profile}} + \underbrace{\cos \theta_t \cos \theta_s}_{\text{out-of-plane profile}} \quad (\text{VII.5})$$

The scalar product of the two magnetization vectors results into a linear combination of the two magnetization profiles. The first term proportional to  $\sin \theta_s$  stems from in-plane

magnetization components of the sample, whereas the second term arises from out-of-plane components. Any magnetic configuration of the tip and sample leads thus to a wall profile that is a superposition of the two terms. The coefficients are given by  $\sin \theta_t \cos \phi_t$  and  $\cos \theta_t$ , respectively.

In the case of a magnetization vector of the tip restricted to the  $x$ - $z$  plane which means  $\phi_t = 0$  and  $\cos \phi_t = 1$ , Eq. (VII.5) is reduced to

$$\vec{m}_t \cdot \vec{m}_s = \sin \theta_t \sin \theta_s + \cos \theta_t \cos \theta_s \quad (\text{VII.6})$$

By applying the addition theorem  $\cos(x - y) = \cos x \cos y + \sin x \sin y$ , and taking into account  $\cos \theta_s = \tanh(2(x - x_i)/w)$  from Eq. (VII.3) yields formula (VII.1) with  $\theta^*$  being the angle  $\theta_t$  between tip and easy axis of the sample magnetization

$$\vec{m}_t \cdot \vec{m}_s = \cos(\theta_t - \theta_s) \quad (\text{VII.7})$$

$$= \cos\left(\theta_t - \arccos\left[\tanh\frac{x - x_i}{w/2}\right]\right) \quad (\text{VII.8})$$

Equation (VII.8) is only valid for the restriction that  $\phi_t = 0$ , i.e. the special case when the tip magnetization lies in the plane defined by the surface normal and the direction of the domain wall propagation. This rather strong assumption cannot be expected to be fulfilled for a given pair of tip and domain wall. Thus, the widely used fit to Eq. (VII.1) [56] does not yield precise information about the magnetization vector  $\vec{m}_T$ . For the general case we return to Eq. (VII.5) and note that fitting the experimental  $dI/dV$ -profiles can only yield the relative strength of the in-plane and out-of-plane contributions, i.e. the ratio of the coefficients in the superposition. In order to take this fact into account we parameterize the coefficients in polar coordinates.

$$\vec{m}_t \cdot \vec{m}_s \stackrel{!}{=} c \sin \theta^* \sin \theta_s + c \cos \theta^* \cos \theta_s \quad (\text{VII.9})$$

The ratio of the two contributions

$$\frac{c \sin \theta^*}{c \cos \theta^*} = \tan \theta^* \quad (\text{VII.10})$$

is given by the parameter  $\theta^*$  and independent of  $c$ . Thus  $\theta^*$  can be obtained by fitting the experimental domain wall profiles.

Applying the addition theorem to Eq. (VII.10) as before, yields

$$\vec{m}_t \cdot \vec{m}_s = c \cos\left(\theta^* - \sum_{i=1}^2 \arccos\left[\tanh\frac{x - x_i}{w/2}\right]\right) \quad (\text{VII.11})$$

i.e. Eq. (VII.1) from literature is recovered for the general case. But what is the meaning of the parameter  $\theta^*$ ?

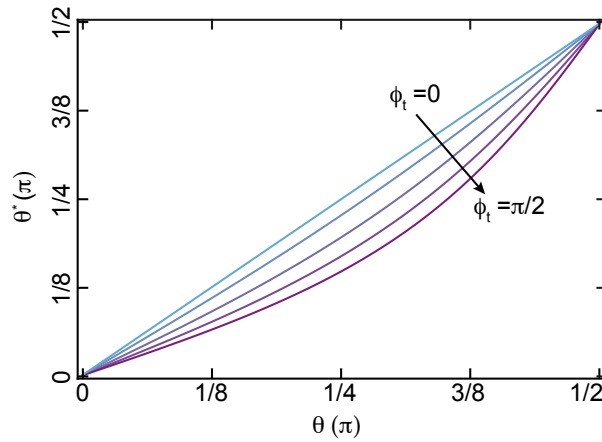
Comparing Eqs. (VII.5) and (VII.9) yields

$$\frac{\sin \theta_t \cos \phi_t}{\cos \theta_t} = \frac{c \sin \theta^*}{c \cos \theta^*} \quad (\text{VII.12})$$

$$\tan \theta_t \cos \phi_t = \tan \theta^* \quad (\text{VII.13})$$

This relation can be evaluated graphically by plotting the equation  $\theta^* = \arctan(\tan \theta_t \cos \phi_t)$  for different azimuthal angles  $\phi_t$  as shown in Fig. VII.11. For a vanishing azimuthal angle

**Figure VII.11:** Graphic evaluation of the relation between  $\theta_t$  and  $\theta^*$  different azimuthal angles  $\phi_t$  of the tip magnetization. The angle  $\theta^*$  underestimates the value of the angle  $\theta_t$  in the general case. Exception is the special case  $\phi_t = 0$ .



$\phi_t$ , the two values are the same and in Eq. (VII.13), the parameter  $\theta^*$  is equal to the angle between easy axis of the sample magnetization and the tip magnetization vector. Since the cosine is a monotonically decreasing function in the chosen angle range, the parameter  $\theta^*$  is understood as an angle that in all cases underestimates the polar angle  $\theta_t$ . As a result for the two different  $\theta^*$  derived from the data fits in Fig. VII.9, the value underestimates the true angle, but gives an impression of the sensitivity to the in-plane component of the magnetization. For a full characterization of the magnetization vector of the tip, it is necessary to map the contrast of well known magnetic systems, with all three magnetization components. That means, both in-plane and the out-of-plane component, as they are present in magnetic vortices [111] or skyrmions [104] for instance.

In summary, the parameter  $\theta^*$  underestimates the true angle  $\theta$  between the tip and sample magnetization easy axis. However, the fitting of the measured domain walls with Eq. (VII.1) extracts reliable values for the domain wall width  $w$  of the order of a few nm for the second AL of Fe on W(110). This represents an example for measurements of a magnetic structure size on the nm scale by means of spin-polarized STM.



---

**NdPc<sub>2</sub> Adsorbed on Fe on W(110)**

---

For the implementation of molecules in any sort of device it is, as already mentioned before, crucial to understand the structural properties of the molecule and its magnetic interactions after adsorption on substrates. This is of particular interest in case of ferromagnetic surfaces and electrodes. It has been shown that paramagnetic molecules, such as metal porphyrins and phthalocyanines can couple to the magnetization of ferromagnetic substrates [25, 112]. The magnetization of the paramagnetic molecules is stabilized by the substrate, and they do not function as independent magnetic units, but can be used as an organic magnetic layer. The coupling is induced for example by indirect exchange coupling through the nitrogen atoms in an Fe porphyrin on Co or Ni substrates as shown by Wende *et al.* [25] or by superexchange through an additional oxygen layer between the ferromagnetic Co and Ni substrate and the magnetization of an Fe porphyrin as shown by Bernien *et al.* [113]. In addition, direct exchange mechanisms of ferromagnetic surfaces, such as Co and Fe with Co phthalocyanine have been observed via STM by Iacovita *et al.* [112] and Brede *et al.* [21] respectively.

If the experimental investigation of a single molecular magnet is done on time-scales longer than the typical magnetization relaxation time of the molecule, an external magnetic field or a stabilizing ferromagnetic support is required. Note that in our STM chamber no external magnetic field is available. For the SMM TbPc<sub>2</sub> it was observed that magnetic hysteresis is only present below 7 K if the time-scale of the observation is below 100 s [33, 114]. Hence, an investigation of the magnetization of a lanthanide double-decker phthalocyanine, such as the NdPc<sub>2</sub>, by STM can only be achieved, if the magnetization of the molecule is coupled to a ferromagnetic substrate. In case of the TbPc<sub>2</sub> SMM deposited on Co it has been shown by STM that a direct coupling of the Tb ion to the surface magnetization is unlikely, because of the high spatial and energetic localization of the 4*f*-orbitals in the Tb. It was therefore claimed that the coupling is mediated by the lower Pc ring and that a direct observation of the Tb 4*f*-states is not possible [36]. Furthermore, the investigation of the TbPc<sub>2</sub> on Ni by x-ray magnetic circular dichroism showed that the magnetization of the TbPc<sub>2</sub> is antiferromagnetically coupled to the Ni surface. The stability of the magnetic

moment is enhanced and in contrast to the single-decker paramagnetic phthalocyanines it was observed that the molecule still functions as a separate magnetic unit [23], i.e. the magnetization of the molecule can be switched to be parallel or antiparallel to the surface magnetization by applying suitable external fields.

The NdPc<sub>2</sub> molecule, in contrast to the late lanthanide TbPc<sub>2</sub> analogue, offers a higher probability of a direct coupling between the 4*f*-states of the Nd ion and the ferromagnetic surface. In addition, it allows direct access to the 4*f*-orbitals by STM as discussed in Chapter VI. Both are a consequence of the higher spatial extent of the orbitals of the central Nd ion and their energetic position closer to the Fermi energy as compared to the Tb ion. This direct accessibility and the assumption, that the NdPc<sub>2</sub> molecule functions as a separate magnetic unit, similar to what is shown by Lodi Rizzini *et al.* [23] makes the molecule a promising candidate for a molecular magnetic unit that is readable and writeable by purely electrical means.

For a systematic spin-polarized STM and STS study of the NdPc<sub>2</sub> coupled to a ferromagnetic layer certain general requirements have to be fulfilled, which are (1) the surface layer has to remain ferromagnetic after the deposition of the molecules, (2) the molecules have to be adsorbed in defined and reproducible positions on the clean surface and (3) the total molecule coverage has to be large enough to allow investigations of two molecules in degenerate adsorption position on two neighboring magnetic domains with opposite magnetization directions in the same STM and STS image. The latter is a consequence of the definition of the spin-dependent  $dI/dV$ -signal given in Eq. (III.17) in the theoretical Chapter III:

$$dI/dV(\vec{r}_0, V, \Theta) \propto n_t n_s(\vec{r}_0, E_F + eV) + m_t m_s(\vec{r}_0, E_F + eV) \cos \Theta(\vec{r}_0). \quad (\text{VIII.1})$$

Here, the total  $dI/dV$ -signal stems from a superposition of a topographic and a spin-dependent signal. To eliminate the contribution of the topographic signal, measurements taken for opposite magnetization direction have to be subtracted from each other. In consequence, it is necessary to compare the results of the spin-polarized spectroscopy data obtained on a molecule coupled to a domain pointing into a certain direction, with the data measured on a different molecule on a domain with opposite magnetization direction. This can in principle also be achieved by changing the magnetization direction of the molecule or the tip by applying an external magnetic field while focussing on only one single molecule. Our experimental setup however does not provide an external magnetic field.

## VIII.1. Topographic and Electronic Structure

For the investigations of the NdPc<sub>2</sub> molecule adsorbed on a ferromagnetic substrate, we choose the widely investigated second AL of Fe on W(110). The magnetic and topographic properties of this surface layer are discussed in detail in Chapter VII. The second AL offers all required properties for the investigation of the molecule with SP-STM without external magnetic field. It serves on the one hand as a system for the characterization of

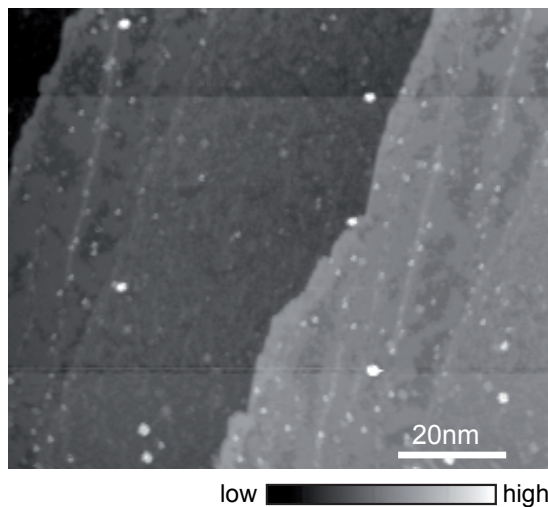


**Figure VIII.1:** Constant current STM images of the second AL of Fe on W(110) with adsorbed NdPc<sub>2</sub> molecules. They adsorb on the first AL of Fe and on the second AL mainly close to the dislocation lines.  $I_T = 1$  nA and  $V_{\text{bias}} = -0.3$  V

the tip magnetization vector and exhibits on the other hand a magnetization easy axis perpendicular to the surface plane, compatible with the easy axis of the magnetization of the molecule that is assumed to be aligned perpendicular to the plane of the molecule [33].

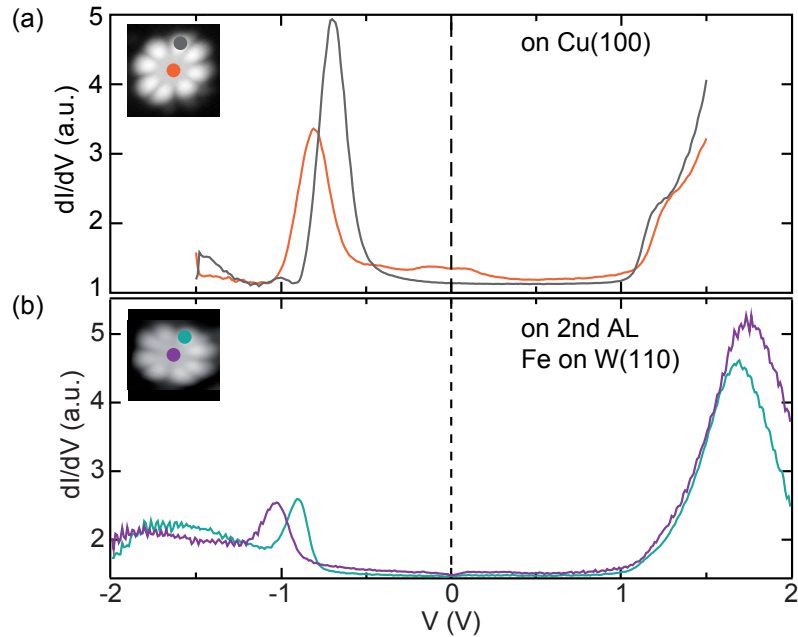
In the experiment, the molecules were evaporated on the second AL of Fe on W(110) as described in Chapter V. The total amount of intact molecules on the surface was low and in all experiments comparable to the observations shown in Fig. VIII.1. Here, two neighboring molecules have a distance of approximately 40 nm, which makes high resolution imaging of the internal molecular features of two molecules in one STM image almost impossible. The main reason for the low coverage is the requirement to conserve a magnetic Fe surface, which could not be achieved if the total amount of adsorbates added during the evaporation process was too high. It has been observed that the magnetism of the surface is quenched by a large amount of surface contaminations (see Chapter V). Furthermore, for a reproducible investigation of the adsorbed molecule it is important that the molecule is located on a defined adsorption site. For the phthalocyanine molecule there are three different adsorption sites on the second AL of Fe on W(110) [21]. In addition Fig. VIII.1 shows that molecules adsorb on the first AL of Fe or at one of the dislocation lines of the second AL but rarely distant from these lines. However, molecules adsorbed on a dislocation line do not exhibit a reproducible and well defined adsorption configuration and the electronic structure might be altered by the influence of the specific electronic structure of the dislocation line. Theoretical approaches like DFT become non-applicable in these cases. Therefore it is challenging to fulfill the requirements for a comprehensive spin-polarized STM and STS study of adsorbed NdPc<sub>2</sub> on this surface.

Nevertheless, it was possible to investigate the topographic and electronic structure of one single NdPc<sub>2</sub> molecule adsorbed on a flat area (i.e. distant from a dislocation line) of the second atomic Fe layer. The measurements were done with a bulk Cr-tip, but it was not possible to achieve magnetic contrast on this specific surface. Therefore the magnetization direction of the tip remains unknown. In addition, it is very likely that the magnetism

of the surface was quenched, since the domain wall contrast at  $V_{\text{bias}} = 50$  meV due to the spin-orbit coupling effect was also absent. As discussed in Chapter VII it should be present for the magnetic surface independent from the magnetization of the STM tip. Therefore the influence of the magnetization of the surface on the magnetization of the molecule was not studied. We claim that the observed differences in the topographic and spectroscopic images result from the different binding strength of the molecule adsorbed on Fe compared to the adsorbed molecule on Cu(100).

The starting point for the comparison of the adsorption of the NdPc<sub>2</sub> molecule on Cu(100) and the second AL of Fe on W(110) are the  $dI/dV$  spectra shown in Fig. VIII.2. The spectra recorded above the center and the ligand of the molecule exhibit similar characteristics on both surfaces. The occupied (HOMO) and unoccupied (LUMO) features are shifted away from the Fermi level in (b) recorded above the molecule on Fe compared to their position in (a). We identified these features in Chapter VI with the  $4f$ -states of the central Nd ion. The HOMO in (b) is located at  $V_{\text{bias}} = -1.1$  V compared to  $-0.8$  V on Cu(100) and the LUMO shifts from  $1.25$  V to  $1.7$  V. A similar shift is observed in the spectroscopy-curves recorded on the ligand of the molecule. In Chapter V, the conclusion is drawn that the larger gap between the features has its origin in a stronger hybridization of the molecule with the substrate.

**Figure VIII.2:**  $dI/dV$  spectra obtained above the center and the organic ligand of the NdPc<sub>2</sub> molecule adsorbed on (a) Cu(100) and (b) Fe on W(110). [ $f_{\text{mod}} = 2.7$  kHz,  $V_{\text{mod}} = 30$  meV rms; (a) tip stabilized at  $I_{\text{T}} = 1$  nA and  $V_{\text{bias}} = -1$  V and) (b) tip stabilized at  $I_{\text{T}} = 2$  nA and  $V_{\text{bias}} = 2$  V]



In the following the comparison of constant current STM and  $dI/dV$ -maps is presented. Here, we chose the respective bias voltages such that the compared images correspond to each other with respect to their location in the  $dI/dV$ -spectra shown in Fig. VIII.2. Namely the HOMO, the LUMO and two images in the gap and above the LUMO are shown.

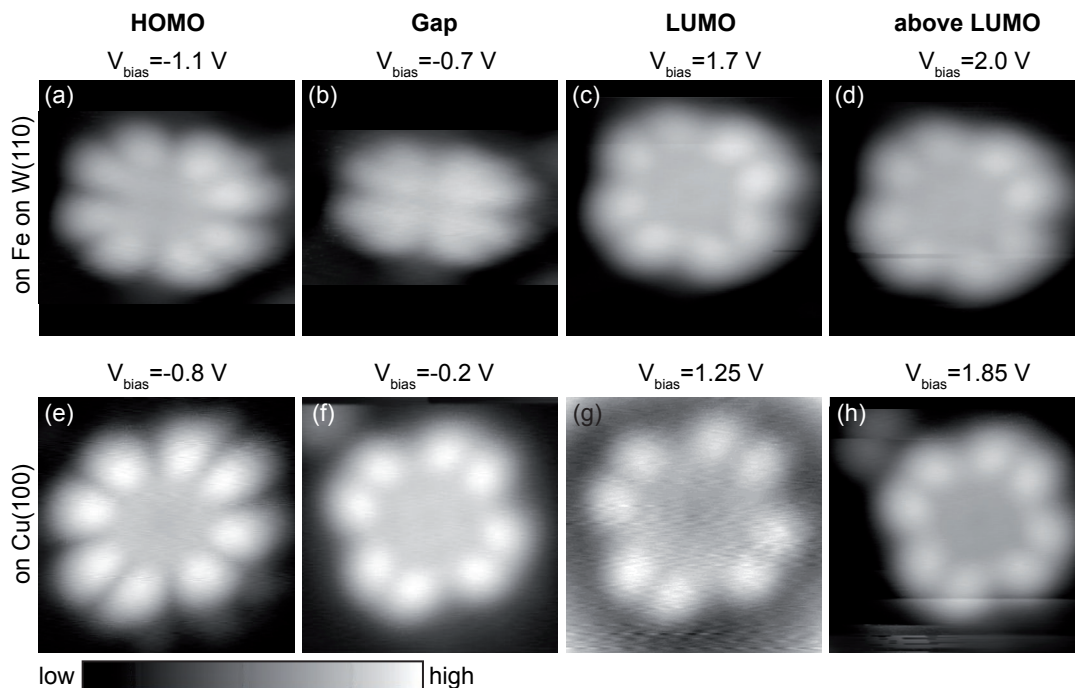


**Figure VIII.3.:** Comparison of constant current topography images of the  $\text{NdPc}_2$  molecule adsorbed on Fe on W(110) (upper row) and Cu(100) (lower row) for the HOMO, the gap, the LUMO and bias voltages above the LUMO. Bias voltages as indicated in the Figure and tunneling currents are: (a)  $I_T = 1 \text{ nA}$ , (b)  $I_T = 1 \text{ nA}$ , (c)  $I_T = 2 \text{ nA}$ , (d)  $I_T = 2 \text{ nA}$ , (e)  $I_T = 1 \text{ nA}$ , (f)  $I_T = 1 \text{ nA}$ , (g)  $I_T = 1 \text{ nA}$ , (h)  $I_T = 1 \text{ nA}$ , (i)  $I_T = 1 \text{ nA}$ . Color code is individually scaled. (Image sizes:  $2.7 \times 2.7 \text{ nm}^2$ )

Figure VIII.3 displays constant current topography images for accordingly selected bias voltages. In the upper row topographic images for the  $\text{NdPc}_2$  molecule adsorbed on Fe are shown and the corresponding images of the molecule on the Cu surface are plotted in the lower row. For the comparison, we choose the HOMO in (a) and (e) and the LUMO shown in (c) and (g). The other images represent the gap shown in (b) and (f) and the bias range above the LUMO in (d) and (h). The overall eight-lobed shape of the molecule is in good agreement with the previous observations on Cu. The central part of the molecule appears lower compared to the ligands. An exception to these observations is the image shown in (b). Here the eight-lobed structure is visible, but distorted and the central part does not show an extended flat area as it is found in general at other bias voltages. This discrepancy might arise from a distortion of the image, since it was the first scan taken on the molecule after stabilizing the tip at this new scan range. In these cases a creep of the piezo elements is more pronounced compared to the creep in images taken after a longer time at a given scan position.

Besides the topographic images we also compare the corresponding spectroscopic maps. The images are displayed in Fig. VIII.4 for the same bias voltages that have already been

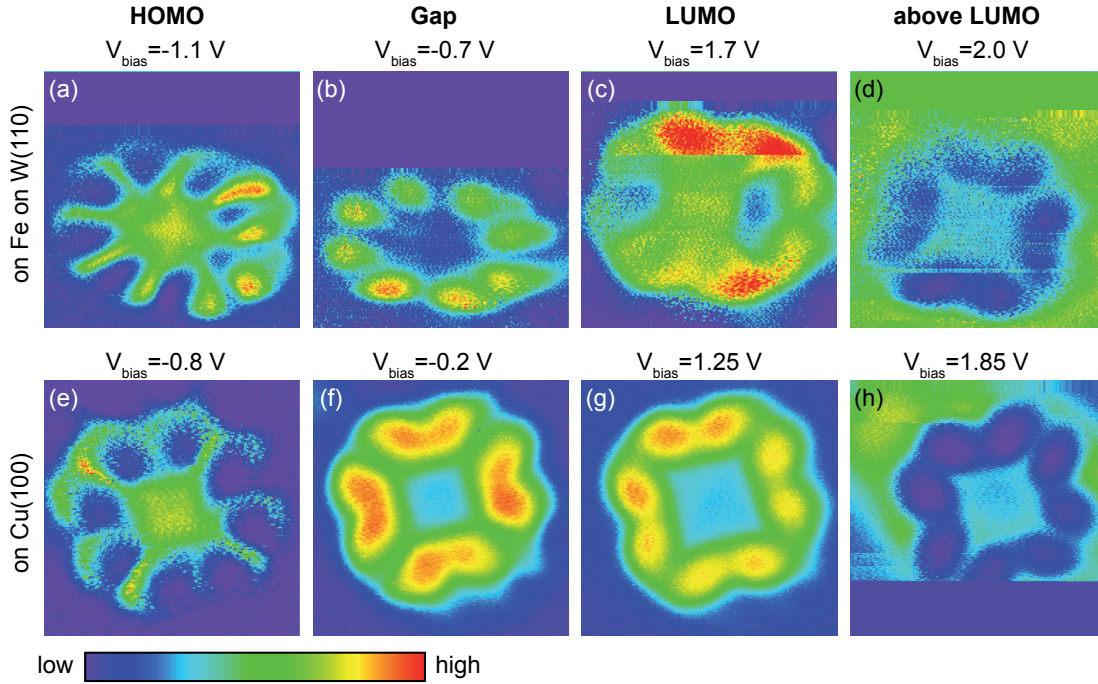


**Figure VIII.4.:** Comparison of the  $dI/dV$  maps of the NdPc<sub>2</sub> molecule adsorbed on Fe on W(110) (upper row) and Cu(100) (lower row). The images were simultaneously recorded with the constant current STM images shown in Fig. VIII.3. Bias voltages as indicated in the Figure and tunneling currents are: (a)  $I_T = 1$  nA (b)  $I_T = 1$  nA (c)  $I_T = 2$  nA (d)  $I_T = 2$  nA (e)  $I_T = 1$  nA (f)  $I_T = 1$  nA (g)  $I_T = 1$  nA (h)  $I_T = 1$  nA (i)  $I_T = 1$  nA STS parameters:  $f_{\text{mod}} = 2.7$  kHz,  $V_{\text{mod}} = 30$  meV rms. Color code is individually scaled. (Image sizes:  $2.7 \times 2.7$  nm<sup>2</sup>)

chosen for the topographic comparison. The images in (d) and (h) exhibit the same low spectral weight on the ligands as compared to the central part of the molecule. The square shaped center and contours of the ligands are also in good agreement. The images taken in the gap in (b) and (f) exhibit two differences. The spectral weight on the ligands is higher compared to the center in both images, but the contrast is larger in the molecule adsorbed on Fe. Besides the small difference in contrast, there is a larger difference in the shape. The eight lobes appear as individual features in (b), whereas there is a connection between lobes of neighboring benzene-like rings in the image shown in (f). An explanation for the different appearance can be given based on the DFT calculations of the NdPc<sub>2</sub> molecule adsorbed on Cu presented in Chapter VI. The corresponding calculated image to  $V_{\text{bias}} = -0.2$  V in Fig. VI.7 exhibits the geometrical shape of the image in Fig. VIII.4 (b) with the separated eight lobes. The shape of the ligand orbitals at this bias range might be very sensitive to the distance of the tip with respect to the molecule. The tip in (f) is closer to the surface as compared to (b), since at the same tunneling current the bias voltage in (f) is lower. A different decay into the vacuum of the wave functions of the states on the lobes and between them can explain the different appearance, if the states between

the lobes decay much faster. Therefore, additional contributions between the benzene-like rings will only be detected if the tip is closer to the surface.

Considering a magnetic tip and a possibly magnetic substrate as discussed in the beginning of this chapter, the most important differences to the observations on Cu(100) should be visible in the HOMO and LUMO. At these bias voltages we claim to have direct access to the  $4f$ -states as discussed in Chapter VI, and effects of magnetic origin should be present here compared to the images on the non-magnetic Cu(100) surface with a non-magnetic W-tip. The images in (a) and (e) corresponding to the HOMO exhibit the same molecular orbital with very similar ratio of the spectral contrast on the central part and the ligands. In contrast to this, the  $dI/dV$ -maps for bias voltages corresponding to the LUMO in (c) and (g) significantly differ from each other in the center of the molecule. The image in (c) measured on the NdPc<sub>2</sub> molecule adsorbed on Fe shows a similar contour of the ligands as in (g), but exhibits an additional high contribution to the  $dI/dV$ -signal in the center. In Chapter VI it was shown that the HOMO and LUMO, assigned to the  $4f$ -states of the Nd ion, should be in the same spin-channel. Therefore, if spin-polarized tunneling occurs, changes in the central part of the molecule should be visible for both bias voltages in Fig. VIII.4 (a) and (c). Whether these changes give rise to a positive or negative contribution to the  $dI/dV$ -signal also depends on the spin-polarization of the tip at these energies. The influence of the spin-polarization of the tip on the spin-dependent STM signal has been observed and discussed in the context of the spin-polarized STM measurements on the second AL of Fe on W(110) in Chapter VII. However, the contrast in (a) does not significantly change preventing an assured conclusion about the observation of molecular spin-contrast in these experiments.

In conclusion, the high contribution of the  $dI/dV$ -signal in the center of the molecule in (c) compared to the observations in the corresponding image on Cu can not unambiguously identified to be of magnetic origin, since neither the magnetic configuration of the tip nor the magnetization of the sample is known. Nevertheless, the enhanced central contribution is another strong evidence for the direct access to the highly spin-polarized  $4f$ -states of the Nd ion. Therefore, it remains promising to investigate the spin-polarized states of the NdPc<sub>2</sub> molecule by SP-STM.





---

## Summary and Outlook

---

In this thesis scanning tunneling microscopy and spectroscopy is used to investigate the influence of different substrates on the adsorption characteristics and electronic as well as magnetic properties of adsorbed magnetic NdPc<sub>2</sub> molecules. This molecule is in particular chosen because of its outmatching electronic structure in comparison to the late lanthanide analogues: the larger spatial extend and energetic position closer to the Fermi energy of the 4*f*-states of the central Nd ion result in a stronger hybridization with the Pc ligands and in consequence opens the door to directly access these 4*f*-states. The experiments on NdPc<sub>2</sub> first focus on the substrate dependent adsorption of the double-decker molecule, followed by a detailed investigation of the topographic and electronic structure of the molecule adsorbed on Cu(100) with a comparison to state-of-the-art density functional theory calculations. For further exploration of the magnetic properties, spin-polarized STM measurements with bulk Cr-tips are established on the second atomic layer of Fe on W(110), which in the end is used as a ferromagnetic substrate for SP-STM investigations of the adsorbed NdPc<sub>2</sub> molecule.

For an understanding of the interaction of the NdPc<sub>2</sub> molecule with surfaces of different reactivity the double-decker molecules are sublimated on various substrates. It is shown in Chapter V that the results of this thermal deposition is strongly substrate dependent. On substrates with larger binding energies, the decomposition probability of the double-decker molecule into single-decker phthalocyanines is lower than on substrates with lower binding energies. This is in contrast to the intuitive picture that the release of binding energy could destabilize the intramolecular bonds. We conclude that there has to be an additional competing effect, which stabilizes the bonding between the two phthalocyanines and the central Nd ion depending on the nature of the substrate. Since the intramolecular bonding of the double-decker is mainly of electrostatic character it is very likely that the enhanced stability has its origin in additional negative charge transferred to the organic Pc ligands that increases the intramolecular electrostatic forces.

The decomposition probability of the double-decker molecules plays an important role for further investigations of the molecules, in particular for SP-STM measurements in which a certain density of molecules on the surface is required for a successful experiment.

The comprehensive understanding of the molecule surface interaction requires a comparison of experimental results to theoretical calculations. In view of this understanding a detailed investigation of the topographic and electronic structure of the adsorbed NdPc<sub>2</sub> molecule on Cu(100) by STM and STS in combination with density functional theory calculations is presented in Chapter VI. Here it is shown, that the lower Pc ring chemisorbs to the surface, which results in two degenerate adsorption positions. Molecular-like electronic states of the upper Pc ring are still observed after the adsorption resulting from the double-decker structure and the weak hybridization between the upper and the lower ring through the Nd center. Remarkably, it is possible to modify these electronic states with the influence of an external electric field. Most importantly, the possibility to get direct access into the spin-polarized 4*f*-states of the central ion by STM is shown. This direct access is a unique characteristic of the NdPc<sub>2</sub> molecule compared to the late lanthanide double-decker molecules and opens the door for direct reading and writing of the spin-state of the molecule.

In view of the spin-polarized STM investigations of the NdPc<sub>2</sub> molecule bulk Cr-tips are used for the SP-STM study. These tips are fabricated ex-situ from Cr rods. The investigation of the influence of further in-situ preparation steps like electron beam heating in Chapter IV shows no reproducible effects but indicate a high reliability of the Cr-tips for SP-STM measurements independent of further in-situ treatments. The focus of the SP-STM measurements on the second atomic layer of Fe on W(110) in Chapter VII lies on the domain walls investigated by either purely out-of-plane sensitive tips or tips with a combination of out-of-plane and in-plane sensitivity. It is shown, that the standard fitting formula describes the domain wall itself in an adequate way but does not account for the true angle  $\theta$  between the surface normal axis and the magnetization of the tip. In general it underestimates the true value.

The reproducible fabrication and mapping of the ferromagnetic second atomic layer of Fe on W(100) is the basis for the spin-polarized STM investigations of the NdPc<sub>2</sub> molecule adsorbed on this surface. Chapter VIII shows first attempts of spin-polarized STM and STS measurements of the adsorbed double-decker molecule on an Fe surface. It was not possible to show clear spin-polarized tunneling, but the results give additional strong evidence for a direct access to the 4*f*-states of the central Nd ion by STM.

The high decomposition probability of the double-decker molecules in combination with very low thermal deposition rates on the surface is the main reason for the limited experimental results with spin-polarized STM on the Fe surface. For further investigations of the magnetic properties of the NdPc<sub>2</sub> coupled to ferromagnetic substrates it will be necessary to enhance the density of intact molecules on the surface. At the same time the number of contaminations has to be kept low, so that the thin Fe layer stays ferromagnetic.

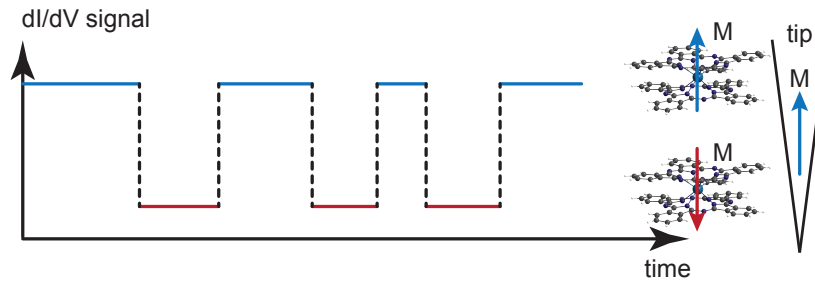


**Figure IX.1.:** Schematic time dependent  $dI/dV$ -signal of a single  $\text{NdPc}_2$  molecule adsorbed on a non-magnetic substrate. While the magnetization direction of the tip stays constant during the measurement, the spin-dependent signal fluctuates between two states corresponding to thermally induced magnetization reversals of the molecule. The relaxation time can be determined from the mean life time of the states.

These contaminations are not necessarily decomposition products of the molecule but result from the powder inside the crucible, which is not perfectly pure. For a realization of this experiment it will be mandatory to establish deposition techniques different from the thermal evaporation. These techniques can for instance be the pulsed injection method or the dry imprint technique already mentioned in Chapter V. The deposition of intact molecules is also crucial for the proposed experiments that will be discussed in the following.

Besides the investigation of the coupling of the magnetic moment of the molecule to a ferromagnetic substrate it will also be interesting for future experiments to investigate the actual single molecule magnet properties. This means the observation of the fluctuating magnetic moment of the molecule adsorbed on non-magnetic materials like Cu. Time dependent spin-polarized scanning tunneling spectroscopy offers insight into these characteristics. In the experiment the spin-dependent  $dI/dV$ -signal of a single  $\text{NdPc}_2$  molecule adsorbed on a non-magnetic surface is recorded as it is shown schematically in Fig. IX.1. A high  $dI/dV$ -signal occurs in case of a parallel alignment of the magnetization of tip and molecule, whereas a low signal occurs from antiparallel alignment. These two states are visible in the time dependent signal and a determination of the relaxation time of the magnetization of the molecule is possible by analyzing the life times of the two states. For this experiment certain requirements have to be fulfilled: the temperature has to be chosen in a way, that the time scale of the magnetization reversal is in a detectable range of the STM data acquisition. In addition a high magnetic field inside the STM is required. Applying this field generates the parallel and antiparallel configuration and the  $dI/dV$ -signals can be compared to the values of the spontaneous magnetization reversals to make sure that the detected fluctuations are of magnetic origin.

Besides the understanding of the electronic and magnetic properties of the molecules it is also important to further investigate the mechanisms of the adsorption. The bonding of the molecule to substrates and electrodes is crucial for any kind of device and a fundamental understanding will help choosing suitable substrates. Based on the results of Chapter V

it will be interesting to compare the adsorption of other molecules, e.g. late lanthanide double-decker phthalocyanines or other SMMs like  $Mn_{12}$  or  $Fe_4$  on these substrates with the results of this work. One of the key aspects here is the influence of the electron transfer on the stability of the adsorbed molecule.

Towards the implementation of molecules into devices it is important to find reproducible methods of contacting these molecules to electrodes. Currently these contacts are mainly realized by inserting molecules into gaps of so called break junctions [115] or gaps of junctions generated by electromigration of material [116]. One experimental route to enhance the reproducibility of the gaps between electrodes could be the direct growth of metallic island with defined separation. A possible system can be so called quantum size islands [117]. The size of the gaps between those islands of equal height can be controlled via the total amount of deposited material. These islands then serve as electrodes for the molecules and as contact pads for the transport measurements, e.g. by using a 4-tip STM.

With the ability to reproducibly fabricate molecular junctions it will be possible to realize so called molecular spin-valves [7] which are based on magneto-resistive effects. Besides the use of ferromagnetic electrodes connected via a non-magnetic molecule the alternative to use non-magnetic electrodes and molecules with e.g. two magnetic centers is imaginable. A possible molecular structure with two magnetic centers is shown in Fig.IX.2 [118].

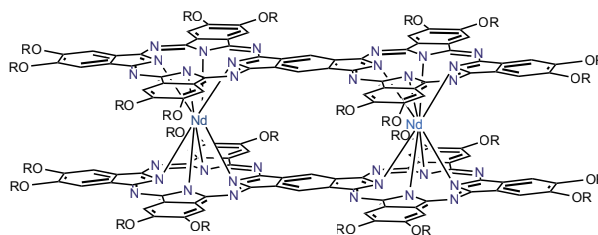


**Figure IX.2:** Possible molecular structure comprising two magnetic centers [118].

However, there are some requirements that have to be fulfilled by a molecule to function in this kind of device. The main point is the ability to switch between two well defined magnetization states in which the two magnetic centers are aligned parallel or antiparallel with respect to each other.

The results of this study concerning the adsorption characteristics and electronic properties of the  $NdPc_2$  molecule are a solid fundament of the proposed experiments. Furthermore, these experiments can in principle be realized with the current and future experimental equipment in our lab.

Only the collaboration with the chemistry group, who synthesize suitable molecular structures and the theory group, who provide detailed state-of-the-art calculations finally leads to a comprehensive and fundamental understanding of magnetic molecules on surfaces.

---

## Bibliography

---

- [1] N. J. Tao. Electron Transport in Molecular Junctions. *Nature Nanotechnology*, 1:173–181, 2006.
- [2] A. Aviram and M. A. Ratner. Molecular Rectifiers. *Chemical Physics Letters*, 29:277 – 283, 1974.
- [3] K. Moth-Poulsen and T. Bjørnholm. Molecular Electronics with Single Molecules in Solid-State Devices. *Nature Nanotechnology*, 4:551–556, 2009.
- [4] N. Ishikawa, M. Sugita, T. Ishikawa, S. Koshihara, and Y. Kaizu. Mononuclear Lanthanide Complexes with a Long Magnetization Relaxation Time at High Temperatures: A New Category of Magnets at the Single-Molecular Level. *J. Phys. Chem. B*, 108:11265–11271, 2004.
- [5] A. Cornia, A. F. Costantino, L. Zobbi, A. Caneschi, D. Gatteschi, M. Mannini, and R. Sessoli. Preparation of novel materials using smms. In Richard Winpenny, editor, *Single-Molecule Magnets and Related Phenomena*, volume 122 of *Structure and Bonding*, pages 133–161. Springer Berlin Heidelberg, 2006.
- [6] A. Naitabdi, J.-P. Bucher, P. Gerbier, P. Rabu, and M. Drillon. Self-Assembly and Magnetism of Mn<sub>12</sub> Nanomagnets on Native and Functionalized Gold Surfaces. *Advanced Materials*, 17:1612–1616, 2005.
- [7] L. Bogani and W. Wernsdorfer. Molecular Spintronics using Single-Molecule Magnets. *Nature Materials*, 7:179–186, 2008.
- [8] S. Sanvito. Molecular Spintronics. *Chem. Soc. Rev.*, 40:3336–3355, 2011.
- [9] M. N. Baibich, J. M. Broto, A. Fert, F. Nguyen Van Dau, F. Petroff, P. Etienne, G. Creuzet, A. Friederich, and J. Chazelas. Giant Magnetoresistance of (001)Fe/(001)Cr Magnetic Superlattices. *Phys. Rev. Lett.*, 61:2472–2475, 1988.
- [10] G. Binasch, P. Grünberg, F. Saurenbach, and W. Zinn. Enhanced Magnetoresistance in Layered Magnetic Structures with Antiferromagnetic Interlayer Exchange. *Phys. Rev. B*, 39:4828–4830, 1989.

## Bibliography

---

- [11] S. A. Wolf, D. D. Awschalom, R. A. Buhrman, J. M. Daughton, S. von Molnár, M. L. Roukes, A. Y. Chtchelkanova, and D. M. Treger. Spintronics: A Spin-Based Electronics Vision for the Future. *Science*, 294:1488–1495, 2001.
- [12] I. Žutić, J. Fabian, and S. Das Sarma. Spintronics: Fundamentals and Applications. *Rev. Mod. Phys.*, 76:323–410, 2004.
- [13] D. Gatteschi, R. Sessoli, and J. Villain. *Molecular Nanomagnets*. Oxford Univ. Press, New York, 2007.
- [14] M. N. Leuenberger and D. Loss. Quantum Computing in Molecular Magnets. *Letters to Nature*, 401:789–793, 2001.
- [15] M. Urdampilleta, S. Klyatskaya, J.-P. Cleuziou, M. Ruben, and W. Wernsdorfer. Supramolecular Spin Valves. *Nature Materials*, 10:502–506, 2011.
- [16] M. Mannini, F. Pineider, P. Sainctavit, C. Danieli, E. Otero, C. Sciancalepore, A. M. Talarico, M.-A. Arrio, A. Cornia, D. Gatteschi, and R. Sessoli. Magnetic Memory of a Single-Molecule Quantum Magnet Wired to a Gold Surface. *Nature Materials*, 8:194–197, 2009.
- [17] W. Wernsdorfer, M. Murugesu, and G. Christou. Resonant Tunneling in Truly Axial Symmetry Mn<sub>12</sub> Single-Molecule Magnets: Sharp Crossover between Thermally Assisted and Pure Quantum Tunneling. *Phys. Rev. Lett.*, 96:057208, 2006.
- [18] F. Branzoli, M. Filibian, P. Carretta, S. Klyatskaya, and M. Ruben. Spin Dynamics in the Neutral Rare-Earth Single-Molecule Magnets [TbPc<sub>2</sub>]<sup>0</sup> and [DyPc<sub>2</sub>]<sup>0</sup> from  $\mu$ SR and NMR Spectroscopies. *Phys. Rev. B*, 79:220404, 2009.
- [19] N. Atodiresei, V. Caciuc, P. Lazić, and S. Blügel. Chemical versus van der Waals Interaction: The Role of the Heteroatom in the Flat Absorption of Aromatic Molecules C<sub>6</sub>H<sub>6</sub>, C<sub>5</sub>NH<sub>5</sub>, and C<sub>4</sub>N<sub>2</sub>H<sub>4</sub> on the Cu(110) Surface. *Phys. Rev. Lett.*, 102:136809, 2009.
- [20] A. Mugarza, R. Robles, C. Krull, R. Korytár, N. Lorente, and P. Gambardella. Electronic and Magnetic Properties of Molecule-Metal Interfaces: Transition-Metal Phthalocyanines Adsorbed on Ag(100). *Phys. Rev. B*, 85:155437, 2012.
- [21] J. Brede, N. Atodiresei, S. Kuck, P. Lazić, V. Caciuc, Y. Morikawa, G. Hoffmann, S. Blügel, and R. Wiesendanger. Spin- and Energy-Dependent Tunneling through a Single Molecule with Intramolecular Spatial Resolution. *Phys. Rev. Lett.*, 105:047204, 2010.
- [22] T. Komeda, H. Isshiki, J. Liu, Y.-F. Zhang, N. Lorente, K. Katoh, B. K. Breedlove, and M. Yamashita. Observation and Electric Current Control of a Local Spin in a Single-Molecule Magnet. *Nature Commun.*, 2:217, 2011.

- 
- [23] A. Lodi Rizzini, C. Krull, T. Balashov, J. J. Kavich, A. Mugarza, P. S. Miedema, P. K. Thakur, V. Sessi, S. Klyatskaya, M. Ruben, S. Stepanow, and P. Gambardella. Coupling Single Molecule Magnets to Ferromagnetic Substrates. *Phys. Rev. Lett.*, 107:177205, 2011.
- [24] S. Sanvito. The Rise of Spinterface Science. *Nature Physics*, 6:562–564, 2010.
- [25] H. Wende, M. Bernien, J. Luo, C. Sorg, N. Ponpandian, J. Kurde, J. Miguel, M. Piantek, X. Xu, Ph. Eckhold, W. Kuch, K. Baberschke, P. M. Panchmatia, B. Sanyal, P. M. Oppeneer, and O. Eriksson. Substrate-Induced Magnetic Ordering and Switching of Iron Porphyrin Molecules. *Nature Materials*, 6:516–520, 2007.
- [26] S. Kuck, G. Hoffmann, M. Bröring, M. Fechtel, M. Funk, and R. Wiesendanger. Naked Iron-5,10,15-triphenylcorrole on Cu(111): Observation of Chirality on a Surface and Manipulation of Multiple Conformational States by STM. *J. Am. Chem. Soc.*, 130:14072–14073, 2008.
- [27] A. Mugarza, C. Krull, R. Robles, S. Stepanow, G. Ceballos, and P. Gambardella. Spin Coupling and Relaxation inside Molecule-Metal Contacts. *Nature Commun.*, 2:490, 2011.
- [28] N. Ishikawa, M. Sugita, T. Ishikawa, S. Koshihara, and Y. Kaizu. Lanthanide Double-Decker Complexes Functioning as Magnets at the Single-Molecular Level. *J. Am. Chem. Soc.*, 125:8694–8695, 2003.
- [29] M. L. Rodriguez-Méndez R. Rousseau, R. Aroca. Extended Hückel Molecular Orbital Model for Lanthanide Bisphthalocyanine Complexes. *Journal of Molecular Structure*, 356:49–62, 1995.
- [30] C. Clarisse and M. T. Riou. Synthesis and Characterization of some Lanthanide Phthalocyanines. *Inorganica Chimica Acta*, 130:139–144, 1987.
- [31] F. Branzoli, P. Carretta, M. Filibian, G. Zoppellaro, M. J. Graf, J. R. Galan-Mascaros, O. Fuhr, S. Brink, and M. Ruben. Spin Dynamics in the Negatively Charged Terbium (III) Bis-phthalocyaninato Complex. *J. Am. Chem. Soc.*, 131:4387–4396, 2009.
- [32] L. Vitali, S. Fabris, A. Mosca Conte, S. Brink, M. Ruben, S. Baroni, and K. Kern. Electronic Structure of Surface-supported Bis(phthalocyaninato) Terbium(III) Single Molecular Magnets. *Nano Lett.*, 8:3364–3368, 2008.
- [33] S. Stepanow, J. Honolka, P. Gambardella, L. Vitali, N. Abdurakhmanova, T.-C. Tseng, S. Rauschenbach, S. L. Tait, V. Sessi, S. Klyatskaya, M. Ruben, and K. Kern. Spin and Orbital Magnetic Moment Anisotropies of Monodispersed Bis(Phthalocyaninato)Terbium on a Copper Surface. *J. Am. Chem. Soc.*, 132:11900–11901, 2010.

- [34] K. Katoh, Y. Yoshida, M. Yamashita, H. Miyasaka, B. K. Breedlove, T. Kajiwara, S. Takaishi, N. Ishikawa, H. Isshiki, Y. F. Zhang, T. Komeda, M. Yamagishi, and J. Takeya. Direct Observation of Lanthanide(III)-Phthalocyanine Molecules on Au(111) by Using Scanning Tunneling Microscopy and Scanning Tunneling Spectroscopy and Thin-Film Field-Effect Transistor Properties of Tb(III)- and Dy(III)-Phthalocyanine Molecules. *J. Am. Chem. Soc.*, 131:9967–9976, 2009.
- [35] K. Katoh, T. Komeda, and M. Yamashita. Surface Morphologies, Electronic Structures, and Kondo Effect of Lanthanide(III)-Phthalocyanine Molecules on Au(111) by Using STM, STS and FET Properties for Next Generation Devices. *Dalton Trans.*, 39:4708–4723, 2010.
- [36] J. Schwöbel, Y. Fu, J. Brede, A. Dilullo, G. Hoffmann, S. Klyatskaya, M. Ruben, and R. Wiesendanger. Real-Space Observation of Spin-Split Molecular Orbitals of Adsorbed Single-Molecule Magnets. *Nature Commun.*, 3:953, 2012.
- [37] J. Bardeen. Tunnelling from a Many-Particle Point of View. *Phys. Rev. Lett.*, 6:57–59, 1961.
- [38] J. Tersoff and D. R. Hamann. Theory and Application for the Scanning Tunneling Microscope. *Phys. Rev. Lett.*, 50:1998–2001, 1983.
- [39] J. Tersoff and D. R. Hamann. Theory of the Scanning Tunneling Microscope. *Phys. Rev. B*, 31:805–813, 1985.
- [40] C. J. Chen. Tunneling Matrix Elements in Three-Dimensional Space: The Derivative Rule and The Sum Rule. *Phys. Rev. B*, 42:8841–8857, 1990.
- [41] R. J. Hamers. Atomic-Resolution Surface Spectroscopy with The Scanning Tunneling Microscope. *Annu. Rev. Phys. Chem.*, 40:531–559, 1989.
- [42] V. A. Ukraintsev. Data Evaluation Technique for Electron-Tunneling Spectroscopy. *Phys. Rev. B*, 53:11176, 1996.
- [43] R. M. Feenstra, J. A. Stroscio, and A. P. Fein. Tunneling Spectroscopy of the Si(111)2x1 Surface. *Surface Science*, 181:295–306, 1987.
- [44] J. C. Slonczewski. Conductance and Exchange Coupling of two Ferromagnets Separated by a Tunneling Barrier. *Phys. Rev. B*, 39:6995–7002, 1989.
- [45] T. Miyazaki and N. Tezuka. Giant Magnetic Tunneling Effect in Fe/Al<sub>2</sub>O<sub>3</sub>/Fe Junction. *J. Magn. Magn. Mater.*, 139:L231–L234, 1995.
- [46] M. Julliere. Tunneling Between Ferromagnetic Films. *Phys. Lett. A*, 54:225–226, 1975.
- [47] D. Wortmann, S. Heinze, Ph. Kurz, G. Bihlmayer, and S. Blügel. Resolving Complex Atomic-Scale Spin Structures by Spin-Polarized Scanning Tunneling Microscopy. *Phys. Rev. Lett.*, 86:4132–4135, 2001.



- 
- [48] M. Cavallini and F. Biscarini. Electrochemically Etched Nickel Tips for Spin Polarized Scanning Tunneling Microscopy. *Rev. Sci. Instrum.*, 71:4457–4460, 2000.
- [49] R. Koltun, M. Herrmann, G. Güntherodt, and V. A. M. Brabers. Enhanced Atomic-Scale Contrast on  $\text{Fe}_3\text{O}_4(100)$  Observed with an Fe STM Tip. *Appl. Phys. A*, 73:49–53, 2001.
- [50] C. Albonetti, I. Bergeneti, M. Cavallini, V. Dediu, M. Massi, J.-F. Moulin, and F. Biscarini. Electrochemical Preparation of Cobalt Tips for Scanning Tunneling Microscopy. *Rev. Sci. Instrum.*, 73:4254–4256, 2002.
- [51] M. Bode, M. Getzlaff, and R. Wiesendanger. Spin-Polarized Vacuum Tunneling into the Exchange-Split Surface State of  $\text{Gd}(0001)$ . *Phys. Rev. Lett.*, 81:4256–4259, 1998.
- [52] A. Kubetzka, M. Bode, O. Pietzsch, and R. Wiesendanger. Spin-Polarized Scanning Tunneling Microscopy with Antiferromagnetic Probe Tips. *Phys. Rev. Lett.*, 88:057201, 2002.
- [53] A. A. Minakov and I. V. Shvets. On the Possibility of Resolving Quantization Axes of Surface Spins by Means of a Scanning Tunneling Microscope with a Magnetic Tip. *Surface Science Letters*, 236:L377–L381, 1990.
- [54] André Kubetzka. *Spinpolarisierte Rastertunnelmikroskopie an magnetischen Nanostrukturen: Fe/W(110)*. PhD thesis, University of Hamburg, 2002.
- [55] A. Li Bassi, C. S. Casari, D. Cattaneo, F. Donati, S. Foglio, M. Passoni, C. E. Bottani, P. Biagoni, A. Brambilla, M. Finazzi, F. Ciccacci, and L. Duò. Bulk Cr Tips for Scanning Tunneling Microscopy and Spin-Polarized Scanning Tunneling Microscopy. *Appl. Phys. Lett.*, 91:173120, 2007.
- [56] A. Schlenhoff, S. Krause, G. Herzog, and R. Wiesendanger. Bulk Cr Tips with Full Spatial Magnetic Sensitivity for Spin-Polarized Scanning Tunneling Microscopy. *Appl. Phys. Lett.*, 97:083104, 2010.
- [57] J. E. McKendry, C. S. Allen, K. Critchley, M. Ł. Górzny, A. S. Walton, and S. D. Evans. Magnetic Field enhanced Nano-Tip Fabrication for Four-Probe STM Studies. *Nanotechnology*, 19:085201, 2008.
- [58] M. Bode, S. Krause, L. Berbil-Bautista, S. Heinze, and R. Wiesendanger. On the Preparation and Electronic Properties of Clean  $\text{W}(110)$  Surfaces. *Surface Science*, 601:3308–3314, 2007.
- [59] A. de Cian, M. Moussavi, R. Weiss, and J. Fischer. Synthesis, Structure, and Spectroscopic and Magnetic Properties of Lutetium(III) Phthalocyanine Derivatives:  $\text{LuPc}_2\cdot\text{CH}_2\text{Cl}_2$  and  $[\text{LuPc}(\text{OAc})(\text{H}_2\text{O})_2]\cdot\text{H}_2\text{O}\cdot 2\text{CH}_3\text{OH}$ . *Inorg. Chem.*, 24:3162–3167, 1985.

## Bibliography

---

- [60] J.-P. Bucher, L. Santesson, and K. Kern. Thermal Healing of Self-Assembled Organic Monolayers: Hexane- and Octadecanethiol on Au(111) and Ag(111). *Langmuir*, 10:979–983, 1994.
- [61] H. Tanaka, T. Ikeda, K. Yamashita, M. Takeuchi, S. Shinkai, and T. Kawai. Network of Tris(porphyrinato)cerium(III) Arranged on the Herringbone Structure of an Au(111) Surface. *Langmuir*, 26:210–214, 2010.
- [62] C. Pérez León, C. Sürgers, M. Mayor, M. Marz, R. Hoffmann, and H. von Löhneseisen. STM Investigation of Large  $\pi$ -Conjugated Oligomers and Tetrahydrofuran Codeposited on Cu(111) by Pulse Injection. *J. Phys. Chem. C*, 113:14335–14340, 2009.
- [63] S. Rauschenbach, F. L. Stadler, E. Lunedei, N. Malinowski, S. Koltsov, G. Costantini, and K. Kern. Electro spray Ion Beam Deposition of Clusters and Biomolecules. *small*, 2:540–547, 2006.
- [64] M. Toader, M. Knupfer, D. R. T. Zahn, and M. Hietschold. Initial Growth of Lutetium(III) Bis-phthalocyanine on Ag(111) Surface. *J. Am. Chem. Soc.*, 133:5538–5544, 2011.
- [65] Y. Zhang, P. Guan, H. Isshiki, M. Chen, M. Yamashita, and T. Komeda. Bis(phthalocyaninato)yttrium Grown on Au(111): Electronic Structure of a Single Molecule and the Stability of Two-Dimensional Films Investigated by Scanning Tunneling Microscopy/Spectroscopy at 4.8 K. *Nano Res*, 3:604–611, 2010.
- [66] P. H. Lippel, R. J. Wilson, M. D. Miller, Ch. Wöll, and S. Chiang. High-Resolution Imaging of Copper-Phthalocyanine by Scanning-Tunneling Microscopy. *Phys. Rev. Lett.*, 62:171–174, 1989.
- [67] M. MŠadak, J. Roncali, and F. Garnier. Lanthanide-Phthalocyanine Complexes: From a Diphtalocyanine  $Pc_2Ln$  to a Super Complex  $Pc_3Ln_2$ . *J. Chim. Physicochim. Biol.*, 83, 1986.
- [68] Y. Wang, J. Kröger, R. Berndt, and W. Hofer. Structural and Electronic Properties of Ultrathin Tin-Phthalocyanine Films on Ag(111) at the Single-Molecule Level. *Angewandte Chemie*, 121:1287–1291, 2009.
- [69] D. G. Fedak and N. A. Gjostein. Structure and Stability of the (100) Surface of Gold. *Phys. Rev. Lett.*, 16:171–172, 1966.
- [70] K. Toyoda, Y. Nakano, I. Hamada, K. Lee, S. Yanagisawa, and Y. Morikawa. First-Principles Study of Benzene on Noble Metal Surfaces: Adsorption States and Vacuum Level Shifts. *Surface Science*, 603:2912 – 2922, 2009.
- [71] N. Lorente, M. F. G. Hedouin, R. E. Palmer, and M. Persson. Chemisorption of Benzene and STM Dehydrogenation Products on Cu(100). *Phys. Rev. B*, 68:155401, 2003.

- 
- [72] N. Atodiresei, V. Caciuc, P. Lazić, and S. Blügel. Engineering the Magnetic Properties of Hybrid Organic-Ferromagnetic Interfaces by Molecular Chemical Functionalization. *Phys. Rev. B*, 84:172402, 2011.
- [73] H. B. Michaelson. The Work Function of the Elements and its Periodicity. *J. Appl. Phys.*, 48:4729, 1977.
- [74] K. Walzer and M. Hietschold. STM and STS Investigation of Ultrathin Tin Phthalocyanine Layers Adsorbed on HOPG(0001) and Au(111). *Surface Science*, 471:1–10, 2001.
- [75] A. F. Takács, F. Witt, S. Schmaus, T. Balashov, M. Bowen, E. Beaupaire, and W. Wulfhchel. Electron Transport Through Single Phthalocyanine Molecules Studied using Scanning Tunneling Microscopy. *Phys. Rev. B*, 78:233404, 2008.
- [76] S.-H. Chang, S. Kuck, J. Brede, L. Lichtenstein, G. Hoffmann, and R. Wiesendanger. Symmetry Reduction of Metal Phthalocyanines on Metals. *Phys. Rev. B*, 78:233409, 2008.
- [77] X. W. Tu, G. Mikaelian, and W. Ho. Controlling Single-Molecule Negative Differential Resistance in a Double-Barrier Tunnel Junction. *Phys. Rev. Lett.*, 100:126807, 2008.
- [78] P. Hohenberg and W. Kohn. Inhomogeneous Electron Gas. *Phys. Rev.*, 136:B864–B870, 1964.
- [79] V. I. Anisimov, F. Aryasetiawan, and A. I. Lichtenstein. First-Principles Calculations of the Electronic Structure and Spectra of Strongly Correlated Systems: The LDA+U Method. *J. Phys.: Condens. Matter*, 9:767–808, 1997.
- [80] A. Mugarza, N. Lorente, P. Ordejón, C. Krull, S. Stepanow, M.-L. Bocquet, J. Fraxedas, G. Ceballos, and P. Gambardella. Orbital Specific Chirality and Homochiral Self-Assembly of Achiral Molecules Induced by Charge Transfer and Spontaneous Symmetry Breaking. *Phys. Rev. Lett.*, 105:115702, 2010.
- [81] N. Atodiresei. "private communication", 2012.
- [82] M. Bode, A. Kubetzka, O. Pietzsch, and R. Wiesendanger. Spin-Polarized Scanning Tunneling Spectroscopy on Fe Nanowires. *Appl. Phys. A*, 72:S149–S153, 2001.
- [83] O. Pietzsch, A. Kubetzka, M. Bode, and R. Wiesendanger. Real-Space Observation of Dipolar Antiferromagnetism in Magnetic Nanowires by Spin-Polarized Scanning Tunneling Spectroscopy. *Phys. Rev. Lett.*, 84:5212–5215, 2000.
- [84] J.D.H Donnay and H.M. Ondik, editors. *Crystal Data*. Gaithersburg, MD, 1973.
- [85] U. Gradmann and G. Waller. Periodic Lattice Distortions in Epitaxial Films of Fe(110) on W(110). *Surface Science*, 116:539–548, 1982.

## Bibliography

---

- [86] P. J. Berlowitz, J.-W. He, and D. W. Goodman. Overlayer Growth and Chemisorptive Properties of Ultra-Thin Fe Films on W(110) and W(100). *Surface Science*, 231:315–324, 1990.
- [87] J. Kołaczkiwicz and E. Bauer. V and Fe on the W(110) Face. *Surface Science*, 450:106–116, 2000.
- [88] H. J. Elmers, J. Hauschild, H. Höche, U. Gradmann, H. Bethge, D. Heuer, and U. Köhler. Submonolayer Magnetism of Fe(110) on W(110): Finite Width Scaling of Stripes and Percolation between Islands. *Phys. Rev. Lett.*, 73:898–901, 1994.
- [89] H. Bethge, D. Heuer, Ch. Jensen, K. Reshöft, and U. Köhler. Misfit-Related Effects in the Epitaxial Growth of Iron on W(110). *Surface Science*, 331–333:878–884, 1995.
- [90] Matthias Bode. *Strukturelle und Lokale Elektronische Eigenschaften Ultradünner Eisenfilme auf W(110)*. PhD thesis, University of Hamburg, 1996.
- [91] M. Przybylski and U. Gradmann. Ferromagnetic Order in a Fe(110) Monolayer on W(110) by Mössbauer Spectroscopy. *Phys. Rev. Lett.*, 59:1152–1155, 1987.
- [92] J. Hauschild, H. J. Elmers, and U. Gradmann. Dipolar Superferromagnetism in Monolayer Nanostripes of Fe(110) on Vicinal W(110) Surfaces. *Phys. Rev. B*, 57:R677–R680, 1998.
- [93] J. Hauschild, U. Gradmann, and H. J. Elmers. Perpendicular Magnetization and Dipolar Antiferromagnetism in Double Layer Nanostripe Arrays of Fe(110) on W(110). *Appl. Phys. Lett.*, 72:3211–3213, 1998.
- [94] H. J. Elmers, J. Hauschild, and U. Gradmann. Onset of Perpendicular Magnetization in Nanostripe Arrays of Fe on Stepped W(110) Surfaces. *Phys. Rev. B*, 59:3688–3695, Feb 1999.
- [95] L. Z. Mezey and J. Giber. The Surface Free Energies of Solid Chemical Elements: Calculation from Internal Free Enthalpies of Atomization. *Jpn. J. Appl. Phys.*, 21:1569–1571, 1982.
- [96] H. J. Elmers, J. Hauschild, and U. Gradmann. Reorientation of Magnetization States in Fe-Nanostripe Arrays on Stepped W(110) Caused by Adsorption of Co, H<sub>2</sub> and O<sub>2</sub>. *J. Magn. Magn. Mat.*, 198:222–224, 1999.
- [97] H. J. Elmers, J. Hauschild, and U. Gradmann. Morphology and Magnetism of Fe on Vicinal W(1 1 0) Surfaces with Different Step Orientation. *J. Magn. Magn. Mat.*, 221:219–223, 2000.
- [98] R. Kurzawa, K.-P. Kämper, W. Schmitt, and G. Güntherodt. Spin-Resolved Photoemission Study of in situ Grown Epitaxial Fe Layers on W(110). *Sol. State. Commun.*, 60:777–780, 1986.

- 
- [99] A. Kubetzka, O. Pietzsch, M. Bode, and R. Wiesendanger. Spin-Polarized Scanning Tunneling Microscopy Study of  $360^\circ$  Walls in an External Magnetic Field. *Phys. Rev. B*, 67:020401, 2003.
- [100] Stefan Meckler. *Non-Collinear Magnetism in Fe on W(110)*. PhD thesis, University of Hamburg, 2010.
- [101] A. Hubert and R Schäfer. *Magnetic Domains*. Springer-Verlag Berlin Heidelberg, 2000.
- [102] E. Y. Vedmedenko, A. Kubetzka, K. von Bergmann, O. Pietzsch, M. Bode, J. Kirschner, H. P. Oepen, and R. Wiesendanger. Domain Wall Orientation in Magnetic Nanowires. *Phys. Rev. Lett.*, 92:077207, 2004.
- [103] P. Ferriani, K. von Bergmann, E. Y. Vedmedenko, S. Heinze, M. Bode, M. Heide, G. Bihlmayer, S. Blügel, and R. Wiesendanger. Atomic-Scale Spin Spiral with a Unique Rotational Sense: Mn Monolayer on W(001). *Phys. Rev. Lett.*, 101:027201, 2008.
- [104] S. Heinze, K. von Bergmann, M. Menzel, J. Brede, A. Kubetzka, R. Wiesendanger, G. Bihlmayer, and S. Blügel. Spontaneous Atomic-Scale Magnetic Skyrmion Lattice in Two Dimensions. *Nature Physics*, 2045, 2011.
- [105] M. Heide, G. Bihlmayer, and S. Blügel. Dzyaloshinskii-Moriya Interaction Accounting for the Orientation of Magnetic Domains in Ultrathin Films: Fe/W(110). *Phys. Rev. B*, 78:140403, 2008.
- [106] S. Meckler, N. Mikuszeit, A. Preßler, E. Y. Vedmedenko, O. Pietzsch, and R. Wiesendanger. Real-Space Observation of a Right-Rotating Inhomogeneous Cycloidal Spin Spiral by Spin-Polarized Scanning Tunneling Microscopy in a Triple Axes Vector Magnet. *Phys. Rev. Lett.*, 103:157201, 2009.
- [107] M. Bode, S. Heinze, A. Kubetzka, O. Pietzsch, X. Nie, G. Bihlmayer, S. Blügel, and R. Wiesendanger. Magnetization-Direction-Dependent Local Electronic Structure Probed by Scanning Tunneling Spectroscopy. *Phys. Rev. Lett.*, 89:237205, 2002.
- [108] M. Bode, A. Kubetzka, S. Heinze, O. Pietzsch, R. Wiesendanger, M. Heide, X. Nie, G. Bihlmayer, and S. Blügel. Spin-Orbit Induced Local Band Structure Variations Revealed by Scanning Tunneling Spectroscopy. *Journal of Physics: Condensed Matter*, 15:S679–S692, 2003.
- [109] J. A. Stroscio, D. T. Pierce, A. Davies, R. J. Celotta, and M. Weinert. Tunneling Spectroscopy of bcc (001) Surface States. *Phys. Rev. Lett.*, 75:2960–2963, 1995.
- [110] P. Ferriani, C. Lazo, and S. Heinze. Origin of the Spin Polarization of Magnetic Scanning Tunneling Microscopy Tips. *Phys. Rev. B*, 82:054411, 2010.

## Bibliography

---

- [111] A. Wachowiak, J. Wiebe, M. Bode, O. Pietzsch, M. Morgenstern, and R. Wiesendanger. Direct Observation of Internal Spin Structure of Magnetic Vortex Cores. *Science*, 298:577–580, 2002.
- [112] C. Iacovita, M. V. Rastei, B. W. Heinrich, T. Brumme, J. Kortus, L. Limot, and J. P. Bucher. Visualizing the Spin of Individual Cobalt-Phthalocyanine Molecules. *Phys. Rev. Lett.*, 101:116602, 2008.
- [113] M. Bernien, J. Miguel, C. Weis, M. E. Ali, J. Kurde, B. Krumme, P. M. Panchmatia, B. Sanyal, M. Piantek, P. Srivastava, K. Baberschke, P. M. Oppeneer, O. Eriksson, W. Kuch, and H. Wende. Tailoring the Nature of Magnetic Coupling of Fe-Porphyrin Molecules to Ferromagnetic Substrates. *Phys. Rev. Lett.*, 102:047202, 2009.
- [114] R. Biagi, J. Fernandez-Rodriguez, M. Gonidec, A. Mirone, V. Corradini, F. Moro, V. De Renzi, U. del Pennino, J. C. Cezar, D. B. Amabilino, and J. Veciana. X-Ray Absorption and Magnetic Circular Dichroism Investigation of Bis(phthalocyaninato)Terbium Single-Molecule Magnets Deposited on Graphite. *Phys. Rev. B*, 82:224406, 2010.
- [115] B. T. Li, W. Hu, and D. Zhu. Nanogap Electrodes. *Advanced Materials*, 22:286–300, 2010.
- [116] F. O. Hadeed and C. Durkan. Controlled Fabrication of 1–2nm Nanogaps by Electromigration in Gold and Gold-Palladium Nanowires. *Appl. Phys. Lett.*, 91:123120, 2007.
- [117] M. C. Tringides, M. Jałochowski, and E. Bauer. Quantum Size Effects in Metallic Nanostructures. *Physics Today*, 60:50–54, 2007.
- [118] C. Besson. "private communication", 2012.

---

## Acknowledgement

---

Diese Doktorarbeit ist im Rahmen meiner dreijährigen Tätigkeit am Peter Grünberg Institut (PGI-6) des Forschungszentrums Jülich entstanden. Natürlich können die physikalischen Experimente und die anschließende Auswertung nur in enger Zusammenarbeit mit den vielen anderen Mitarbeitern des Instituts zu einem gelungenem Gesamtergebnis führen. Ich möchte mich deshalb hier noch einmal bei allen, die mich in den vergangenen Jahren begleitet haben, bedanken.

Zuallererst bedanke ich mich bei meinem Doktorvater **PD Dr. Daniel E. Bürgler** für die vorzügliche Betreuung. Daniel, die vergangenen drei Jahre waren durch eine Flut an neuen Aufgaben und Herausforderungen gekennzeichnet, bei denen du mir jederzeit unterstützend zur Seite gestanden hast. Danke dafür!

**Prof. Dr. Thomas Michely** danke ich für die Übernahme der Zweitkorrektur meiner Arbeit.

Bei unserem Institutsdirektor **Prof. Dr. Claus M. Schneider** bedanke ich mich dafür, dass er mir die Möglichkeit gegeben hat, auf diversen Konferenzen meine Ergebnisse zu präsentieren, für die fantastische Ausstattung unseres Labors und lehrreiche Erkenntnisse im Seminarraum.

**Prof. Dr. Paul Kögerler** danke ich für die Unterstützung seitens der Molekül-Bereitstellung.

Mein Laboralltag wurde über die drei Jahre hinweg von vielen Kollegen begleitet, denen ich im Folgenden danken möchte.

**Dr. Frank Matthes** hat mich in die mysteriöse Welt des Ultrahochvakuums eingeführt. Ich danke dir, Frank, für die vielen Stunden des Erklärens und Unterstützens! **Dr. Julius Mennig** und **Christian Hahn** bin ich dankbar für die gemeinsame Zeit des Präparierens, Messens, Schraubens und (manchmal) Reparierens. Bei den letzten beiden Tätigkeiten sind wir häufig auf das technische Personal unseres Instituts angewiesen gewesen, das zum Glück jederzeit zur tatkräftigen Unterstützung herbeieilte. **Franz-Josef Köhne** und **Thomas Jansen** möchte ich hier ganz besonders erwähnen, aber auch an **Bernd Küpper**,

**Norbert Schnitzler** und **Konrad Bickmann** sowie die Herren aus der E-Werkstatt, **Heinz Pfeifer** und **Jürgen Lauer**, geht mein Dank.

**Dr. Claire Besson** hat es geschafft, mich in die Geheimnisse der Chemie einzuweihen und ganz nebenbei jederzeit neue Moleküle geliefert; meist zu Ungunsten ihres weißen Kittels. Danke für deine Unterstützung, Claire!

**Dr. Nicolae Atodiresei** und **Dr. Vasile Caciuc** danke ich für den enormen Anteil, den sie durch ihre Arbeit zum Verständnis meiner experimentellen Ergebnisse beigetragen haben. Sie haben sich in vielen Diskussionen immer die Zeit genommen, meine großen und kleinen Fragen verständlich und detailliert zu beantworten.

Die vielen übrigen **Mitarbeiter des PGI-6**, die ich hier nicht namentlich aufführen kann, sind in jedem Fall ausschlaggebend dafür gewesen, dass ich in den vergangenen drei Jahren eine sehr angenehme und lehrreiche Zeit am Forschungszentrum in Jülich erleben durfte. Ich bedanke mich bei euch für Kaffee- und Mittagspausen, Institutsausflüge, Probevorträge, Erklärungen und Hilfestellungen aller Art, sei es ein zu schweres Vakuumteil, ein zu kleines Fahrrad, Flugangst oder ein liegengebliebenes Auto.

Zu guter Letzt bedanke ich mich bei **meinen Eltern und meiner Familie** für den fortwährenden Rückhalt und die Ermunterung zu lernen und zu entdecken. Und bei meinem Freund **Lukas**, der immer für mich da ist.



---

## Erklärung

---

Ich versichere, dass ich die von mir vorgelegte Dissertation selbständig angefertigt, die benutzten Quellen und Hilfsmittel vollständig angegeben und die Stellen der Arbeit – einschließlich Tabellen, Karten und Abbildungen –, die anderen Werken im Wortlaut oder dem Sinn nach entnommen sind, in jedem Einzelfall als Entlehnung kenntlich gemacht habe; dass diese Dissertation noch keiner anderen Fakultät oder Universität zur Prüfung vorgelegen hat; dass sie – abgesehen von unten angegebenen Teilpublikationen – noch nicht veröffentlicht worden ist sowie, dass ich eine solche Veröffentlichung vor Abschluss des Promotionsverfahrens nicht vornehmen werde. Die Bestimmungen der Promotionsordnung sind mir bekannt. Die von mir vorgelegte Dissertation ist von PD Dr. Daniel E. Bürgler betreut worden.

Jülich, den 28. 11. 2012

Sarah Fahrendorf



---

## Curriculum Vitae

---

### Personal Data

Sarah Fahrendorf  
born 06.07.1984 in Marl  
german

### Education

- since 01/2010      PETER GRÜNBERG INSTITUT, FORSCHUNGSZENTRUM JÜLICH  
Ph.D. in physics  
Supervisor: PD Dr. D. E. Bürgler
- 10/2004 – 10/2009      RHEINISCH-WESTFÄLISCHE TECHNISCHE HOCHSCHULE ZU AACHEN  
10/2009      Diploma in physics  
Diploma thesis:  
Topic: *Spin-Transfer-induzierte Spinnwellenanregung in nano-  
strukturierten ferromagnetischen Einzelschichten*  
Supervisor: Prof. Dr. G. Güntherodt, Physikalisches Institut 2a
- 09/1995 – 06/2004      GYMNASIUM IM LOEKAMP, MARL  
06/2004      Abitur

### Jobs

- 10/2006 – 08/2009      PHYSIKALISCHES INSTITUT 1A, RWTH AACHEN  
Tutor for physics lab courses
- 01/2009 – 06/2009      PHYSIKALISCHES INSTITUT 2A, RWTH AACHEN  
Tutor for physics lab courses

Jülich, November 28th 2012